

Search for Higgs boson pair
production in the $HH \rightarrow bb\tau\tau$
channel in p-p collisions using
CMS data at $\sqrt{s} = 13 \text{ TeV}$ at the
LHC

By

RAJARSHI BHATTACHARYA

PHYS05201304017

Saha Institute of Nuclear Physics, Kolkata

A thesis submitted to

The Board of Studies in Physical Sciences

In partial fulfilment of requirements

For the Degree of

DOCTOR OF PHILOSOPHY

of

HOMI BHABHA NATIONAL INSTITUTE



June, 2020

Homi Bhabha National Institute¹

Recommendations of the Viva Voce Committee

As members of the Viva Voce Committee, we certify that we have read the dissertation prepared by Rajarshi Bhattacharya entitled “Search for Higgs boson pair production in the $HH \rightarrow bb\tau\tau$ channel in p-p collisions using CMS data at $\sqrt{s} = 13 \text{ TeV}$ at the LHC” and recommend that it may be accepted as fulfilling the thesis requirement for the award of Degree of Doctor of Philosophy.

Chairman	Prof. Sukalyan Chattopadhyay		Date:
Guide/Convener	Prof. Subir Sarkar		Date:
Co-Guide	Prof. Suchandra Dutta		Date:
Examiner	Prof. Sreerup Raychaudhuri		Date:
Member 1	Prof. Pratik Majumdar		Date:
Member 2	Prof. Tapan Kumar Nayak		Date:

Final approval and acceptance of this thesis is contingent upon the candidate's submission of the final copies of the thesis to HBNI.

I hereby certify that I/we have read this thesis prepared under my direction and recommend that it may be accepted as fulfilling the thesis requirement.

Date: 29/01/2021

Suchandra Dutta
Co-guide

Subir Sarkar
Guide

Place: KOLKATA

¹This page is to be included only for final submission after successful completion of viva voce.

STATEMENT BY AUTHOR

This dissertation has been submitted in partial fulfilment of requirements for an advanced degree at Homi Bhabha National Institute (HBNI) and is deposited in the Library to be made available to borrowers under rules of the HBNI.

Brief quotations from this dissertation are allowable without special permission, provided that accurate acknowledgement of source is made. Requests for permission for extended quotation from or reproduction of this manuscript in whole or in part may be granted by the Competent Authority of HBNI when in his or her judgment the proposed use of the material is in the interests of scholarship. In all other instances, however, permission must be obtained from the author.

Rajarshi Bhattacharya

Rajarshi Bhattacharya

DECLARATION

I, hereby declare that the investigation presented in the thesis has been carried out by me. The work is original and has not been submitted earlier as a whole or in part for a degree / diploma at this or any other Institution / University.

Rajarshi Bhattacharya

Rajarshi Bhattacharya

List of Publications arising from the thesis

Journal

1. The CMS Collaboration, “Search for Higgs boson pair production in events with two bottom quarks and two tau leptons in proton-proton collisions at $\sqrt{s} = 13 \text{ TeV}$ ”, *Phys. Lett. B* **778** (2018) 101-127, [doi:10.1016/j.physletb.2018.01.001](https://doi.org/10.1016/j.physletb.2018.01.001), [arXiv:1707.02909](https://arxiv.org/abs/1707.02909)
2. The CMS Tracker Group, “Beam test performance of prototype silicon detectors for the Outer Tracker for the Phase-2 Upgrade of CMS”, *JINST* **15** (2020) 03, P03014, [doi:10.1088/1748-0221/15/03/P03014](https://doi.org/10.1088/1748-0221/15/03/P03014)

Conferences

1. Rajarshi Bhattacharya, Suchandra Dutta and Subir Sarkar, “Study of $B_s^0 \rightarrow \phi\phi \rightarrow KKKK$ with the CMS Phase II Detector”, XXII DAE-BRNS High Energy Physics Symposium, 12-16 Dec 2016, University of Delhi, Delhi (India), *Springer Proc. Phys.* **203** (2018) 317-320 [doi:10.1007/978-3-319-73171-1_72](https://doi.org/10.1007/978-3-319-73171-1_72)
2. Rajarshi Bhattacharya, “Prospects of CMS in B physics in Phase-2”, 16th Conference on Flavour Physics and CP Violation (FPCP 2018), Hyderabad, India, 14-18 July, 2018

Others

1. The CMS Collaboration, “The Phase-2 Upgrade of the CMS tracker”, CERN-LHCC-2017-009, CMS-TDR-014
2. Report from Working Group 4: “Opportunities in Flavour Physics at the HL-LHC and HE-LHC”, *CERN Yellow Rep. Monogr.* **7** (2019) 867-1158, HL/HE-LHC Workshop, CERN-LPCC-2018-06 [doi:10.23731/CYRM-2019-007.867](https://doi.org/10.23731/CYRM-2019-007.867), [arXiv:1812.07638](https://arxiv.org/abs/1812.07638)

3. The CMS Collaboration, “Search for pair production of Higgs bosons in the two tau leptons and two bottom quarks final state using proton-proton collisions at $\sqrt{s} = 13 \text{ TeV}$ ”, CMS-PAS-HIG-17-002
4. Chiara Amendola, Konstantin Androsov, Giuseppe Bagliesi, Rajarshi Bhattacharya, Florian Beaudette, Francesco Brivio, Luca Cadamuro, Claudio Caputo, Maria Agnese Ciocci, Pietro Govoni, Maria Teresa Grippo, Ricardo Manzoni, Giacomo Ortona, Roberto Salerno, and Yves Sirois, “Search for Higgs boson pair production in the $bb\tau\tau$ final state with the CMS detector at the LHC, CMS Analysis Note: AN-17-007
5. Jeremy Andrea, Panagiotis Assiouras, Georg Auzinger, Rajarshi Bhattacharya, Anadi Canepa, Nicolas Pierre Chanon, Vladimir Cherepanov, Nikkie Deelen, Martin Delcourt, Alexander Dierlamm, Suchandra Dutta, Thomas Eichhorn, Tomasz Gadek, Yuri Gershtein, Geoffrey Hall, Mykyta Haranko, Robert Harr, Siew Yan Hoh, Alan Honma, Tom James, Mark Kovacs, Aristoteles Kyriakis, Dimitrios Loukas, Jelena Luetic, Stefano Mersi, Mark Pesaresi, Nabin Poudyal, Alan Prosser, Ryan Rivera, Alessandro Rossi, Suvankar Roy Chowdhury, Subir Sarkar, Basil Schneider, Sarah Seif El Nasr, Jarne Theo De Clercq, Kirika Uchida, Lorenzo Uplegger, and Giovanni Zevi Della Porta, “Beam Test Performance of Prototype Silicon Detectors for the Outer Tracker for the Phase-2 Upgrade of CMS”, CMS Detector Note: CMS-DN-17-032
6. The CMS Collaboration, “ECFA 2016: Prospects for selected standard model measurements with the CMS experiment at the High-Luminosity LHC”, CMS-PAS-FTR-16-006
7. Rajarshi Bhattacharya, Suchandra Dutta, Subir Sarkar, “Study of $B_s \rightarrow \phi\phi \rightarrow 4K$ with the CMS Phase II Detector”, CMS Analysis Note: AN-16-322
8. Rajarshi Bhattacharya, Suchandra Dutta, Subir Sarkar, “Prospects on $B_s \rightarrow \phi\phi \rightarrow 4K$ with the CMS Detector at the LHC Phase II”, CMS Analysis Note: AN-17-124

Rajarshi Bhattacharya
Rajarshi Bhattacharya

DEDICATION

Dedicated to my beloved family

ACKNOWLEDGEMENTS

I would like to start by expressing my heartfelt gratitude to my supervisors Prof. Subir Sarkar and Prof. Suchandra Dutta for their constant support throughout my Ph.D. tenure. They have consistently helped me by providing the physics and technical knowledge required for the research work. They have also helped me tremendously in my thesis writing.

I would also like to thank Prof. Satyaki Bhattacharya for the many discussions we had and Prof. Sunanda Banerjee for motivating me throughout the Ph.D. tenure.

I would also like to thank the CMS group of the INFN Pisa for hosting me many times. A special mention for Konstantin Androsov from INFN Pisa has to be there and any words describing Konstantin's help in my research work would be less. He was constantly involved in my research work related to $HH \rightarrow b\bar{b}\tau\tau$ analysis and helped me to learn the analysis techniques in the CMS. I would also like to express my sincere gratitude to Prof. Giuseppe Bagliesi, Prof. Agnese Ciocci, Maria Teresa Grippo, Maria Rosaria Di Domenico and Angela Giraldi, from the INFN Pisa, for their help in the $HH \rightarrow b\bar{b}\tau\tau$ analysis. I would also like to thank Prof. Alberto Messineo, with whom I had opportunity to work during one of my INFN Pisa visits.

I would like to thank the whole $HH \rightarrow b\bar{b}\tau\tau$ analysis group in the CMS and all the people related to the beam test of the Strip-Strip (2S) module for their constant help and support.

I would like to acknowledge Fabrizio Palla, Mario Galanti and Urs Langenegger for providing necessary knowledge for the $B_s^0 \rightarrow \phi\phi \rightarrow 4$ Kaons study.

I would also express my gratitude to the CMS collaboration for letting me work as a part of them. I would also like to thank Saha Institute of Nuclear Physics (SINP)

and Homi Bhabha National Institute (HBNI) for giving me an opportunity to do Ph.D. I would also like to thank Department of Atomic Energy, India for funding me during my Ph.D. tenure.

I would also like to thank my batch-mates of the Post-M.Sc. at SINP, with whom I have grown a fond friendship during the Ph.D. tenure. I would like to thank all my colleagues at the HENPP division; specially Atanuda, Kalyanmoyda, Swagatadi, Debarotidi, Palashda, Biswarupda, Niyajda, Souravda, Mahotsabda, Suvonkarda, Kuntalda, Asimda, Arnab, Biswarup, Shamik, Saswati, Arghya, Debabrata, Prasant, Jhuma, Wadud, Aritra, Gourab and Pritam, for their constant help and support. I have spent most of my Ph.D. time with them and discussions with them helped me to clear many confusions. The casual interactions with them also helped me to keep my work experience stress-free.

Finally, last but not the least, I would like to thank my family: my parents, my wife, my aunt, my brother and my in-laws for keeping their faith and supporting me throughout my Ph.D. tenure.

Rajarshi Bhattacharya

Rajarshi Bhattacharya

Contents

Summary	xxii
List of Figures	xxxviii
List of Tables	xli
1 Introduction	1
2 The Standard Model of Particle Physics	5
2.1 The Standard Model of Particle Physics	5
2.2 The Symmetry group of the Standard Model	8
2.3 Quantum Electrodynamics	9
2.4 Quantum Chromodynamics	11
2.5 Weak interactions and the standard Electroweak theory	12
2.6 Spontaneous Symmetry Breaking and the Brout-Englert-Higgs Mechanism	15
2.7 The Higgs self-interaction	18
2.8 HH production	19
2.9 HH decay	20
2.10 Physics beyond the Standard Model	23
2.11 HH production as a probe for BSM physics	23
2.11.1 Non-resonant HH production	23
2.11.2 Resonant HH production	24
2.12 Decays of B_s^0 meson as a probe for BSM physics	26
2.13 $B_s^0 \rightarrow \phi\phi \rightarrow 4$ Kaons	27
3 The CMS experiment at the LHC	29
3.1 The LHC	29
3.2 The CMS Detector	35

3.2.1	Tracker	38
3.2.2	Electromagnetic Calorimeter	43
3.2.3	Hadron Calorimeter	47
3.2.4	Muon System	50
3.3	The CMS Trigger and DAQ System	52
3.4	CMS Data and Monte Carlo Events	56
3.4.1	CMS data tiers	60
4	Physics Object Reconstruction in CMS	61
4.1	Beam spot reconstruction	61
4.2	Primary vertex reconstruction	62
4.3	Particle Flow algorithm	63
4.4	Electron reconstruction and identification	65
4.5	Photon Reconstruction	67
4.6	Muon reconstruction	68
4.7	Jet Clustering	70
4.7.1	b-Jet	71
4.8	Reconstruction of hadronic τ decays	72
4.8.1	Missing Transverse Momentum	76
5	Search for Higgs boson pair production in the $b\bar{b}\tau\tau$ final state	79
5.0.1	High Level Trigger	81
5.1	Collision datasets	81
5.2	Simulated events	81
5.2.1	Background datasets	82
5.2.2	Signal datasets	83
5.3	Event Selection	85
5.3.1	Muon selection	86
5.3.2	Electron selection	86
5.3.3	τ_h selection	87
5.3.4	Selection of the $H \rightarrow \tau\tau$ candidate	87
5.3.5	Selection of the $H \rightarrow b\bar{b}$ candidate	89
5.3.6	Categorisation of events based on jet configuration	89
5.3.7	HH candidate selection	91
5.3.8	Final discriminating variables	93
5.4	Background estimation	96
5.4.1	QCD multi-jet event	97
5.4.2	Drell-Yan + jets background estimation	100

5.5	Systematic Uncertainties	101
5.6	Results	104
6	CMS Phase-2 Tracker and Level1 Tracking	111
6.1	The CMS Phase-2 Tracker	113
6.2	Concept of p_T discrimination	115
6.3	L1 Tracking	117
7	Test Beam Results for Prototype 2S modules	121
7.1	The CBC2	122
7.2	Prototype 2S Modules	124
7.3	Test beam setup	126
7.4	Reconstruction	129
7.5	Test beam measurements	131
7.6	Results	132
	7.6.1 Performance of mini-modules	132
	7.6.2 Performance of the full-sized module	137
7.7	Conclusions	140
8	Trigger level study of $B_s^0 \rightarrow \phi\phi \rightarrow 4$ Kaons using L1 Tracks for HL-LHC	141
8.1	Dataset	142
8.2	Event Selection	143
	8.2.1 Track Selection	144
	8.2.2 Reconstruction of ϕ candidates	144
	8.2.3 Reconstruction of B_s^0 candidates	145
8.3	Results	148
	8.3.1 Effect of Level-1 tracking p_T threshold on signal efficiency and trigger rate	156
8.4	Summary	157
9	Conclusions	159
10	Appendix	163
10.1	CMS Datasets for 2016	163
10.2	Background Monte-Carlo datasets	165
10.3	Signal Mote-Carlo Datasets	166
	10.3.1 Resonant Datasets	166
	10.3.2 Non-Resonant Datasets	167

List of Figures

2.1	Feynman diagram for interaction between a charged fermion and a photon.	11
2.2	Feynman diagrams for QCD interactions, (a) quark-gluon interaction, (b) gluon trilinear self-interaction and (c) gluon quartic self-interaction.	12
2.3	(a) Higgs to fermions vertex and (b) Higgs to gauge bosons vertex	18
2.4	Higgs self-interaction (a) trilinear, and (b) quartic.	19
2.5	Feynman diagrams for HH production at the LHC through the ggF process. (a) HH produced solely via the Higgs-to-top coupling (y_t), and (b) HH produced by both the Higgs-to-top coupling and the Higgs self-coupling.	20
2.6	Feynman diagrams for the different HH production modes other than ggF, (a) vector boson fusion (VBF), (b) HH production in association with a top anti-top pair (ttHH), and (c) HH production in association with a vector boson (VHH).	21
2.7	The HH production cross-section for different production modes as a function of the centre of mass energy (\sqrt{s}) of p-p collisions.	22

2.8	The branching fractions of various HH decay modes, weighted with respect to the branching fraction of $HH \rightarrow b\bar{b}b\bar{b}$	22
2.9	Feynman diagrams for interaction between (a) a pair of Higgs bosons and a pair of top quarks, (b) a gluon pair and a Higgs boson, and (c) a gluon pair and a Higgs boson pair.	25
2.10	Feynman diagram for resonant HH production.	26
2.11	Feynman diagram for $B_s^0 \rightarrow \phi\phi$ decay.	28
3.1	The layout of the CERN accelerator complex.	31
3.2	The schematic of the LHC.	33
3.3	The peak instantaneous luminosity versus time as delivered by the LHC to the CMS experiment with stable beams in p-p collisions. The green, red, blue, purple, orange, sky blue and deep blue colours represent 2010, 2011, 2012, 2015, 2016, 2017 and 2018 data-taking periods respectively.	35
3.4	Average number of interactions per bunch crossing during 2016 data taking period.	36
3.5	The integrated luminosity delivered to the CMS experiment by the LHC with stable beams in p-p collisions. The green, red, blue, purple, orange, sky blue and deep blue colours represent 2010, 2011, 2012, 2015, 2016, 2017 and 2018 data taking periods respectively.	36
3.6	The layout of the CMS detector.	37
3.7	The layout of the CMS tracker.	40

3.8	Material budget of the CMS tracker as a function of tracker η , in units of radiation length. The maximum around $ \eta \sim 1.4$ is due to the presence of the service materials in that region.	40
3.9	(a) The hit efficiency vs instantaneous luminosity for the CMS pixel detector measured with 2016 data. (b) The hit efficiency vs instantaneous luminosity for the CMS Phase-1 pixel detector measured with 2018 data.	41
3.10	The p_T resolution of the simulated muon tracks as measured by the CMS tracker as a function of η , for muons of $p_T = 1$ (black), 10 (blue) and 100 GeV (red) [1]. The solid symbols represent the half-width containing 68% of the residual distribution around the mean value and stand for actual resolution. The open symbols represent the resolution if the 90% of the residual distribution around the mean value is considered and show the effect of the extreme values.	44
3.11	(a) Transverse and (b) longitudinal impact parameter resolution of the simulated muon tracks as a function of η for muons of $p_T = 1$ (black), 10 (blue) and 100 GeV (red) [1]. The solid symbols represent the half-width containing 68% of the residual distribution around the mean value and stand for actual resolution. The open symbols represent the resolution if the 90% of the residual distribution around the mean value is considered and show the effect of the extreme values.	45

3.12	(a) Tracking efficiency for muons coming from Z decay as a function of muon $ \eta $. (b) Tracking efficiency for muons coming from Z decay vs number of primary vertices reconstructed in an event. The black dots and light blue rectangles represent 2016 data and simulation respectively.	46
3.13	The layout of the CMS electromagnetic calorimeter.	47
3.14	The energy resolution of the electromagnetic calorimeter as measured in beam tests.	48
3.15	A longitudinal view of one quarter of the CMS detector in the $r - \eta$ plane. The layout shown is up-to the HCAL indicating the components of the HCAL: hadron barrel (HB), hadron outer (HO), hadron endcap (HE) and hadron forward (HF)	49
3.16	Layout of one quarter of the CMS detector. The components of the muon system: four DT chamber (MB1-MB4) in the barrel region, four CSC stations in the endcap (ME1-ME4) and RPC stations are shown in green, blue and red colours respectively.	51
3.17	The schematic representation of the CMS trigger/DAQ system.	53
3.18	A schematic representation of the CMS L1 trigger system.	54
3.19	Muon trigger efficiency of one of the muon trigger paths used in CMS as a function of (a) muon p_T and (b) muon η , as measured with 2016 data.	56

3.20	Electron trigger efficiency, measured with 2016 data, for several electron trigger paths used in CMS as a function of (a) electron p_T and (b) electron η . The <code>HLT_Ele25_eta2p1_WPTight</code> is used in this analysis which requires the presence of an electron of $p_T > 24 \text{ GeV}$ and $ \eta \leq 2.1$	57
3.21	Tau trigger efficiency measured with 2016 data, as a function of tau p_T , for the tau trigger path used in the $HH \rightarrow b\bar{b}\tau\tau$ analysis.	58
3.22	The delivered (blue filled region) and recorded (yellow filled region) integrated luminosity to the CMS experiment by the LHC, in p-p collisions during the 2016 data taking period.	59
4.1	Vertex resolution in (a) x direction and (b) z direction, as a function of the number of tracks associated to the vertices [1], using minimum bias and jet enriched events.	63
4.2	A transverse slice of the CMS detector highlighting interaction of different final state particles with the detector materials.	64
4.3	Muon reconstruction and identification efficiency for (a) loose and (b) tight muons as a function of η , measured with CMS data collected in 2015 [2].	70
4.4	Secondary vertex formation for the b-jets.	72
4.5	The b-tagging efficiency for (a) b-jets, (b) c-jets and (c) light quark and gluon jets respectively.	73

4.6	(a) τ_h identification efficiency as measured in the $Z/\gamma^* \rightarrow \tau\tau \rightarrow \mu\tau_h$ events and (b) Mis-identification efficiency of the jets as measured in the multi-jet events [3]. Values obtained for different MVA isolation discriminant working points are represented by different colours. The solid symbols represent the value obtained with 8 TeV CMS data corresponding to an integrated luminosity of 19.7 fb^{-1} . The open symbols represent the value obtained from the MC events.	75
4.7	(a) Mis-identification efficiency for electrons for different <i>against electron discriminant</i> working points, as measured in $Z/\gamma^* \rightarrow ee$ events [3]. (b) Mis-identification efficiency for muons for different <i>against muon discriminant</i> working points, as measured in $Z/\gamma^* \rightarrow \mu\mu$ events. [3]. The solid symbols represent the values obtained with 19.7 fb^{-1} 8 TeV CMS data. The open symbols represent the value obtained with MC events.	77
5.1	Feynman diagrams of various background processes to the $HH \rightarrow b\bar{b}\tau\tau$ final state, (a) $t\bar{t}$ + jets, (b) $Z/\gamma^* \rightarrow ll$ + jets, (c) di-boson, (d) single top, (e) W + jets, (f) Electroweak + two-jets, and (g) SM Higgs boson production.	80
5.2	Feynman diagrams for the SM HH production.	84
5.3	Different possible scenarios depending on the separation of the two b-quarks, (a) $\Delta R(b, b) > 0.8$, (b) $0.4 < \Delta R(b, b) < 0.8$ and (c) $\Delta R(b, b) < 0.4$. In all the cases, green and yellow cones represent AK4 jets and violet cones represent AK8 jet.	90

5.4	ROC curves for $t\bar{t}$ background rejection and signal efficiencies for (a) low-mass resonant production, (b) high-mass resonant production and (c) non-resonant production with low-mass BDT.	94
5.5	m_{T2} distribution for non-resonant HH signal events (solid red line) and $t\bar{t}$ background (solid blue line) [4]	97
5.6	A sketch of different regions used for the QCD background estimation. The charge of the τ pair is plotted along the x axis. while the isolation requirement on the τ candidates is plotted along the y axis.	99
5.7	$m_{\mu+\mu-}$ distribution for (a) $Z + 0$ b-tagged jet, (b) $Z + 1$ b-tagged jet, and (c) $Z + 2$ b-tagged jets categories. The black dots represent data and coloured filled histograms represent MC events. The MC events are stacked up. The ratio between data and MC is also shown.	102
5.8	$m_{\mu+\mu-}$ distribution after the simultaneous fit in (left) $Z + 0$ b-tagged jet, (centre) $Z + 1$ b-tagged jet and (right) $Z + 2$ b-tagged jets. The black dots represent data points, The solid blue lines represent the obtained pdf combining the three Drell-Yan MC templates. The dashed blue lines represent the MC template for all other backgrounds.	104

- 5.9 Distribution of the final discriminating variables for the $b\bar{b}\mu\tau_h$ final state. Panels a and d, show the distribution of m_{HH}^{KinFit} in the low-mass (LM) resonant signal region for resolved 1b1j and 2b categories respectively. Panels b and e show the distribution of m_{HH}^{KinFit} in the high-mass (HM) resonant signal regions for resolved 1b1j and 2b categories respectively. g shows the distribution of m_{HH}^{KinFit} in the resonant signal region for the boosted category. Panels c, f and h show the distribution of m_{T2} in the non-resonant signal region for resolved 1b1j, 2b and boosted categories respectively. Data are represented by points with error bars and expected signal contributions are represented by the solid (BSM HH signals) and dashed (SM non-resonant HH signal) lines. Expected background contributions (shaded histograms) and associated systematic uncertainties (dashed areas) are also shown. The background histograms are stacked. 105

5.10 Distributions of the final discriminating variables for the $b\bar{b}e\tau_h$ final state. Panels a and d show distribution of m_{HH}^{KinFit} in the low-mass (LM) resonant signal region for resolved 1b1j and 2b categories respectively. Panels b and e show distribution of m_{HH}^{KinFit} in the high-mass (HM) resonant signal regions for resolved 1b1j and 2b categories respectively. g shows distribution of m_{HH}^{KinFit} in the resonant signal region for the boosted category. Panels c, f and h show distribution of m_{T2} in the non-resonant signal region for resolved 1b1j, 2b and boosted categories respectively. Data are represented by points with error bars and expected signal contributions are represented by solid (BSM HH signals) and dashed (SM non-resonant HH signal) lines. Expected background contributions (shaded histograms) and associated systematic uncertainties (dashed areas) are also shown. The background histograms are stacked. 106

5.11	Distributions of the final discriminating variables for the $b\bar{b}\tau_h\tau_h$ final state. Panels a, c, e show distribution of m_{HH}^{KinFit} in the resonant signal region for resolved 1b1j, 2b and boosted categories respectively. Panels b, d and f show distribution of m_{T2} in the non-resonant signal region for resolved 1b1j, 2b and boosted categories respectively. Data are represented by points with error bars and expected signal contributions are represented by solid (BSM HH signals) and dashed (SM non-resonant HH signal) lines. Expected background contributions (shaded histograms) and associated systematic uncertainties (dashed areas) are also shown. The background histograms are stacked.	107
5.12	(a) 95% CL upper limits on the resonant HH production cross-section times branching fraction as a function of the resonant particle mass (m_S) [5]. The red line denotes the expectation for production of a radion. (b) Excluded regions in the $m_A - \tan\beta$ plane in the hMSSM scenario [5].	108
5.13	(c) 95% CL upper limits on the non-resonant HH production times branching fraction as a function of κ_λ/κ_t [5], (d) Excluded regions in the $\kappa_\lambda - \kappa_t$ plane [5].	109
6.1	The layout of the CMS Phase-2 tracker. The inner tracker is represented by green and yellow colours, while blue and red colours represent the outer tracker.	114
6.2	The concept of p_T discrimination.	116

6.3	The schematic of the tracklet based tracking algorithm. A portion of the barrel outer tracker in the $x - y$ view is shown. The blue and red lines represent PS and 2S modules respectively. The light blue stars represent stubs. (a) The formed seed or tracklet is represented by red stars. (b) A helical trajectory from the nominal interaction point is formed using the tracklet and the trajectory is propagated to other layers. (c) The matched stubs to the trajectory are represented by green stars.	118
6.4	A schematic diagram of the implementation of the tracklet algorithm in the hardware [6]. The red boxes represent the processing modules and the blue boxes are the memory blocks, where the data is stored. The data flows from left to right in the figure.	120
7.1	Block diagram of one of 254 channels of the CBC2 ASIC [7–9].	122
7.2	Block diagram of the CBC2 ASIC [7–9].	124
7.3	An irradiated 2S mini-module consisting of 254 strips and 2 CBC2s.	125
7.4	The current-voltage characteristics of a sensor of the irradiated mini-module before (red) and after (black) irradiation to $6 \times 10^{14} n_{eq}/cm^2$ which shows an increase in leakage current after irradiation. The measurements before and after irradiation were taken at 20°C and -20°C respectively.	126
7.5	The full-sized 2S module used in the test beam.	127

- 7.6 The schematic diagram of the CERN test beam setup. The four scintillators used to generate the trigger, the six MIMOSA-26 planes and the fast timing plane equipped with the FE-I4 chip are shown. The prototype detector under test (DUT) is placed within the telescope system as shown. 127
- 7.7 (a) Cluster formation from multiple hits in a single sensor. The big yellow rectangle represents the sensor. The strips with no hit are represented by the blue rectangles and the strips with a hit are represented by the green rectangles. Multiple adjacent hits with no gap in between are grouped together to form a cluster. (b) Stub formation from two clusters in two sensors. 130
- 7.8 Average number of hits per event for non-irradiated and irradiated mini-modules as a function of V_{CTH} . A bias voltage of 250 V (600 V) was applied to the non-irradiated (irradiated) module. 132
- 7.9 Average number of clusters per event for non-irradiated and irradiated mini-modules as a function of V_{CTH} . A bias voltage of 250 V (600 V) was applied to the non-irradiated (irradiated) module. 133
- 7.10 Differential cluster occupancy for non-irradiated and irradiated mini-modules as a function of V_{CTH} . A bias voltage of 250 V (600 V) was applied to the non-irradiated (irradiated) module. 135

- 7.11 Stub efficiency for the irradiated (blue) and non-irradiated (red) mini-modules as a function of the incident angle (top x-axis) or the effective p_T (bottom x-axis). As expected, for large angle of incidence, which corresponds to low effective p_T , the stub efficiency drops. A radius of 60 cm is used to calculate p_T . The stub correlation window is set to 5 strips. 136
- 7.12 Comparison of stub efficiency for different angular scans with different correlation windows for the irradiated mini-module. The incident angle is shown in top x-axis and the effective p_T is shown in bottom x-axis. The choice of window size leads to a shift in the turn-on p_T , but the efficiency at the plateau remains the same. A bias voltage of 600 V was applied to the irradiated mini-module. 138
- 7.13 Stub efficiency of a full-sized 2S module. The module was operated at a bias voltage of 250 V and the V_{CTH} value was set to 115 DAC units. (a) Stub efficiency per strip and (b) stub efficiency per CBC computed using data from strips scanned by the beam. 139
- 8.1 True p_T of the softest kaon in generated $B_s^0 \rightarrow \phi\phi \rightarrow 4$ Kaons events. 142
- 8.2 (a) d_z between all the oppositely charged track pairs, (b) d_{xy} between all the track pairs having opposite charges and $|d_z| \leq 1$ cm for $\langle \text{PU} \rangle = 200$. The distributions are normalised to unit area. The dashed blue and solid red histograms correspond to the Offline and L1 signal events respectively, while the green filled area represents the background events. 145

- 8.3 Invariant mass distribution of all the tracks pairs, having opposite charges, $|d_z| \leq 1 \text{ cm}$ and $d_{xy} \leq 1 \text{ cm}$ for $\langle \text{PU} \rangle = 200$. The distributions are normalised to unit area. The dashed blue and solid red histograms correspond to the Offline and L1 signal events respectively while the green filled area represents the background events. 146
- 8.4 (a) $\Delta R(\phi\text{-pair})$ distribution for all the ϕ -pairs, with $|d_z|(\phi\text{-pair}) \leq 1 \text{ cm}$ and $d_{xy}(\phi\text{-pair}) \leq 1 \text{ cm}$, (b) $\Delta R(K^+K^-)$ distribution of the ϕ candidates, which form ϕ pairs with $|d_z|(\phi\text{-pair}) \leq 1 \text{ cm}$, $d_{xy}(\phi\text{-pair}) \leq 1 \text{ cm}$ and $0.2 \leq \Delta R(\phi\text{-pair}) \leq 1$, for $\langle \text{PU} \rangle = 200$. The distributions are normalised to unit area. The dashed blue and solid red histograms correspond to the Offline and L1 signal events respectively, while the green filled area represents the background events. 147
- 8.5 Invariant mass distribution of all the ϕ -pairs, with $|d_z| \leq 1 \text{ cm}$, $d_{xy} \leq 1 \text{ cm}$, $0.2 \leq \Delta R(\phi\text{-pair}) \leq 1.0$ and $\Delta R(K^+K^-) \leq 0.12$, for $\langle \text{PU} \rangle = 200$. The distributions are normalised to unit area. The dashed blue and solid red histograms correspond to the Offline and L1 signal events respectively, while the green filled area represents the background events. 148
- 8.6 Signal efficiency and trigger rate for different selection baselines and for different pileup scenarios. Uncertainties are statistical only. 150

- 8.7 p_T of the four (kaon) tracks that from the selected B_s^0 candidates, ordered in terms of descending p_T for $\langle \text{PU} \rangle = 200$. The events are selected with the medium baseline. The distributions are normalised to unit area. The dashed blue and solid red histograms correspond to the Offline and L1 signal events respectively, while the green filled area represents the background events. 151
- 8.8 Number of ϕ candidates reconstructed in an event, for medium baseline and $\langle \text{PU} \rangle = 200$. The distributions are normalised to unit area. The dashed blue and solid red histograms correspond to the Offline and L1 signal events respectively, while the green filled area represents the background events. 152
- 8.9 Transverse momentum of the two reconstructed ϕ candidates which form the selected B_s^0 candidate, for medium baseline and $\langle \text{PU} \rangle = 200$. The distributions are normalised to unit area. The dashed blue and solid red histograms correspond to the Offline and L1 signal events respectively, while the green filled area represents the background events. 152
- 8.10 Transverse momentum of the selected B_s^0 candidate, for medium baseline and $\langle \text{PU} \rangle = 200$. The distributions are normalised to unit area. The dashed blue and solid red histograms correspond to the Offline and L1 signal events respectively, while the green filled area represents the background events. 153

- 8.11 ROC curve of signal efficiency vs trigger rate due to variation of $|d_z|$ between a pair of tracks over the range 0.3 – 1.0 cm for $\langle \text{PU} \rangle = 140$ and 200. 155
- 8.12 ROC curves of signal efficiency vs trigger rate due to variation of L1 tracking p_T threshold on the lowest- p_T kaon track of the B_s^0 candidates over the range 2 – 3 GeV for $\langle \text{PU} \rangle = 140$ and 200. Green, blue and red lines correspond to loose, medium and tight selection baselines respectively. Uncertainties are statistical only. 157

List of Tables

2.1	The lepton sector of the Standard Model [10].	7
2.2	The quark sector of the Standard Model [10].	7
2.3	The gauge sector of the Standard Model.	8
3.1	Single muon trigger paths used in the $HH \rightarrow b\bar{b}\tau\tau$ analysis.	55
4.1	Details of the input variables used in the electron identification classifier.	66
4.2	Minimum BDT scores required for electron identification for tight and loose WPs.	66
4.3	b-Tagging working points and corresponding threshold on the CSV discriminant.	72
5.1	Trigger paths used for the $b\bar{b}\mu\tau_h$, $b\bar{b}e\tau_h$ and $b\bar{b}\tau_h\tau_h$ final states.	81
5.2	The BSM shape benchmark points for the non-resonant $HH \rightarrow b\bar{b}\tau\tau$ production [11; 12].	85
5.3	SM shape benchmark points for non-resonant $HH \rightarrow b\bar{b}\tau\tau$ production.	85
5.4	Selection conditions for the τ_h candidate for different final states. . . .	87
5.5	Jet selection criteria.	89

5.6	Scale factors for normalisation of Drell-Yan + jets background.	101
5.7	Systematic uncertainties, which affect normalisation of different processes.	103
5.8	Systematic uncertainties, which affect shape of distributions for different processes.	103
6.1	Main parameters of the 2S and PS modules of the proposed CMS Phase-2 tracker [6].	115
7.1	Details of modules used in various test beams at CERN.	124
8.1	Baseline event selection conditions.	149
8.2	Signal efficiency and trigger rate for loose, medium and tight working points respectively for $\langle \text{PU} \rangle = 140$. Uncertainties are statistical only.	149
8.3	Signal efficiency and trigger rate for loose, medium and tight working points respectively for $\langle \text{PU} \rangle = 200$. Uncertainties are statistical only.	150
8.4	Signal efficiency and trigger rate as a function of the $ d_z $ cut between the pair of tracks, for $\langle \text{PU} \rangle = 200$. Uncertainties are statistical only.	153
8.5	Signal efficiency and trigger rate as a function of the $ d_z $ cut between the pair of tracks, for $\langle \text{PU} \rangle = 140$. Uncertainties are statistical only.	154
8.6	Signal efficiency and trigger rate as a function of L1 tracking p_T threshold on the lowest- p_T kaon track of the B_s^0 candidates, for medium baseline selection and $\langle \text{PU} \rangle = 200$. Uncertainties are statistical only.	156
10.1	The single muon datasets, used in the $HH \rightarrow b\bar{b}\tau\tau$ analysis, for the $b\bar{b}\mu\tau_h$ final state.	163

10.2	The single electron datasets, used in the $HH \rightarrow b\bar{b}\tau\tau$ analysis, for the $b\bar{b}e\tau_h$ final state.	164
10.3	The tau datasets, used in the $HH \rightarrow b\bar{b}\tau\tau$ analysis, for the $b\bar{b}\tau_h\tau_h$ final state.	164
10.4	Drell-Yan + jets and W + jets background datasets.	165
10.5	Di-boson and the SM Higgs background datasets.	166
10.6	Electroweak background datasets	167
10.7	$t\bar{t}$ and Single top background datasets	168
10.8	List of resonant spin-0 signal samples.	168
10.9	List of resonant spin-2 signal samples.	169
10.10	List of non-resonant signal samples.	169

Chapter 1

Introduction

The Standard Model (SM) of particle physics studies the fundamental constituents of matter and their interactions, namely, strong, weak and electromagnetic. Numerous collider and non-collider experiments have substantiated the predictions of the SM with great precision. With the discovery of the Higgs boson at the Large Hadron Collider (LHC) in 2012, the SM is regarded as the most successful theory of particle physics.

The discovery of the Higgs boson at a mass, $m_H = 125.09 \pm 0.21$ (stat.) ± 0.11 (syst.) GeV , by A Toroidal LHC ApparatuS (ATLAS) [13] and Compact Muon Solenoid (CMS) [14] experiments [15–17], was followed by measurements of the Higgs boson properties like mass, spin and parity which have been found to be in agreement with the SM predictions [18]. At present, search for pair production of the Higgs bosons (HH) in all the possible final states is the main focus at the LHC, which will allow one to measure the Higgs trilinear self-coupling [19]. The search for HH

production also probes the effect of physics beyond the Standard Model (BSM) [20–30]. In this thesis, results of a search for HH production in the $HH \rightarrow b\bar{b}\tau\tau$ final state, which has a good trade-off between signal yield and background contamination, have been presented.

The LHC will undergo a major upgrade during 2025-27 to achieve instantaneous luminosities that will be higher than the current value of $10^{34} \text{ cm}^{-2} \text{ s}^{-1}$ by a factor of 5 – 7. The upgraded High Luminosity LHC (HL-LHC) is expected to deliver $\sim 300 \text{ fb}^{-1}$ of data each year to both ATLAS and CMS experiments. However, such an increase in the instantaneous luminosity will also lead to a steep increase in the average number of additional pile-up (PU) interactions from the current value of 40 – 50 to 140 – 200. As a consequence, the trigger rates in the individual experiments will increase significantly. In order to function efficiently in the extremely harsh radiation conditions of the HL-LHC, the CMS detector will have to go through a series of upgrades (CMS Phase-2 upgrade). The current tracker will be replaced with a new one with increased radiation hardness, reduced material budget, higher granularity and longer trigger latency. The new tracker will be equipped with detector modules capable of selecting high- p_T tracks at the detector front-end itself, to allow CMS to include tracking information in the Level1 (L1) trigger system. This is crucial for CMS to keep the L1 trigger rate at an acceptable range while retaining the full physics potential. Availability of tracks at L1 will also allow CMS to trigger on low- p_T , fully hadronic final states, like $B_s^0 \rightarrow \phi\phi \rightarrow 4 \text{ Kaons}$, for the first time. The CMS Phase-2 outer tracker will be equipped with two kinds of modules, namely, Pixel-Strip (PS) and Strip-Strip (2S) modules. The performance of the prototype 2S

modules have been studied under realistic beam conditions.

The thesis is organised in the following way. An overview of the Standard Model of Particle physics, and theoretical aspects of HH production and decay into the $b\bar{b}\tau\tau$ final state, flavour physics and the $B_s^0 \rightarrow \phi\phi \rightarrow 4$ Kaons process, will be presented in Chapter 2. A brief overview of the LHC, the CMS detector, trigger and Data Acquisition (DAQ) systems, and Monte-Carlo event generation will be described in Chapter 3 which will be followed by a discussion about reconstruction and identification of various physics objects in CMS in Chapter 4. The analysis method and results of a search for $HH \rightarrow b\bar{b}\tau\tau$ using data collected by CMS in 2016, corresponding to an integrated luminosity of 35.9fb^{-1} , will be discussed in Chapter 5.

A brief discourse on the HL-LHC, and CMS Phase-2 upgrade, in particular the CMS Phase-2 tracker upgrade and Level1 tracking will be a part of Chapter 6. Results obtained from the analysis of test beam data of the prototype 2S modules will be discussed in Chapter 7. A study of the potential of CMS at the HL-LHC to trigger on $B_s^0 \rightarrow \phi\phi \rightarrow 4$ Kaons events with the help of L1 tracking, will be described in Chapter 8.

Chapter 2

The Standard Model of Particle Physics

A brief overview of the Standard Model (SM) of particle physics and the theoretical aspects related to the work presented in this thesis, namely, pair production of the Higgs boson, measurement of the Higgs trilinear self-coupling and search for physics beyond the SM in Higgs boson pair production, will be discussed in this chapter. Importance of rare, low- p_T processes, such as $B_s^0 \rightarrow \phi\phi \rightarrow 4$ Kaons, in the context of search for new physics beyond the direct reach of the Large Hadron Collider (LHC), will also be discussed.

2.1 The Standard Model of Particle Physics

The Standard Model of particle physics is a description of the elementary particles and their interactions based on quantum field theory and is currently the most suc-

successful theory of particle physics. In the SM, the fundamental constituents of matter are fermions, i.e. particles with spin $1/2$. Interactions between the matter particles are mediated by the exchange of gauge bosons, which are particles with spin 1. Three of the four fundamental interactions, i.e. strong, electromagnetic and weak, are described by the SM.

The fermions in the SM are further classified in lepton and quark sectors based on the type of their interaction. The lepton sector, shown in Table 2.1, consists of three generations of particles, namely electron, muon and tau and the associated neutrinos. The leptons carry an electrical charge of -1 , measured in the units of absolute value of electron charge (e). The mass of electron, muon and tau are shown in the same table. The neutrinos do not have electric charge and are considered as massless in the SM [31]. However, experimental measurements show that the neutrinos carry a tiny mass. The current upper limits on the neutrino masses are also shown in Table 2.1. For each charged lepton, there is an associated anti-particle with the same mass but opposite electric charge. Neutrinos are hypothesised as Majorana fermions which are their own anti-particles. Majorana neutrinos are characterised by the property that the neutrino and antineutrino could be distinguished only by chirality.

The charged leptons interact through electromagnetic and weak forces, whereas the neutrinos participate in weak interactions only.

The quark sector, shown in Table 2.2, consists of six quarks organised in three generations. The up (u), charm (c) and top (t) quarks have an electric charge of $+2/3 e$, whereas, the down (d), strange (s) and bottom (b) quarks have an electric charge of $-1/3 e$. The quark masses are shown in the same table. Each quark has an

associated anti-particle with the same mass but opposite electric charge. The quarks participate in strong, electromagnetic and weak interactions. The quarks carry the so-called colour charge, which is the quantum number associated with the strong interaction. The quarks and anti-quarks carry opposite colour charges. The quarks are not observed in nature as isolated particles, but are confined in colour singlet bound states as hadrons, e.g. proton, neutron etc.

Charge (+1)	electron (e)	muon (μ)	tau (τ)
Mass	$0.511 \pm 0.0000000031 \text{ MeV}$	$105.7 \pm 0.0000024 \text{ MeV}$	$1.777 \pm 0.00012 \text{ GeV}$
Charge (0)	electron neutrino (ν_e)	muon neutrino (ν_μ)	tau neutrino (ν_τ)
Mass	$< 1.1 \text{ eV}$	$< 0.17 \text{ MeV}$	$< 15.5 \text{ MeV}$

Table 2.1: The lepton sector of the Standard Model [10].

Charge ($+\frac{2}{3}$)	up (u)	charm (c)	top (t)
Mass	$2.16^{+0.49}_{-0.26} \text{ MeV}$	$1.27 \pm 0.02 \text{ GeV}$	$172.76 \pm 0.30 \text{ GeV}$
Charge ($-\frac{1}{3}$)	down (d)	strange (s)	bottom (b)
Mass	$4.67^{+0.48}_{-0.17} \text{ MeV}$	$93^{+11}_{-5} \text{ MeV}$	$4.18^{+0.03}_{-0.02} \text{ GeV}$

Table 2.2: The quark sector of the Standard Model [10].

The gauge bosons, associated to the strong, electromagnetic and weak forces, along-with the relative strength and range of the three interactions are shown in Table 2.3,

A neutral fundamental scalar particle, the Higgs boson, was introduced in the SM to generate the mass of the gauge bosons and fermions. The Higgs boson was discovered by the ATLAS [13] and CMS experiments [14] at the LHC in 2012 [15; 16], which is one of the most notable achievements of particle physics in recent years. The

Interactions	Strong	Electromagnetic	Weak	
Relative Strength	≈ 1	$\frac{1}{137}$	10^{-6}	
Range (m)	$10^{-15} - 10^{-16}$	∞	10^{-18}	
Gauge bosons	gluons (g)	photon (γ)	W^\pm	Z
Mass (GeV)	massless	massless	80.379 ± 0.012	91.1876 ± 0.021

Table 2.3: The gauge sector of the Standard Model.

experimentally measured value of the mass of the Higgs boson is $m_H = 125.09 \pm 0.21 (stat.) \pm 0.11 (syst.) GeV$ [17]. The Higgs boson interacts with the fermions with an interaction strength or coupling proportional to the fermion mass. For Higgs boson interaction with the gauge bosons, the coupling is proportional to the squared mass of the gauge bosons.

2.2 The Symmetry group of the Standard Model

Symmetry has always been the guiding principle behind the construction of the SM, which is expressed mathematically by the group theory [32]. The group structure of the fundamental interactions described by the SM can be stated as,

$$SU(3)_C \times SU(2)_L \times U(1)_Y \quad (2.1)$$

where,

- $SU(3)_C$ represents the symmetry group associated to the strong interaction. The subscript C represents the colour quantum number.
- The $SU(2)_L \times U(1)_Y$ group stands for electroweak interaction (unification of

weak and electromagnetic interactions). The subscript L in $SU(2)_L$ refers to the left-chiral fields. Only the left-chiral fermionic fields form doublets under the $SU(2)_L$ group. The subscript Y in $U(1)_Y$ represents the weak hypercharge (Y).

2.3 Quantum Electrodynamics

The electromagnetic interaction between the charged particles, which takes place through exchange of photons, is described by Quantum Electrodynamics (QED) [33]. The Lagrangian of a free Dirac fermion [33] of mass m is as follows,

$$\mathcal{L} = \bar{\psi}(i\not{\partial} - m)\psi \quad (2.2)$$

where,

- ψ is the fermionic field
- $\bar{\psi}$ is $\psi^\dagger\gamma_0$
- $\not{\partial}$ is $\gamma^\mu\partial_\mu$, γ^μ being the Dirac matrices

The Lagrangian of Equation 2.2 is invariant under a global $U(1)$ transformation, i.e.

$$\psi \xrightarrow{U(1)} \psi' = \exp(-ieQ\theta)\psi \quad (2.3)$$

where,

- e is the electron charge
- Q is the charge of the fermion, measured in the units of electron charge
- θ , the phase of the $U(1)$ transformation, is a constant over space-time ($\frac{\partial\theta}{\partial x} = 0$)

If θ is considered to be a function of space-time (denoted by $\theta(x)$), the Lagrangian of Equation 2.2 no more remains invariant under the $U(1)$ transformation. In order to preserve such invariance, the partial derivative in Equation 2.2 has to be replaced by the covariant derivative, defined as,

$$D_\mu = \partial_\mu + ieQA_\mu \quad (2.4)$$

where, a new vector field A_μ has been introduced which transforms under the local $U(1)$ transformation as,

$$A_\mu \xrightarrow{U(1)} A'_\mu = A_\mu + \partial_\mu\theta(x) \quad (2.5)$$

The field A_μ can be identified as the photon field. The free photon field is represented by $-\frac{1}{4}F_{\mu\nu}F^{\mu\nu}$ in the Lagrangian, where $F_{\mu\nu} = \partial_\mu A_\nu - \partial_\nu A_\mu$. The total Lagrangian for QED can now be written as,

$$\mathcal{L}_{QED} = \bar{\psi}(i\not{D} - m)\psi - \frac{1}{4}F_{\mu\nu}F^{\mu\nu} \quad (2.6)$$

where $\not{D} = \gamma^\mu D_\mu$. The Lagrangian in Equation 2.6 is invariant under local $U(1)$ transformations and contains, in addition to the free terms, a term $eQ\bar{\psi}\gamma^\mu\psi A_\mu$, which represents the interaction between a charged fermion and a photon. Therefore,

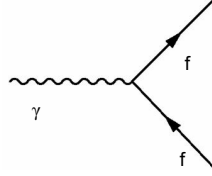


Figure 2.1: Feynman diagram for interaction between a charged fermion and a photon.

electromagnetic interaction is considered to arise from the requirement of local $U(1)$ gauge invariance. A mass term for the photon field of type $A_\mu A^\mu$ is prohibited by the gauge invariance. In the following sections, the $U(1)$ symmetry group of the electromagnetic interaction will be represented by $U(1)_{em}$ to avoid any confusion with the $U(1)_Y$ group.

The Feynman diagram [33] for interaction between a Dirac fermion and the photon field A_μ , at the lowest order of perturbation theory, is shown in Figure 2.1 where the associated vertex factor is $-ieQ\gamma^\mu$.

2.4 Quantum Chromodynamics

The strong interaction between quarks and gluons is described by the Quantum Chromodynamics (QCD) [33]. The quarks carry a colour quantum number and form triplets under the $SU(3)_C$ group of strong interaction. Requirement of the local $SU(3)$ gauge invariance gives rise to interaction between coloured quarks and gluons. There are eight massless gluons corresponding to eight generators of the $SU(3)_C$ group. Due to the non-abelian nature of the $SU(3)_C$ group, gluons can also interact with themselves.

Several Feynman diagrams depicting basic QCD interactions are shown in Figure 2.2.

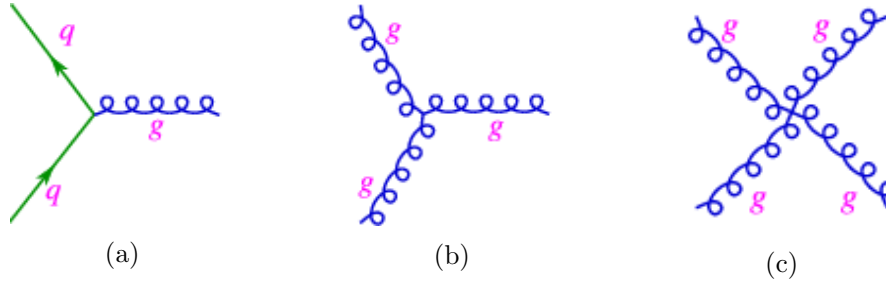


Figure 2.2: Feynman diagrams for QCD interactions, (a) quark-gluon interaction, (b) gluon trilinear self-interaction and (c) gluon quartic self-interaction.

2.5 Weak interactions and the standard Electroweak theory

The weak force responsible for the nuclear β decay was first explained by E. Fermi with a simple model [34], where it was considered as a point-like four fermion interaction. Though the Fermi theory was able to explain low energy weak interactions, the theory was not renormalizable. While trying to overcome the problems of the Fermi theory, physicists hypothesised that the weak interaction is mediated by intermediate vector bosons [35; 36], much like the electromagnetic interaction which is mediated by photons. However, it was also understood that the short-range nature of the weak interaction would mean that the intermediate vector bosons are massive. Spontaneous symmetry breaking and the Higgs mechanism, provide a way to generate the mass of the vector bosons protecting both the gauge symmetry and renormalizability

of the theory. This idea has been successfully employed by S. Glashow, A. Salam and S. Weinberg to unify the electromagnetic and weak interactions to develop the standard electroweak theory [35; 37; 38].

The electroweak interaction is described by the $SU(2)_L \times U(1)_Y$ symmetry group. The gauge bosons of the electroweak interactions are obtained from three generators of the $SU(2)_L$ group and one generator of the $U(1)_Y$ group. The W^\pm bosons are obtained from two different combinations of the first two generators of the $SU(2)_L$ group, whereas, two different combinations of the third generator of the $SU(2)_L$ group and the single generator of the $U(1)_Y$ group give rise to the Z boson and photon.

The quantum number associated to the $U(1)_Y$ group is called the weak hypercharge (Y). The electric charge (Q), the quantum number associated to the third generator of the $SU(2)_L$ group (T_3) and weak hypercharge (Y) are related as follows,

$$Q = T_3 + Y \tag{2.7}$$

The left- and right-chiral fermions behave differently in weak interactions. Under the $SU(2)_L$ group, the left-chiral fermions form doublets, whereas the right-chiral fermions form singlets. The leptons, under the $SU(2)_L \times U(1)_Y$ group, are represented as,

$$\begin{pmatrix} \nu_L \\ l_L \end{pmatrix} \tag{2.8}$$

l_R

where, l stands for electron, muon or tau lepton, and ν represents the associated

neutrino. The subscript L stands for the left-chiral fields and R stands for the right-chiral fields. There is no right-chiral neutrino in the SM, else a mass term for the neutrinos would have to be added in the SM Lagrangian. Since, the W bosons are formed from the first two generators of the $SU(2)_L$ group, they only interact with the left-chiral fields. The Z boson and photon can interact with both the left- and right-chiral fields.

Similarly, the quarks, under the $SU(2)_L \times U(1)_Y$ group, are represented as :

$$\begin{aligned} & \begin{pmatrix} u_L \\ d'_L \end{pmatrix}, \begin{pmatrix} c_L \\ s'_L \end{pmatrix}, \begin{pmatrix} t_L \\ b'_L \end{pmatrix} \\ & \qquad u_R, c_R, t_R \\ & \qquad d'_R, s'_R, b'_R \end{aligned} \tag{2.9}$$

where, again, the left-chiral fields are grouped together, since they form doublets under the $SU(2)_L$ group, and the right-chiral fields are kept separate, since they form singlets under the $SU(2)_L$ group. In general, the mass or physical eigenstates of the quarks do not overlap with the weak interaction eigenstates. Without loss of generality, the mass and weak interaction eigenstates can be assumed to be identical for the up type quarks. The weak interaction eigenstate of each down type quark is considered as superposition of mass eigenstates of all three down type quarks. The prime used for the down type quarks signifies that they are the weak interaction eigenstates, not the mass eigenstates. As a result, the W boson mediated interactions can involve quarks from two different generations which is known as quark mixing as introduced by N. Cabibbo [39]. The phenomenon of quark mixing leads to CP

violation, as demonstrated by M. Kobayashi and T. Maskawa [40]. The amplitude of the quark mixing is denoted by the Cabibbo-Kobayashi-Maskawa (CKM) matrix given below,

$$V = \begin{pmatrix} V_{ud} & V_{us} & V_{ub} \\ V_{cd} & V_{cs} & V_{cb} \\ V_{td} & V_{ts} & V_{tb} \end{pmatrix} \quad (2.10)$$

2.6 Spontaneous Symmetry Breaking and the Brout-Englert-Higgs Mechanism

Spontaneous Symmetry Breaking (SSB) occurs, when a Lagrangian is invariant under a symmetry group, but the ground state of the Lagrangian is not. According to the Nambu-Goldstone theorem [41; 42], if a Lagrangian is invariant under a continuous symmetry group having n generators, and if the ground state of the Lagrangian is symmetric under a continuous group containing n' generators, $n - n'$ massless states should be present in the spectrum. If the Lorentz symmetry remains unbroken, the new states have to be scalar, known as the Goldstone bosons. The Goldstone theorem is valid for spontaneously broken symmetries also. However, for local gauge theories, the Brout-Englert-Higgs Mechanism (or Higgs mechanism in short) [43–46] is required to generate the mass of the gauge boson which states that, for spontaneously broken gauge symmetries, the Goldstone bosons do not appear in the physical spectrum of the theory, but combines with the gauge bosons. As a result, after the SSB, a number of gauge bosons, which is equal to the number of Goldstone bosons that disappear, acquire mass.

For the electroweak theory, the SSB is realised by an $SU(2)_L$ scalar doublet,

$$\phi = \begin{pmatrix} \phi_1 \\ \phi_2 \end{pmatrix} \quad (2.11)$$

The Lagrangian of the scalar doublet can be expressed as,

$$\mathcal{L} = (D_\mu \phi)^\dagger (D^\mu \phi) - V(\phi) \quad (2.12)$$

where,

- D_μ is the covariant derivative, considering $SU(2)_L \times U(1)_Y$ symmetry
- $V(\phi)$ is the potential term for the scalar doublet, a general form of which is,

$$V(\phi) = \mu^2 \phi^\dagger \phi + \lambda (\phi^\dagger \phi)^2; \lambda > 0 \quad (2.13)$$

Depending upon the value of μ^2 , there are two possibilities with the potential,

- case $\mu^2 > 0$, where the minimum of the potential occurs at $\phi_1, \phi_2 = 0$ and no spontaneous symmetry breaking occurs.
- case $\mu^2 < 0$, where the minima of the potential appears at $|\phi_1|^2 + |\phi_2|^2 = v^2/2$, where $v = \sqrt{-\frac{\mu^2}{\lambda}}$ is known as the vacuum expectation value (vev). The system can choose any of the infinite number of degenerate minima. For simplicity, we consider that the system chooses the minima $\phi_1 = 0$, and $\phi_2 = v/\sqrt{2}$. The

field ϕ can be expanded around the vev by a perturbation,

$$\phi = \frac{1}{\sqrt{2}} \begin{pmatrix} 0 \\ v + H(x) \end{pmatrix} \quad (2.14)$$

where, the field $H(x)$ corresponds to a physical Higgs boson. In Equation 2.14, the unitary gauge is chosen such that the Goldstone components in the scalar field is zero. Replacing ϕ by H in the Lagrangian of Equation 2.12 will break the $SU(2)_L \times U(1)_Y$ symmetry and the new Lagrangian will only be symmetric under the $U(1)_{em}$ group, which remains unbroken. The $SU(3)_C$ group of the strong interaction also remains unbroken throughout the symmetry breaking process. The new field H , obtained after the symmetry breaking, can be identified as the Higgs boson.

The W and Z bosons acquire mass through the Higgs Mechanism after the spontaneous symmetry breaking. The gluons and photon remain massless, since the $SU(3)_C$ and $U(1)_{em}$ groups remain unbroken. The Yukawa interaction between the fermions and the $SU(2)_L$ scalar doublet leads to the mass terms for the fermions after the symmetry breaking. The value of vev, which is a free parameter of the theory, has a value of 246 GeV [47].

The Higgs boson can interact with the gauge bosons, with a vertex probability proportional to the square of the gauge bosons mass. Similarly, interaction of the Higgs boson with the fermions is specified by a coupling factor proportional to the fermion mass. The Feynman diagrams of the interaction of the Higgs boson with the gauge bosons and fermions are shown in Figure 2.3.

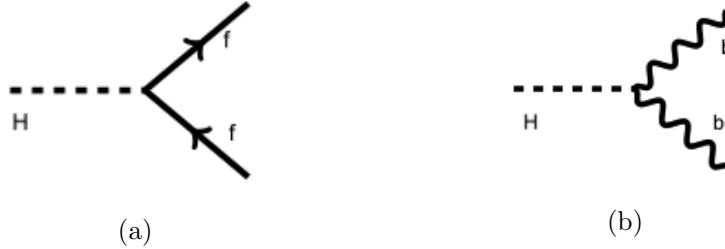


Figure 2.3: (a) Higgs to fermions vertex and (b) Higgs to gauge bosons vertex

The Higgs boson has been discovered by the ATLAS [13] and CMS experiments [14] at the LHC in 2012 [15; 16]. The mass of the Higgs boson is a free parameter of the theory and has been experimentally measured to be $m_H = 125.09 \pm 0.21 (stat.) \pm 0.11 (syst.) GeV$ [17]. Following the discovery of the Higgs boson, measurement of the properties of the particle, namely spin, parity etc. is of prime importance at the LHC. The measured properties of the Higgs boson are found to agree with the Standard Model predictions [18].

2.7 The Higgs self-interaction

In the SM, the Higgs boson can interact with itself leading to Higgs trilinear and quartic self-interactions, as shown in the Feynman diagrams in Figures 2.4a, and 2.4b. The Higgs trilinear and quartic self-couplings are denoted by, λ_{HHH} and λ_{HHHH} respectively.

The measurement of the Higgs boson self-couplings is an independent test of the SM. Both the self-couplings depend on the Higgs mass and are precisely predicted in the SM to have small values. Measurement of the Higgs boson self-couplings at the



Figure 2.4: Higgs self-interaction (a) trilinear, and (b) quartic.

LHC is, therefore, very challenging. As the SM predicted value of the Higgs boson trilinear and quartic self-couplings are $\lambda_{HHH} = \frac{m_H^2}{2v^2}$ and $\lambda_{HHHH} = \frac{m_H^2}{8v^2}$ respectively, the focus of the LHC is to probe the Higgs boson trilinear self-coupling only. For simplicity, in the following text, the trilinear self-coupling is denoted by λ .

2.8 HH production

The Feynman diagrams for HH production through the ggF process are shown in Figure 2.5. In Figure 2.5a, HH is produced through an intermediate top loop via the Higgs-to-top coupling (y_t), whereas, in Figure 2.5b, the Higgs boson pair is produced via both the Higgs-to-top coupling and the Higgs self-coupling. Measurement of the HH production cross-section is, therefore, an important handle to measure the Higgs self-coupling [19].

Feynman diagrams for the other HH production modes, like vector boson fusion (VBF), HH in association with the top anti-top pair (ttHH) and HH in association with a vector boson (VHH), are shown in Figure 2.6. The HH production

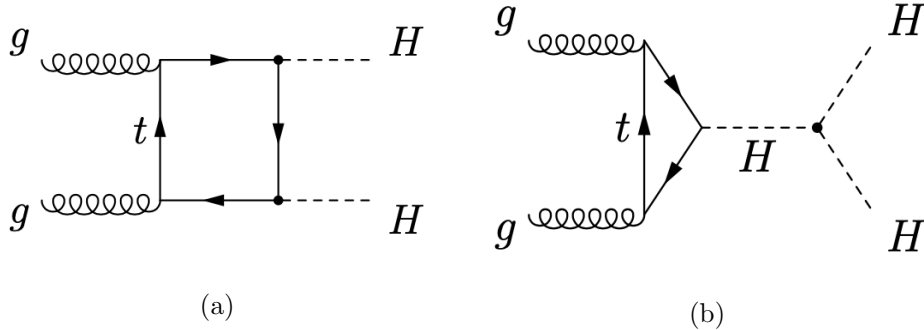


Figure 2.5: Feynman diagrams for HH production at the LHC through the ggF process. (a) HH produced solely via the Higgs-to-top coupling (y_t), and (b) HH produced by both the Higgs-to-top coupling and the Higgs self-coupling.

cross-section for different production modes, as a function of the centre of mass energy of p-p collisions, is shown in Figure 2.7. From the figure it can be seen that the HH production cross-section is dominated by the ggF production mode. For simplicity, search for HH production is restricted to the ggF production mode only. The SM predicted value of HH production cross-section in the ggF mode, at a centre of mass energy, $\sqrt{s} = 13\text{TeV}$, is $\sigma_{HH} = 33.49^{+4.3\%}_{-6.0\%} (\text{scale}) \pm 5.9\% (\text{theo}) \text{fb}$ [48–52], calculated at the next-to-next-to-leading order (NNLO) of the perturbative calculation, including next-to-next-to leading logarithm (NNLL) corrections and finite top quark mass effects.

2.9 HH decay

The branching fractions of various HH decay modes, weighted with respect to the branching fraction of $HH \rightarrow b\bar{b}b\bar{b}$, is shown in Figure 2.8.

Analyses of Higgs pair production have focussed on final states where at least

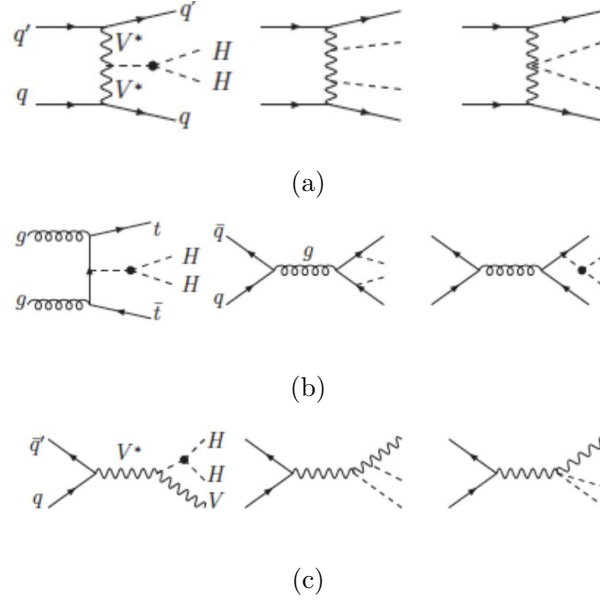


Figure 2.6: Feynman diagrams for the different HH production modes other than ggF , (a) vector boson fusion (VBF), (b) HH production in association with a top anti-top pair ($ttHH$), and (c) HH production in association with a vector boson (VHH).

one Higgs decays to $b\bar{b}$. The $HH \rightarrow b\bar{b}b\bar{b}$ has the highest branching fraction of $\mathcal{B}(HH \rightarrow b\bar{b}b\bar{b}) = 33.6\%$, but at the same time the channel has a very large background due to the presence of four jets in the final state. The $HH \rightarrow b\bar{b}\gamma\gamma$ decay has the cleanest signature among the relevant HH final states in the CMS detector due to the presence of two high energy photons. However, the final state suffers from a small branching fraction of $\mathcal{B}(HH \rightarrow b\bar{b}\gamma\gamma) = 0.26\%$. The $HH \rightarrow b\bar{b}\tau\tau$ final state, that can be experimentally studied with a moderately high efficiency due to the presence of a tau lepton pair in the final state, has a branching fraction of $\mathcal{B}(HH \rightarrow b\bar{b}\tau\tau) = 7.3\%$. The $HH \rightarrow b\bar{b}\tau\tau$ decay, therefore, has a good tradeoff between the signal

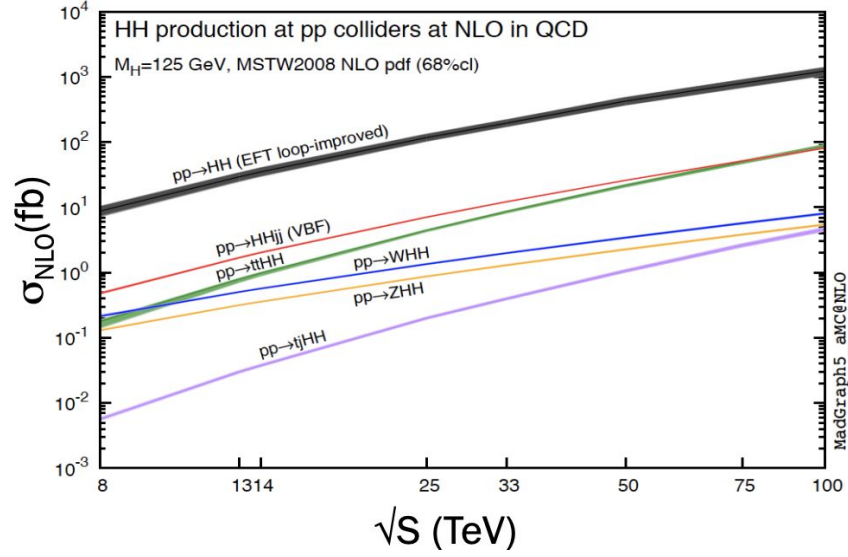


Figure 2.7: The HH production cross-section for different production modes as a function of the centre of mass energy (\sqrt{s}) of p-p collisions.

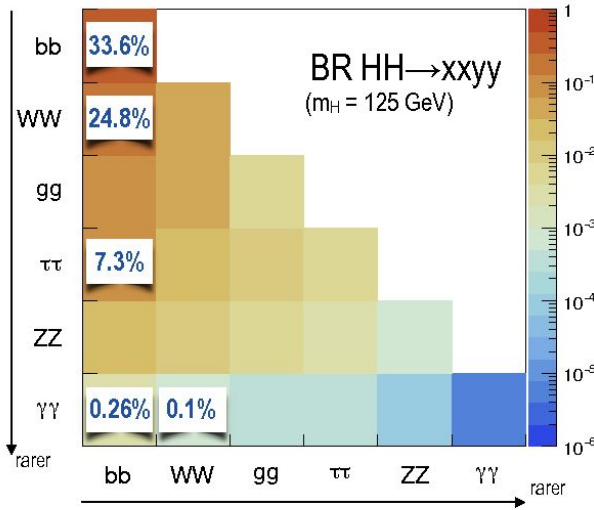


Figure 2.8: The branching fractions of various HH decay modes, weighted with respect to the branching fraction of $HH \rightarrow b\bar{b}b\bar{b}$.

yield and background contamination and is a final state of importance for the HH search.

2.10 Physics beyond the Standard Model

Despite the remarkable success of the Standard Model, there are several phenomena, like Higgs mass hierarchy problem, presence of Dark Matter and Dark Energy, presence of small neutrino mass etc., that can not be explained by the SM. Many theories, collectively know as theories beyond the Standard Model (BSM), have been developed to address the shortcomings of the SM.

2.11 HH production as a probe for BSM physics

Effect of BSM physics can be explored by studying HH production either via the anomalous couplings of the Higgs boson or via a BSM particle that can be produced either directly or in the quantum loop. In both the cases, there will be an increase in the HH production cross-section. For the resonant case, where a BSM particle directly decays to HH , the increase will be at a specific invariant mass value. For the non-resonant case, where the anomalous coupling of the Higgs boson comes into play, the increase will be over the full range of the invariant mass spectrum.

2.11.1 Non-resonant HH production

For non-resonant HH production, the effect of the BSM physics can be modelled by an effective Lagrangian, which is formed by extending the SM Lagrangian with

dimension-6 operators [20]. The effective Lagrangian modifies the Higgs-to-top coupling (y_t) and Higgs self-coupling (λ). The modification in the couplings is parametrised by: $\kappa_t = y_t/y_t^{SM}$ and $\kappa_\lambda = \lambda/\lambda^{SM}$. The effective Lagrangian also proposes new couplings like,

- c_2 : the coupling parameter associated with the interaction between a pair of Higgs bosons and a pair of top quarks. The corresponding Feynman diagram is shown in Figure 2.9a.
- c_g : the coupling parameter associated with the interaction between a gluon pair and a Higgs boson. The corresponding Feynman diagram is shown in Figure 2.9b.
- c_{2g} : the coupling parameter associated with the interaction between a gluon pair and a Higgs boson pair. The corresponding Feynman diagram is shown in Figure 2.9c.

Currently, only the HH production by y_t and λ couplings is being studied where the couplings can take BSM values.

2.11.2 Resonant HH production

A generic Feynman diagram for resonant HH production is shown in Figure 2.10, where a BSM particle X decays to two Higgs bosons. The resonant HH production is predicted by many extensions of the SM. Some examples are given below :

- Higgs Singlet Model [21–23]: In this model, an additional scalar singlet of the $SU(2)_L$ group is considered on top of the SM. The scalar singlet produces

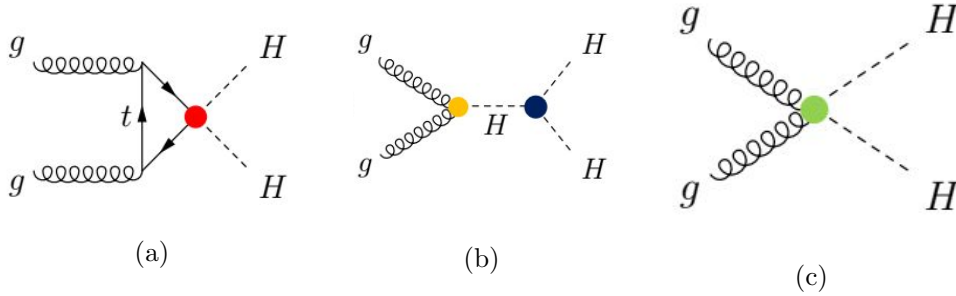


Figure 2.9: Feynman diagrams for interaction between (a) a pair of Higgs bosons and a pair of top quarks, (b) a gluon pair and a Higgs boson, and (c) a gluon pair and a Higgs boson pair.

another physical Higgs boson state after the spontaneous symmetry breaking. The new Higgs boson may be heavier than the SM Higgs boson and can decay to two SM Higgs boson.

- Two-Higgs Doublet Model (2HDM) [24] and minimal supersymmetric standard model (MSSM) [25; 26]: In both the models, an additional scalar doublet of the $SU(2)_L$ group is considered. After the spontaneous symmetry breaking, five Higgs states appear: two CP even neutral Higgs bosons h and H (where H is heavier than h by convention), the CP odd pseudoscalar A and two charged Higgs bosons H^\pm . The ratio of the two vevs of the two scalar doublets is represented by $\tan\beta = v_2/v_1$. In the alignment limit [53], the lighter CP even neutral Higgs boson h coincides with the SM Higgs boson and the heavy CP even neutral Higgs H can decay to two SM Higgs bosons. The MSSM, where the observed 125 GeV Higgs boson is considered as the CP even light Higgs boson h , is called the *h*MSSM [27; 28].

- Warped Extra Dimensions (WED) [29; 30]: The WED models predict extra dimensions, with an anti-de Sitter geometry, over the usual 4 dimensions of space-time. In the WED models, resonant HH production is mediated by either a spin-two massive Kaluza-Klein (KK) graviton or a spin-zero radion.

Although, physics motivation and phenomenology of the BSM models are very different, the resonant signal can be represented by a CP even scalar particle S decaying to two Higgs bosons, with an intrinsic width which can be neglected compared to the detector resolution (narrow-width approximation).

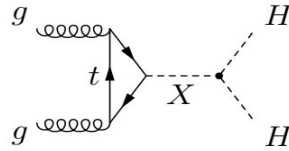


Figure 2.10: Feynman diagram for resonant HH production.

2.12 Decays of B_s^0 meson as a probe for BSM physics

The B_s^0 meson is composed of a b anti-quark and an s quark while its anti-particle \bar{B}_s^0 is composed of a b quark and an s anti-quark. B_s^0 (\bar{B}_s^0) can decay to any particular final state either directly or after $B_s^0 - \bar{B}_s^0$ oscillation takes place. The interference between these two decay amplitudes results in an asymmetry in the decay time and amplitude distributions of B_s^0 and \bar{B}_s^0 mesons. This asymmetry can be related to the CP-violating phase ϕ_s [54]. The phase ϕ_s is related to the elements of the CKM matrix by the relation $\phi_s \simeq 2\beta_s$, where $\beta_s = \arg[-(V_{ts}V_{tb}^*)/(V_{cs}V_{cb}^*)]$. The value of

ϕ_s depends on the decay amplitude and is precisely predicted in the SM to have different values in B_s^0 (\bar{B}_s^0) decays to different final states. Presence of BSM physics can significantly change the decay amplitudes from the SM predictions, where heavy new particles enter the quantum loop. Hence, an accurate experimental measurement of the decay amplitudes and ϕ_s in various decay modes of the B_s^0 (\bar{B}_s^0) meson is required to look for hints of new physics, which may lie beyond the direct reach of the LHC.

2.13 $B_s^0 \rightarrow \phi\phi \rightarrow 4$ Kaons

In CMS, the measurement of the CP-violating phase (ϕ_s) in B_s^0 decay has been performed with the $B_s^0 \rightarrow J/\psi\phi$ (with $\phi \rightarrow K^+K^-$) events [55]. A large branching fraction and clean experimental signature of the two muons coming from the J/ψ decay is the main reason for the choice of the final state. In the SM, the $B_s^0 \rightarrow J/\psi\phi$ decay predominantly proceeds through the $b \rightarrow c\bar{c}s$ penguin diagram.

The $B_s^0 \rightarrow \phi\phi$ (with $\phi \rightarrow K^+K^-$) decay is forbidden at the tree level in the SM and proceeds predominantly via a gluonic penguin $b \rightarrow s\bar{s}s$ loop process (cf. Fig. 2.11). $B_s^0 \rightarrow \phi\phi$ not only provides an independent measurement of ϕ_s , but also offers an excellent probe to search for new heavy particles that may enter the penguin quantum loops. In the SM, the value of ϕ_s in the $B_s^0 \rightarrow \phi\phi$ decay is small and QCD factorisation calculations show an upper limit of $\phi_s < 0.02$ [56–58]. The first evidence of the $B_s^0 \rightarrow \phi\phi$ decay was observed by the CDF experiment [59] at the Tevatron. The CDF and later LHCb experiments also searched for CP violation

in this decay channel [60–63]. The latest LHCb results for the branching fraction and CP violation phase, as measured in this process, are $\mathcal{B}(B_s^0 \rightarrow \phi\phi) = (1.84 \pm 0.05_{\text{stat}} \pm 0.07_{\text{syst}} \pm 0.11_{f_s/f_u} \pm 0.12_{\text{norm}}) \times 10^{-5}$ [64] and $\phi_s = -0.073 \pm 0.115_{\text{stat}} \pm 0.027_{\text{syst}}$, based on approximately 9000 B_s^0 candidates [65].

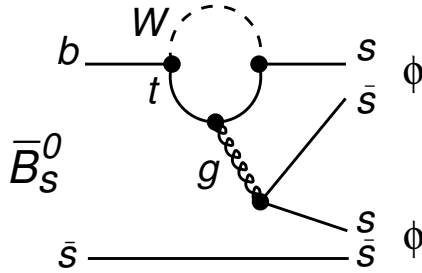


Figure 2.11: Feynman diagram for $B_s^0 \rightarrow \phi\phi$ decay.

Due to lack of a proper trigger, at present, it is next to impossible for CMS to trigger on low- p_T , fully hadronic final states, like $B_s^0 \rightarrow \phi\phi \rightarrow 4$ Kaons. However, during the High Luminosity LHC (HL-LHC) phase, tracking information will be included in the Level-1 trigger of CMS which will empower CMS to trigger on such final states for the first time. CMS Phase-2 Level1 tracking and the prospects of triggering $B_s^0 \rightarrow \phi\phi \rightarrow 4$ Kaons events during the HL-LHC, will be discussed in chapter 6 and chapter 8 respectively.

Chapter 3

The CMS experiment at the LHC

3.1 The LHC

The Large Hadron Collider (LHC) [66] is presently the highest energy particle accelerator in the world. The accelerator, placed in a tunnel between 50 and 175 meters below the surface in the Swiss-French border near Geneva, has a circumference of 27 km . Beams of protons or heavy ions are accelerated in opposite directions in the LHC tunnel and are made to collide in four interaction points. Although the operation of the LHC started in 2008, the first physics collision took place in 2010 at a centre of mass energy, $\sqrt{s} = 7\text{ TeV}$. In 2012, the energy was increased to $\sqrt{s} = 8\text{ TeV}$. The proton-proton collision energy at the LHC was further increased to $\sqrt{s} = 13\text{ TeV}$ during the long shutdown period 1 (LS1) during early 2013 to early 2015.

The proton beams go through several stages of acceleration through the CERN accelerator complex, as shown in Figure 3.1, before being injected into the LHC

tunnel. The acceleration steps are listed below,

- Protons are extracted from hydrogen atoms.
- The extracted protons are passed to a linear accelerator (LINAC2) [67], which accelerates them to an energy of 50 *MeV*.
- From the LINAC2 the protons are passed to the Proton Synchrotron Booster (PSB) [68], which accelerates them to 1.4 *GeV*.
- The Proton Synchrotron (PS) [69] is the next accelerator in the chain. The PS pushes the energy of the protons to 25 *GeV*. The PS also groups the protons in bunches of 25 *ns* (or 50 *ns*) according to the collision requirement.
- The proton bunches are then passed to the Super Proton Synchrotron (SPS) [70] where they are further accelerated to 450 *GeV*.
- Finally, the proton bunches are transferred to the LHC tunnel and accelerated to the collision energy.

The LHC is made out of eight straight sections and eight arcs. A simplified schematic diagram of the collider is shown in Figure 3.2. Counter-rotating proton or heavy-ion beams can be made to collide against each other at eight well defined points around the tunnel, four of which house the following four detectors,

- A Large Ion Collider Experiment (ALICE) [71] studies the physics of strongly interacting matter at very high energy densities, where formation of a novel phase of matter, called quark-gluon plasma, is expected

CERN's Accelerator Complex

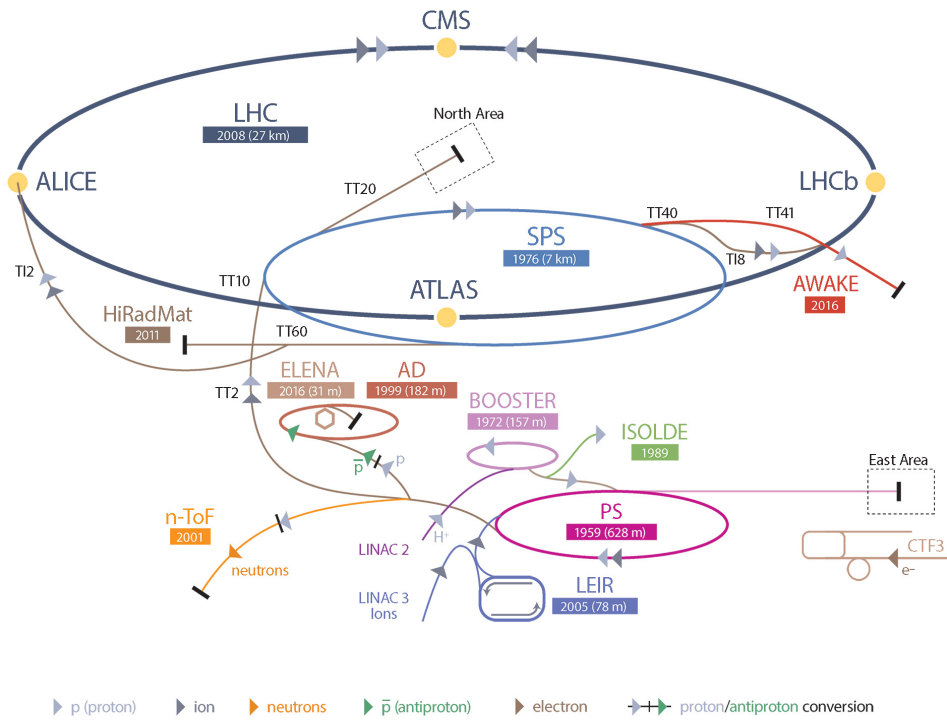


Figure 3.1: The layout of the CERN accelerator complex.

- A Toroidal LHC ApparatuS (ATLAS) [13] is a general purpose detector designed to study physics at the electroweak scale including Electroweak Symmetry Breaking and Higgs physics, as well as physics beyond the Standard Model, by exploiting the full physics potential of the LHC
- Compact Muon Solenoid (CMS) [14] is another general purpose detector with the same physics goals as that of ATLAS

- The Large Hadron Collider beauty (LHCb) [72] is a forward detector designed to investigate CP violation, matter-antimatter asymmetry etc. by studying B-hadrons

Superconducting electromagnets are used to maintain the orbital motion of the protons in the LHC. These magnets produce a maximum magnetic field of 8 Tesla, operating at a temperature below 2° K. Dipole magnets are used to bend the protons, whereas quadrupole magnets are used to focus the beams in the transverse direction. The diameter of a proton beam after focusing is about 16 μm .

Radio Frequency (RF) cavities are used to accelerate the protons up-to the final energy. The RF cavities produce a field gradient of 5.5 MeV/m which provides enough energy to accelerate the protons after compensating for the energy loss of the protons due to synchrotron radiation.

The instantaneous luminosity of an accelerator depends on several beam parameters. Considering a Gaussian beam profile, the formula to compute instantaneous luminosity is [73],

$$L = \frac{N_b^2 n_b f_{rev} \gamma_r}{4\pi \epsilon_n \beta^*} F \quad (3.1)$$

where,

- N_b indicates the number of bunches in each beam,
- n_b is the number of particles per bunch,
- f_{rev} is the revolution frequency,

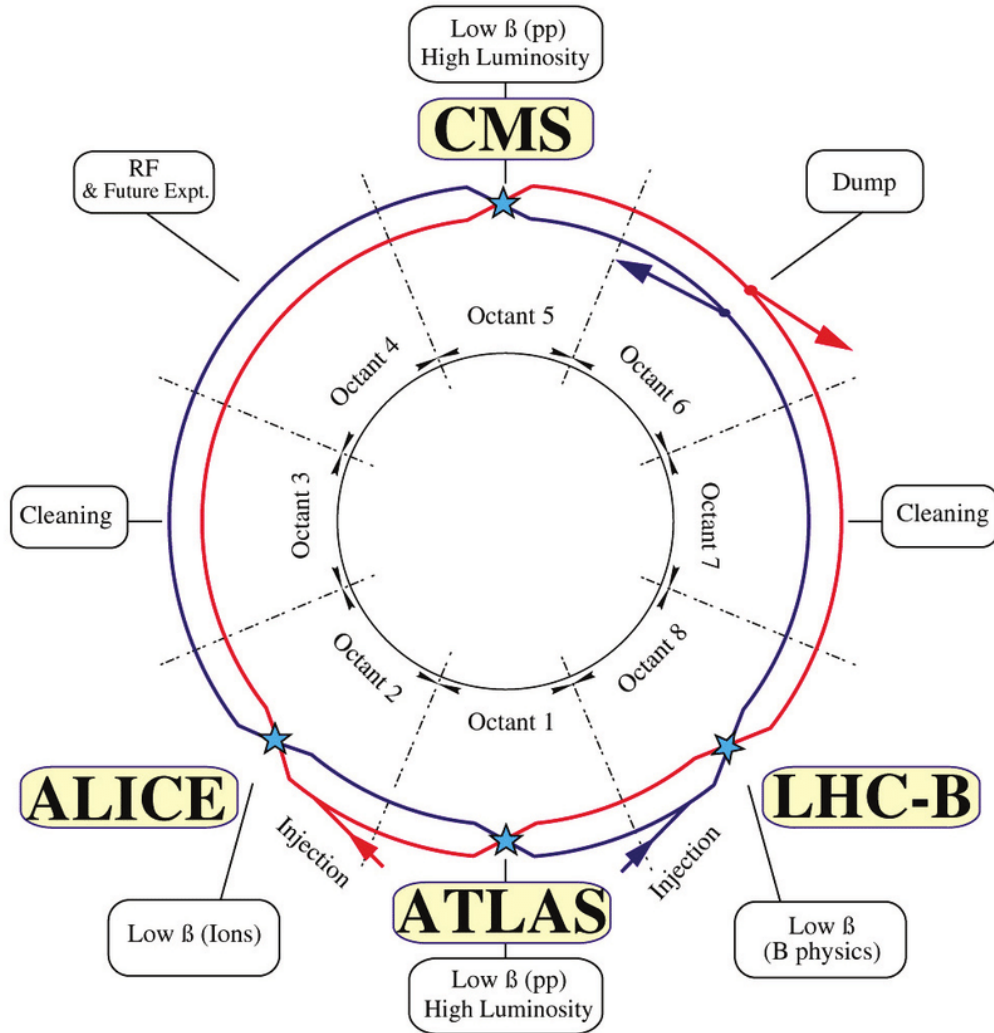


Figure 3.2: The schematic of the LHC.

- ϵ_n is normalised beam emittance,

- β^* is the machine beta function,
- γ_r is the Lorentz relativistic factor,
- F is the geometric reduction factor.

The geometric reduction factor or F is defined by,

$$F = \left[1 + \left(\frac{\theta_c \sigma_z}{2\sigma^*} \right)^2 \right]^{1/2} \quad (3.2)$$

where,

- θ_c is the beam crossing angle,
- σ_z and σ^* are the RMS size of the bunches along the longitudinal and transverse directions respectively.

The design value of the peak instantaneous luminosity of the LHC is $10^{34} \text{ cm}^{-2} \text{ s}^{-1}$ (equiv. to 10 Hz/nb). The delivered peak instantaneous luminosity for each running year is shown in Figure 3.3 where it can be seen that the LHC has crossed the designed luminosity from 2016 onward.

At the LHC, high instantaneous luminosity along-with large proton-proton cross section results in a large number of interactions per bunch crossing. Most of these interactions involve low momentum transfer and are of little physics interest. The interaction vertices in one bunch crossing, apart from the vertex of physics interest, are called pile-up (PU) vertices. As shown in Figure 3.4, the average value of pile-up is $\langle \text{PU} \rangle \sim 27$ for the 2016 data taking period. The high number of interactions

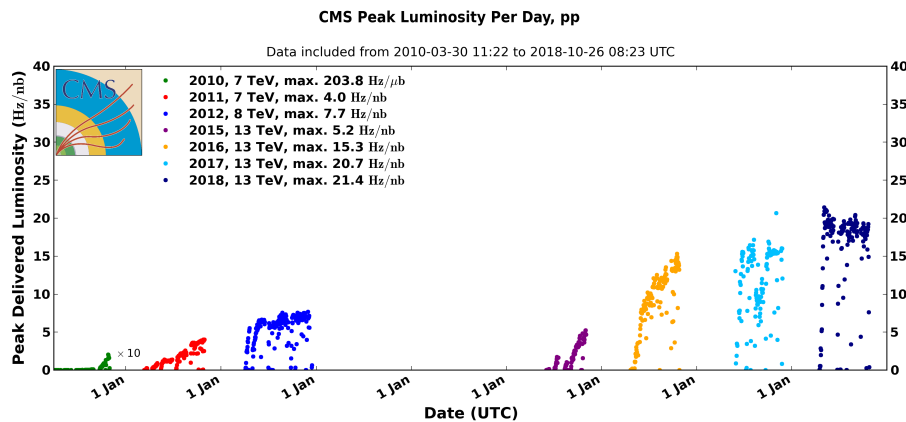


Figure 3.3: The peak instantaneous luminosity versus time as delivered by the LHC to the CMS experiment with stable beams in p-p collisions. The green, red, blue, purple, orange, sky blue and deep blue colours represent 2010, 2011, 2012, 2015, 2016, 2017 and 2018 data-taking periods respectively.

also results in high multiplicity of particles crossing the detectors (~ 1000 charged particles) per bunch crossing.

The total amount of data collected by an experiment over a data taking period is represented by integrated luminosity, $L_{int} = \int L dt$, where L is the instantaneous luminosity. Figure 3.5 shows the integrated luminosity for p-p collisions delivered by the LHC to CMS for each running year.

3.2 The CMS Detector

The Compact Muon Solenoid (CMS) is a general purpose detector located at the LHC collision point 5 of the LHC ring. Precise measurement of energy and momentum of electrons, photons and muons and reconstruction of the interaction vertices with

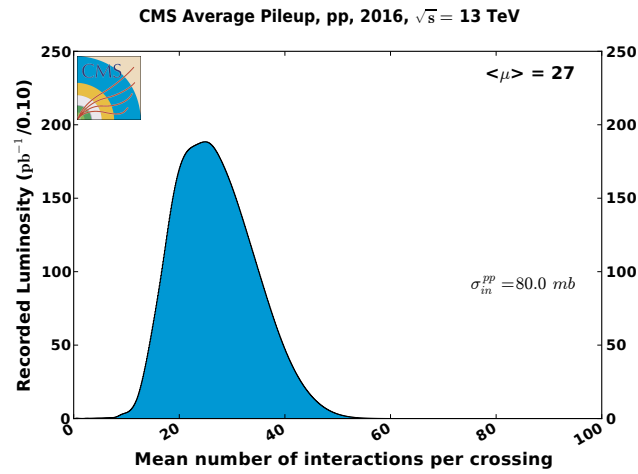


Figure 3.4: Average number of interactions per bunch crossing during 2016 data taking period.

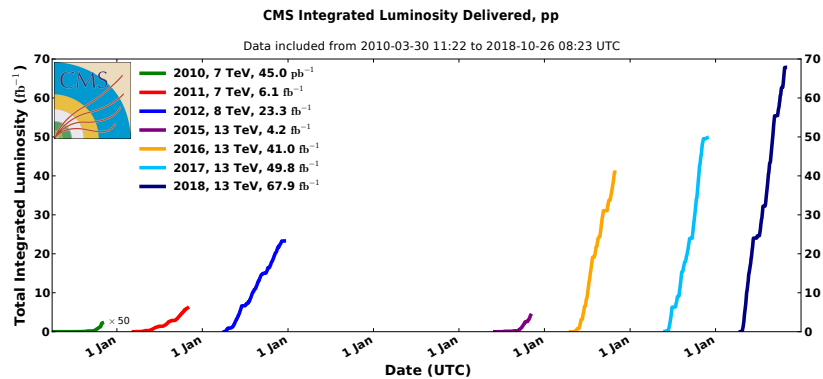


Figure 3.5: The integrated luminosity delivered to the CMS experiment by the LHC with stable beams in p-p collisions. The green, red, blue, purple, orange, sky blue and deep blue colours represent 2010, 2011, 2012, 2015, 2016, 2017 and 2018 data taking periods respectively.

high resolution are among the major characteristics of the detector. The detector has been specifically designed to work in high radiation levels of the LHC.

The CMS detector is composed of several sub-detectors covering a wide solid angle around the beam pipe. The detector has a cylindrical shape with an overall length of 28.7 m and a diameter of 15 m and weighs 14000 tonnes. The detector consists of one central barrel and two endcap regions. A layout of the CMS detector is shown in Figure 3.6.

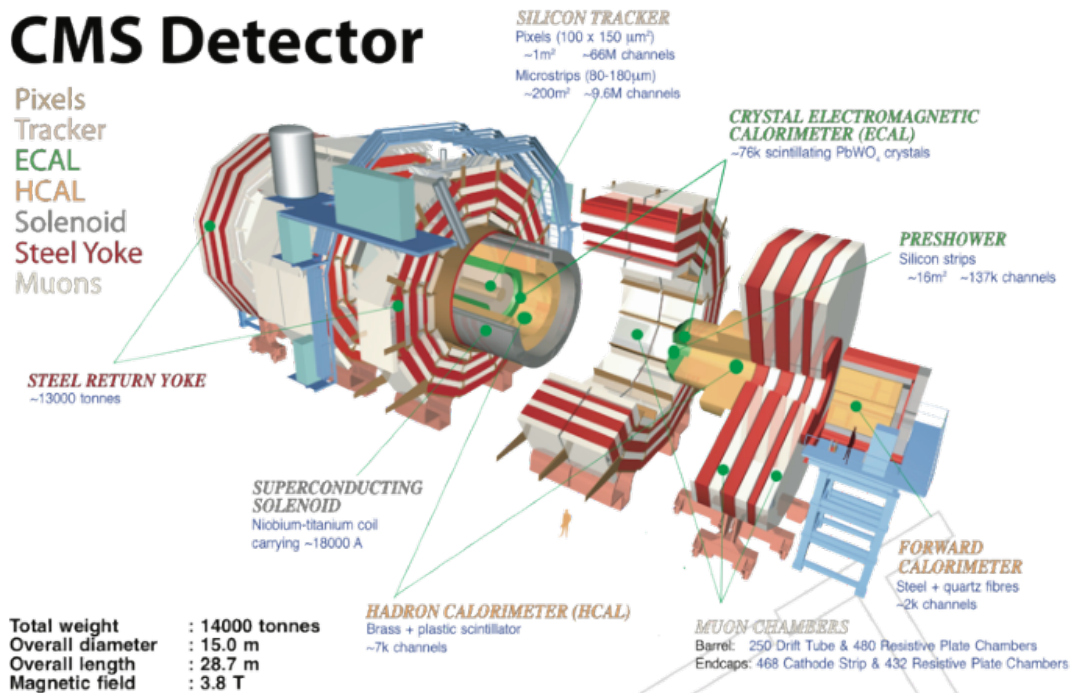


Figure 3.6: The layout of the CMS detector.

CMS uses a right-handed co-ordinate system. The origin of the co-ordinate system is at the nominal interaction point. The x -axis points towards the centre of the LHC, the y -axis points upwards (perpendicular to the LHC plane), and the z -axis is along the anti-clockwise beam direction. The polar angle, θ is measured from the

positive z -axis and the azimuthal angle ϕ is measured in the $x - y$ plane. The pseudorapidity, η , is defined as $\eta = -\log(\tan(\theta/2))$. The details of the CMS detector can be found in Reference [14]. An overview of the various sub-detectors of CMS is presented in the following sections.

The CMS beam pipe is 20 m long and made out of Beryllium (Be), which is a very light material and has a very low probability of nuclear interaction for particles emerging from p-p collisions.

The CMS detector has a superconducting solenoid [74], which produces a large magnetic field of 3.8 Tesla. The enclosure of the superconducting solenoid, which has an internal diameter of 6 m , acts as a support structure for sub-detectors. The silicon tracker, the crystal electromagnetic calorimeter and the sampling hadron calorimeter are placed inside the solenoid radially outwards from the beam pipe. The large magnetic field produced by the solenoid enables CMS to measure the momenta of the charged particles very precisely. The solenoid is made up of Aluminium conductor and the solenoid coils are split in five separate modules, each containing four layers of wound within a supporting cylinder. The magnetic flux is returned by a 1.8 m thick iron yoke, which consists of 6 endcap discs and 5 barrel wheels. The return yoke houses the muon detector subsystem. The magnetic field inside the return yoke is around 2 Tesla.

3.2.1 Tracker

The CMS tracking system [75; 76], which is placed closest to the beam pipe, has been designed to work efficiently in the high radiation environment of the LHC.

The CMS tracker is made up of several cylindrical layers of silicon pixel and strip detectors. Charged particles, produced in p-p collisions and passing through these detectors, register hits in the detector layers. The charged particles bend in the tracker volume due to the presence of the strong magnetic field. Trajectories of the charged particles, called tracks, are reconstructed by the tracker, by combining the hits in different layers. The momenta of the charged particles are measured from the radius of curvature of the trajectory. Reconstructed tracks are used to find the primary and secondary vertices in the event.

The layout of the CMS tracker is shown in Figure 3.7. The tracker provides a pseudorapidity coverage up-to $|\eta| < 2.5$. The total surface area of the CMS tracker is $200 m^2$. The amount of material that a particle has to traverse in the tracker is quantified by material budget. The probability of multiple scattering increases with increasing material budget which adversely affects the performance of the electromagnetic calorimeter which is placed immediately after the tracker. The tracker design was optimised to keep the material budget as low as possible. The material budget of the CMS tracker, in units of radiation length [77], is shown in Figure 3.8 as a function of η .

The inner region of the CMS tracker is known as the pixel detector and is made out of 66 million square silicon pixels. The size of each pixel is $100 \mu m$ in the $r - \phi$ direction and $150 \mu m$ in the z direction. The thickness of the sensors is $285 \mu m$. The barrel region of the pixel detector consists of three layers situated at radii $4.3 cm$, $7.2 cm$ and $11 cm$ respectively. There are endcap discs on each side of the barrel region at a distance of $34.5 cm$ and $46.5 cm$ from the interaction point. To read out

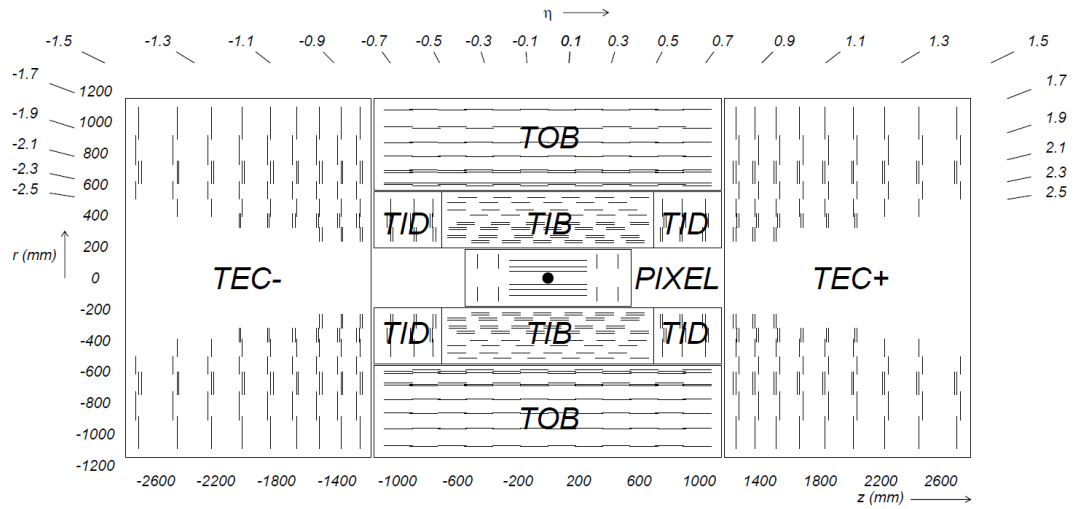


Figure 3.7: The layout of the CMS tracker.

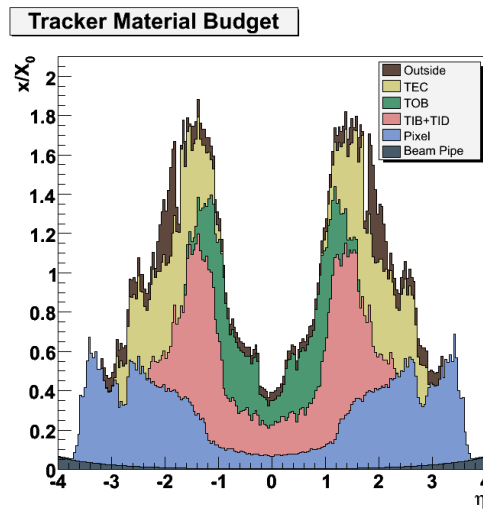


Figure 3.8: Material budget of the CMS tracker as a function of tracker η , in units of radiation length. The maximum around $|\eta| \sim 1.4$ is due to the presence of the service materials in that region.

the full pixel detector 15840 read-out chips (ROC) are used. The ROCs are bump-bonded to the pixel sensors. The pixel detector provides 3-dimensional measurement of a hit needed for vertex reconstruction in CMS. The hit efficiency of the pixel detector measured with 2016 data is shown in Figure 3.9a.

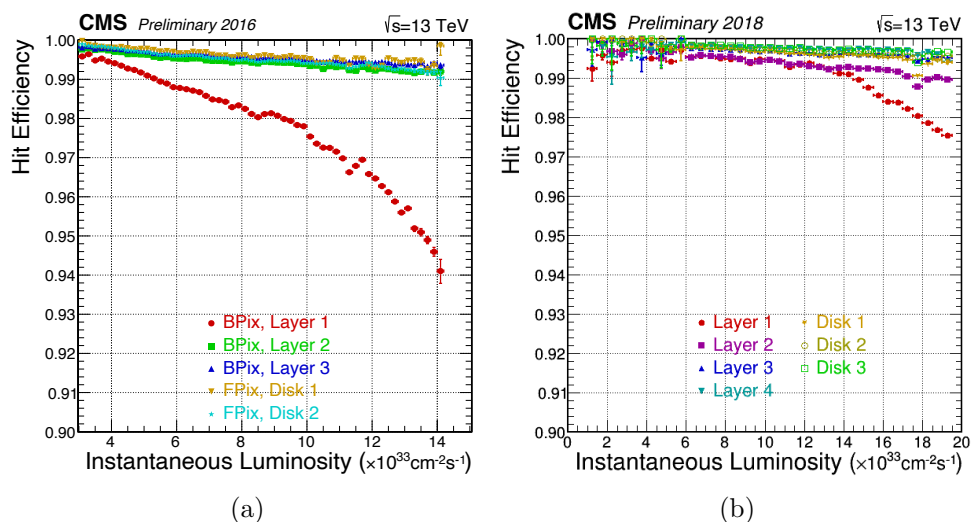


Figure 3.9: (a) The hit efficiency vs instantaneous luminosity for the CMS pixel detector measured with 2016 data. (b) The hit efficiency vs instantaneous luminosity for the CMS Phase-1 pixel detector measured with 2018 data.

It can be seen from the figure that the hit efficiency of the first barrel layer decreased significantly with increasing instantaneous luminosity in 2016. Keeping in mind that the instantaneous luminosity would increase further in subsequent years, the pixel detector was scheduled to be replaced by an improved one, known as the Phase-1 pixel detector, at the end of 2016. The Phase-1 pixel detector, with less material budget compared to the previous pixel detector, consists of four barrel layers at radii 2.9 cm, 6.8 cm, 10.9 cm and 16 cm respectively and three endcap

discs on either side of the barrel region extending up-to 50 *cm* from the interaction point. The Phase-1 pixel detector was also designed to improve vertex resolution and b-tagging performance of CMS. The hit efficiency vs instantaneous luminosity for the CMS Phase-1 pixel detector measured with the 2018 data is shown in Figure 3.9b.

The outer strip tracker surrounding the inner pixel detector is made up of 9.6 million silicon strips. The outer tracker is divided in four regions, as shown in Figure 3.7: four layers in the inner barrel (TIB), six layers in the outer barrel (TOB), three inner discs (TID) on either side of TIB and nine endcap discs (TEC) on each side. The barrel layers cover the radial distance from 25 *cm* to 110 *cm*. The endcap discs cover up-to 110 *cm* in radius and 280 *cm* in *z*. The thickness of the sensors is 320 μm for the TIB and TID. For TOB and TEC, the sensor thickness is 500 μm .

The pitch of the detector modules, defined as the distance between two adjacent strips, varies from 80 – 205 μm depending on the position of the modules. As particle flux decreases away from the interaction point, the pitch is higher at higher radii. The first two layers of TIB and TOB, TID rings 1 and 2 and TEC rings 1, 2 and 5 are equipped with stereo modules. The stereo modules are built with two silicon sensors which are mounted back-to-back with a relative angle of 100 mrad between the strips of the two sensors. The stereo modules provide 3-dimensional positions of the hits with the help of the two sensors.

An iterative tracking algorithm is used to reconstruct the tracks with the hits reconstructed in the tracker layers [1]. The tracking algorithm produces a set of tracks in each iteration and the hits corresponding to the reconstructed tracks are ignored in the successive iterations.

Good momentum resolution is among the primary requirements of a tracking detector. The track p_T resolution as a function of $|\eta|$ is shown in Figure 3.10 for single muon MC simulated events in the CMS tracker. For muons of p_T in the range $1 - 10 \text{ GeV}$, the p_T resolution is around $1 - 4\%$ over the entire η range. The track impact parameter resolutions as a function of η , both in the transverse plane and the longitudinal direction, are shown in Figure 3.11. As can be seen from the figure, the transverse and longitudinal impact parameter resolutions are $\approx 10 - 20 \mu\text{m}$ and $\approx 30 - 100 \mu\text{m}$ respectively, for muons of $p_T = 100 \text{ GeV}$. The tracking and vertex reconstruction performance of the CMS tracker is presented in Ref [1]. The tracking efficiency for muons with $p_T > 10 \text{ GeV}$ with respect to muon η and number of primary vertices reconstructed in an event using 2016 data are shown in Figure 3.12. The tracking efficiency has a high value of $\approx 99\%$ over the whole detector region which decreases as the number of primary vertices increases, and falls to $94 - 95\%$ for number of primary vertices > 40 . The above results confirm the power of the CMS tracker.

3.2.2 Electromagnetic Calorimeter

The CMS Electromagnetic Calorimeter (ECAL) [78] measures energy of electrons and photons precisely from the shower formed by those particles. The ECAL is a homogeneous calorimeter made of PbWO_4 crystals and covers up-to $|\eta| < 3$. The PbWO_4 crystals have high density (8.28 g/cm^3), small radiation length (0.89 cm) and Molière radius (2.2 cm) which allow CMS to have a compact ECAL. The PbWO_4 crystals have fast response time, i.e. almost 80% of scintillation light is emitted within 25 ns .

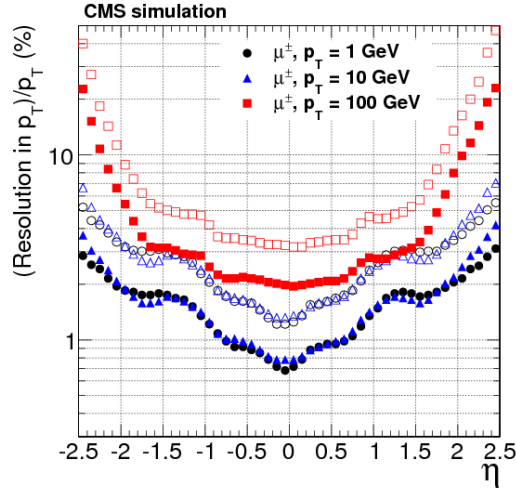


Figure 3.10: The p_T resolution of the simulated muon tracks as measured by the CMS tracker as a function of η , for muons of $p_T = 1$ (black), 10 (blue) and 100 GeV (red) [1]. The solid symbols represent the half-width containing 68% of the residual distribution around the mean value and stand for actual resolution. The open symbols represent the resolution if the 90% of the residual distribution around the mean value is considered and show the effect of the extreme values.

The ECAL is, therefore, able to operate in the high pile-up environment of the LHC. The crystals have low light output that depends on the operating temperature.

The layout of the ECAL, which consists of the central barrel (EB) and the end-caps (EE), is shown in Figure 3.13. The EB covers up-to $|\eta| < 1.479$, while the EE covers the region $1.479 < |\eta| < 3.0$. Avalanche photo diodes (APD) and vacuum photo triodes (VPT) are used to read out the scintillation light from the crystals in EB and EE respectively. The EB has an internal radius of 1.29 m . The EB is composed of 61200 crystals and is mechanically divided into thirty-six **supermodules**. Each **supermodule** covers 10° in both positive or negative θ directions. In order

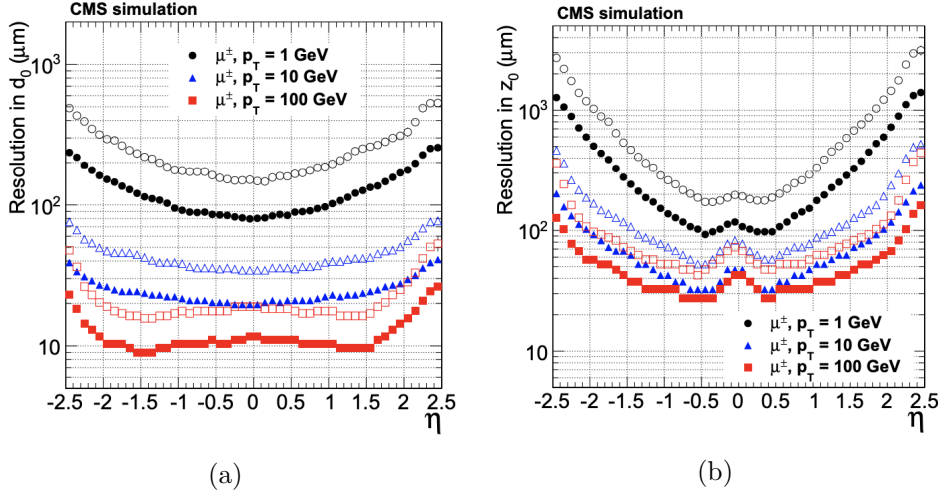


Figure 3.11: (a) Transverse and (b) longitudinal impact parameter resolution of the simulated muon tracks as a function of η for muons of $p_T = 1$ (black), 10 (blue) and 100 GeV (red) [1]. The solid symbols represent the half-width containing 68% of the residual distribution around the mean value and stand for actual resolution. The open symbols represent the resolution if the 90% of the residual distribution around the mean value is considered and show the effect of the extreme values.

to improve the hermiticity, the crystals are mounted in a quasi-projective geometry with their axis tilted by 3° with respect to the nominal interaction point. The crystals have a frontal surface area of $2.2 \times 2.2 \text{ cm}^2$ and a length of 23 cm . The EE sections are placed at a distance of 3.17 m from the nominal interaction point, on both sides of the EB. The EE is divided in four **Dees**. Each dee covers 180° in the ϕ direction. There are 14648 tapered crystals in the EE which are arranged in a rectangular $x - y$ grid and grouped in squared 5×5 mechanical structure called **super-crystals**. The crystal dimensions are $2.86 \times 2.86 \times 22.0 \text{ cm}^3$.

To distinguish between the showers generated by a photon and a neutral pion,

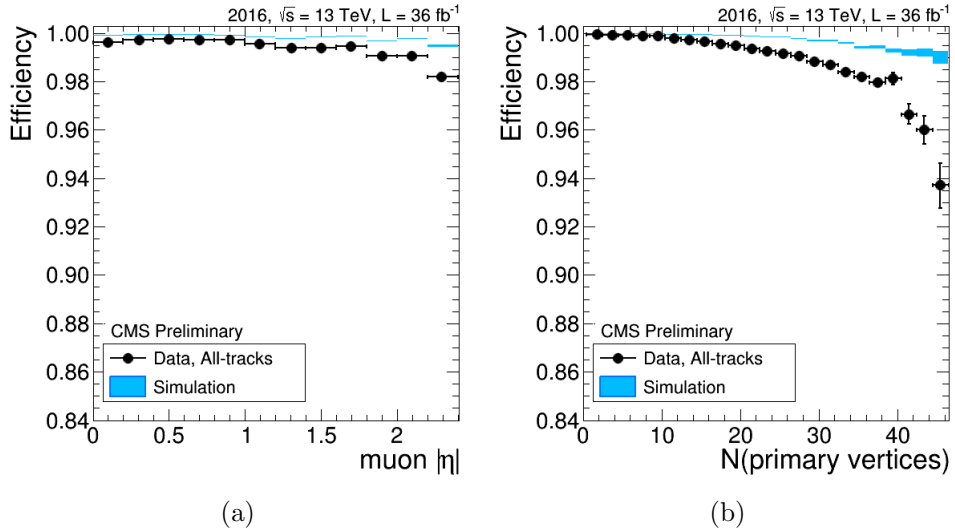


Figure 3.12: (a) Tracking efficiency for muons coming from Z decay as a function of muon $|\eta|$. (b) Tracking efficiency for muons coming from Z decay vs number of primary vertices reconstructed in an event. The black dots and light blue rectangles represent 2016 data and simulation respectively.

an ECAL preshower (ES) detector is placed in front of the EE. The ES is a sampling calorimeter with two planes of lead followed by silicon sensors, and covers the region, $1.653 < |\eta| < 2.61$. The lead in the ES acts as a radiator and the silicon strip detector measures the energy deposit and provides the transverse shower profile.

The resolution of the ECAL is,

$$\left(\frac{\sigma}{E}\right)^2 = \left(\frac{S}{\sqrt{E}}\right)^2 + \left(\frac{N}{E}\right)^2 + C^2 \quad (3.3)$$

where S , N and C represents the intrinsic stochastic term, the noise term and the constant term respectively. The fluctuations related to the shower development in the crystal are represented through the stochastic term. For CMS, the energy region

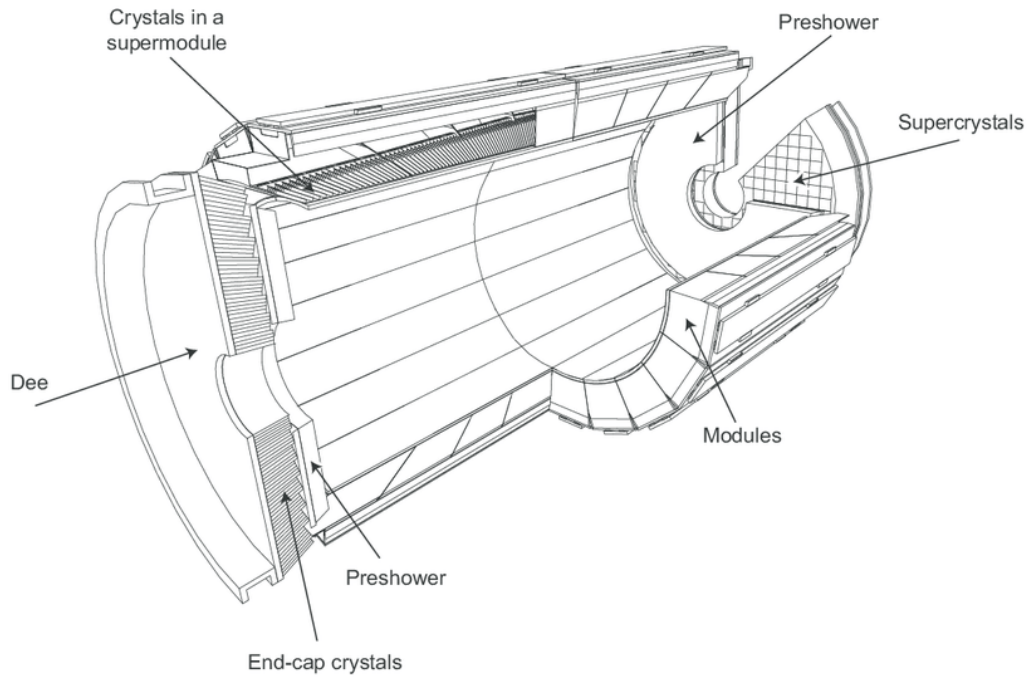


Figure 3.13: The layout of the CMS electromagnetic calorimeter.

of physics interest is around 100 GeV where the constant term is the dominant one. The constant term is derived in dedicated beam tests with electron beams of various energies. The energy resolution of the ECAL obtained in the beam tests is shown in Figure 3.14, where one can see that the energy resolution better than 1% for energies $> 20 \text{ GeV}$ can be achieved.

3.2.3 Hadron Calorimeter

The CMS Hadron Calorimeter (HCAL) [79] is a sampling calorimeter with brass and plastic as the absorber and scintillating materials respectively. Plastic scintillator

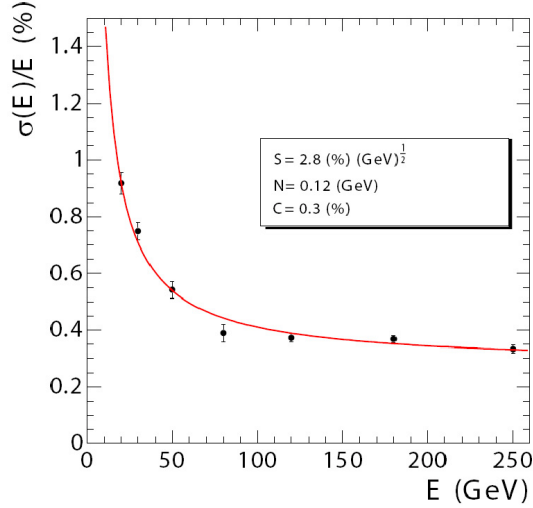


Figure 3.14: The energy resolution of the electromagnetic calorimeter as measured in beam tests.

is chosen due to its long-term stability and radiation hardness and brass because of its non-magnetic nature and structural stability. Charged and neutral hadrons deposit their energy in the HCAL through nuclear interactions. The radial range of the HCAL is from $R = 1.77\text{ m}$ (the outer radius of ECAL) to $R = 2.95\text{ m}$ (the inner radius of the superconducting solenoid). The layout of the HCAL is shown in Figure 3.15 where the sub-components of the HCAL - hadron barrel (HB), hadron endcap (HE), hadron forward (HF) and hadron outer (HO) are shown. The outer hadron calorimeter (HO) is placed outside the superconducting solenoid.

The hadron barrel (HB), with a pseudorapidity coverage of $|\eta| < 1.3$, is segmented into 32×72 towers. Each tower has a size of $\Delta\eta \times \Delta\phi = 0.087 \times 0.087$. For the first and last layers, stainless steel is used as the absorber material due to its structural strength. For all other layers, brass (70% Cu and 30% Zn) plates of



Figure 3.15: A longitudinal view of one quarter of the CMS detector in the $r-\eta$ plane. The layout shown is up-to the HCAL indicating the components of the HCAL: hadron barrel (HB), hadron outer (HO), hadron endcap (HE) and hadron forward (HF)

thickness 155 mm are used as absorber. Plastic scintillators are used as the active material and there are 17 scintillating layers in the HB. The HB is also divided in two half barrels each of which holds 18 identical azimuthal sections.

The hadron endcap (HE) covers the region $1.3 < |\eta| < 3.0$. Similar to the HB, Brass plates are used as absorber in HE. The thickness of the brass plates is 79 mm . The HE is segmented into 14 towers along the η direction and 72 or 36 towers along the ϕ direction depending on the value of η . For $|\eta| < 1.6$, the size of the towers is $\Delta\eta \times \Delta\phi = 0.087 \times 0.087$ and for $|\eta| > 1.6$, it is $\Delta\eta \times \Delta\phi = 0.17 \times 0.17$. In the

HE, there are 18 layers of plastic scintillator. Both in the HB and HE, wavelength shifting fibres are used to carry the light output of the scintillators which are then detected by hybrid photo diodes (HPDs).

The hadron forward (HF) calorimeter covers the region $3.0 < |\eta| < 5.0$. The HF is located at a distance of 11.2 *m* from the nominal interaction point of CMS and the absorber depth is 1.65 *m* at such distance. In the HF, quartz fibres are used as the active medium and steel is used as the absorber material. The signal is generated as Cherenkov light in the quartz fibres.

The HO is placed between the magnetic coil and muon system to have adequate sampling depth in the central barrel region. The HO consists of 5 rings and the central ring has 2 scintillator layers on either side of an iron plate. The other rings have only one scintillator layer. The HO acts as a tail catcher to complement the hadron barrel. The solenoid is used as an additional absorber layer by the HO.

3.2.4 Muon System

The Muon system [2; 80] is the outermost sub-detector of CMS and is placed within the return yoke of the CMS magnet. The yoke provides a high magnetic field (~ 2 T) and serves as the absorber for the hadrons. The Muon system is divided into a central barrel and two endcap sections. The basic building blocks of the Muon system are gaseous detectors. Three types of gaseous detectors, namely, drift tubes (DT), cathode strip chambers (CSC) and resistive plate chambers (RPC) are used in the Muon system. A longitudinal view of one quarter of the Muon system is shown in Figure 3.16.

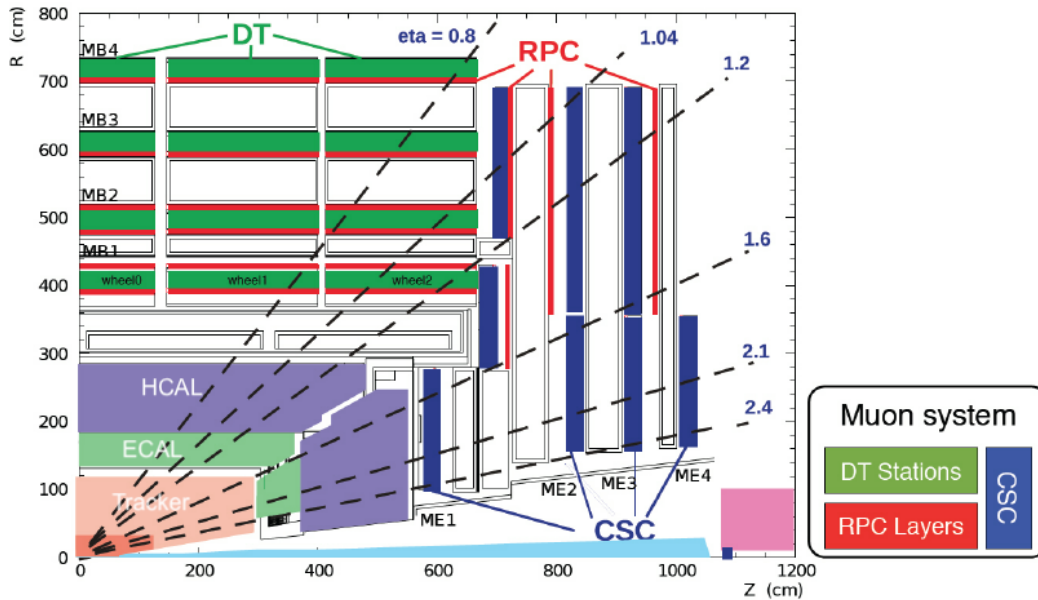


Figure 3.16: Layout of one quarter of the CMS detector. The components of the muon system: four DT chamber (MB1-MB4) in the barrel region, four CSC stations in the endcap (ME1-ME4) and RPC stations are shown in green, blue and red colours respectively.

The central barrel detector consists of drift tubes (DT) covering up-to $|\eta| < 1.2$. The expected muon flux and intensity of the local magnetic field is low in this region. The barrel region is made of four stations (MB1, MB2, MB3 and MB4) of DT chambers which are placed within the barrel return yoke and the four stations form coaxial cylinders around the beam axis. Each station consists of superlayers (SL) which are made up of four DT layers. In the first three stations (MB1, MB2 and MB3), there are 3 SLs, 2 of which measure the $r - \phi$ co-ordinate and the third one measures the $r - z$ co-ordinate. There are two SLs which measure the $r - \phi$ co-ordinate in the last

station (MB4). The first three stations have 60 DT chambers and the fourth station has 70 DT chambers.

The endcap is made of cathode strip chambers (CSC) covering the region $0.9 < |\eta| < 2.4$. CSCs are chosen for the endcap because they can operate efficiently under high magnetic field and high particle rate. CSCs also have a very fast time response. Each endcap is made up of four finely segmented stations in order to provide a good spatial resolution.

Resistive plate chambers (RPC), which have very fast time response, are installed both in barrel and endcap covering the region $|\eta| < 2.1$. The RPCs are designed to provide timing information of muon tracks to the muon trigger system. In the barrel, two RPCs are installed per DT, while in the endcap, one RPC is installed per CSC.

3.3 The CMS Trigger and DAQ System

The total proton-proton inelastic cross-section is ~ 80 mb at 13 TeV while the cross-section for some of the interesting physics, like the Higgs physics is smaller by nearly twelve orders of magnitude. As most of the interactions are of very little physics interest, they can be safely discarded without losing any physics potential. CMS uses a two-level trigger system to select events where at least one collision of interest occurs,

- Level1 (L1) trigger - hardware based trigger designed to bring down the data rate from 40 MHz to 100 kHz
- High Level Trigger (HLT) - software based trigger designed to bring down the

data rate from 100 kHz to 200 Hz

The schematic of the CMS trigger and DAQ system is shown in Figure 3.17. In order to select potentially interesting events, the trigger system looks for presence of at least one high p_T physics object (electron, photon, muon, tau, jet etc.) in the event.

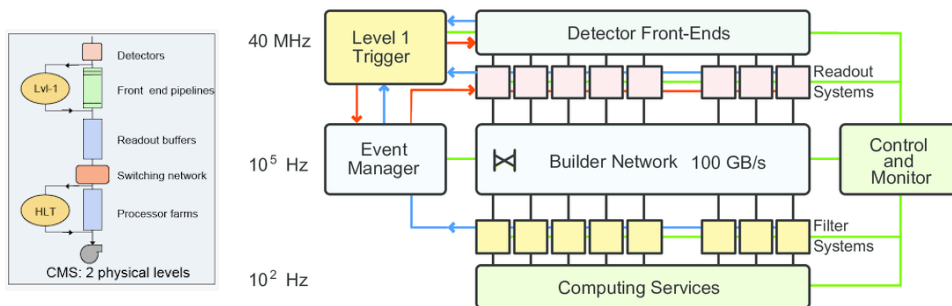


Figure 3.17: The schematic representation of the CMS trigger/DAQ system.

The event selection logic at L1 is implemented on hardware, namely field-programmable gate arrays (FPGA), application-specific integrated circuits (ASIC) and programmable memory lookup tables (LUT) etc. The L1 trigger consists of a calorimeter trigger, a muon trigger, and a Global Trigger (GT) sub-systems. The calorimeter trigger reads the energy deposits in ECAL and HCAL with coarse granularity and forms e/γ candidates, jets, taus, H_T , Missing Transverse Energy etc. in the event and passes it to the GT. Similarly, the muon trigger forms the muon candidates from the hits in the muon chambers and passes to the GT. The GT combines the information of the physics objects sent by the calorimeter and muon triggers to take a decision about acceptance (L1 accept) or rejection of an event. The maximum allowed time taken by the L1 trigger system to process an event is $3.2 \mu s$. The schematic representation

of the CMS L1 trigger system is shown in Figure 3.18.

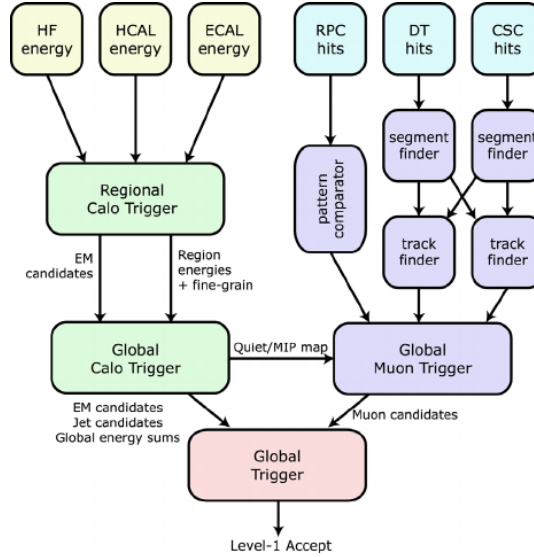


Figure 3.18: A schematic representation of the CMS L1 trigger system.

When an event is accepted by the L1 trigger system, data with full granularity from all the sub-detectors, and the objects formed at L1, are read out by the DAQ and passed to the HLT for further processing. The HLT algorithm is software based and the reconstruction of the physics objects are seeded by the L1 objects. Objects are reconstructed with high precision using algorithms similar to the ones used in the offline reconstruction. A sequence of reconstruction and selection algorithms with increasing complexity are performed at the HLT. The raw data of the events, which are selected by the HLT, are stored permanently for further processing.

The trigger selection algorithms are commonly referred as trigger paths. For example, the trigger requirement to select an isolated muon of $p_T > 24 \text{ GeV}$, in an event is defined as `HLT_IsoMu24` or `HLT_IsoTkMu24`, depending on the muon

reconstruction algorithm (discussed in chapter 4). The efficiency of the trigger path `HLT_IsoMu24` or `HLT_IsoTkMu24` estimated using 2016 data, is shown in Figure 3.19, with respect to p_T and η of the muon object. From Figure 3.19a, it can be seen that the muon trigger efficiency is high ($> 90\%$) after turn-on. The muon trigger paths, used in the analysis of the $HH \rightarrow b\bar{b}\tau\tau$ final state, are shown in Table 3.1. The muon triggers of Table 3.1 use a slightly lower p_T threshold (22 GeV) at the HLT where the region of physics interest lies well above the p_T threshold used. From Figure 3.19b, it can also be seen that the muon trigger efficiency is uniform over η within the detector acceptance.

HLT path names	Trigger requirement
<code>HLT_IsoMu22_eta2p1_v*</code> <code>HLT_IsoTkMu22_eta2p1_v*</code>	Muon, with $p_T > 22\text{ GeV}$ and $ \eta < 2.1$
<code>HLT_IsoMu22_v*</code> <code>HLT_IsoTkMu22_v*</code>	Muon, with $p_T > 22\text{ GeV}$

Table 3.1: Single muon trigger paths used in the $HH \rightarrow b\bar{b}\tau\tau$ analysis.

The trigger efficiency, measured using 2016 data, for several electron trigger paths, as a function of electron p_T in the ECAL barrel region is shown in Figure 3.20a and as a function of electron η in Figure 3.20b [81]. The trigger path `HLT_Ele25_eta2p1_WPTight` is used in the $HH \rightarrow b\bar{b}\tau\tau$ analysis and requires the presence of an electron, which has $p_T > 25\text{ GeV}$ and $|\eta| < 2.1$ and which passes the tight electron selection requirement (discussed in Chapter 4). The `HLT_Ele25_eta2p1_WPTight` trigger path is efficient in the region of physics interest and is uniform over the relevant η region of the detector.

The tau trigger paths, used in the $HH \rightarrow b\bar{b}\tau\tau$ analysis, are

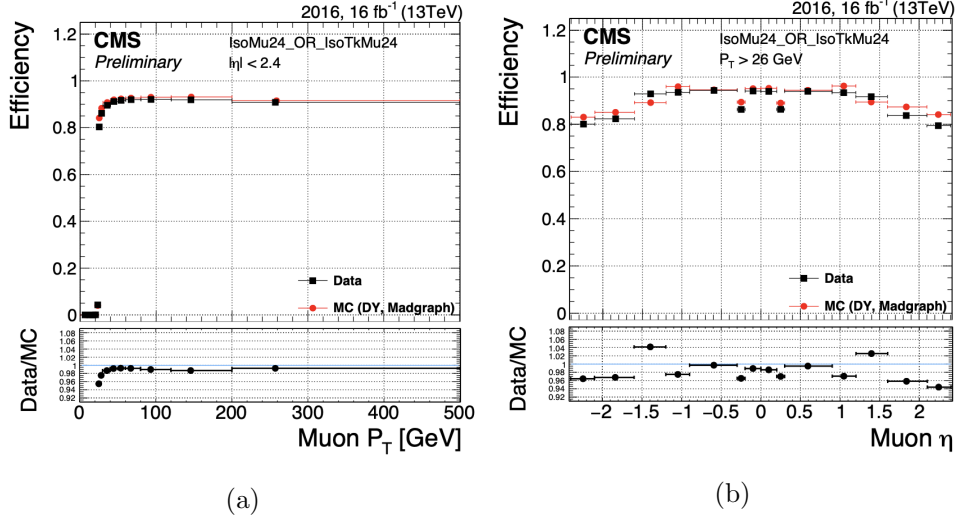


Figure 3.19: Muon trigger efficiency of one of the muon trigger paths used in CMS as a function of (a) muon p_T and (b) muon η , as measured with 2016 data.

- `HLT_DoubleMediumIsoPFTau35_Trk1_eta2p1_Reg`
- `HLT_DoubleMediumCombinedIsoPFTau35_Trk1_eta2p1_Reg`

and require presence of two isolated taus, with $p_T > 35 \text{ GeV}$ and $|\eta| < 2.1$, in the event. The efficiency of the trigger path

`HLT_DoubleMediumIsoPFTau35_Trk1_eta2p1_Reg`, for the 2016 data, as a function of tau p_T is shown in Figure 3.21.

3.4 CMS Data and Monte Carlo Events

In Figure 3.22, the amount of data delivered by the LHC to the CMS experiment and the amount of data recorded by the CMS Data Acquisition (DAQ) system are shown

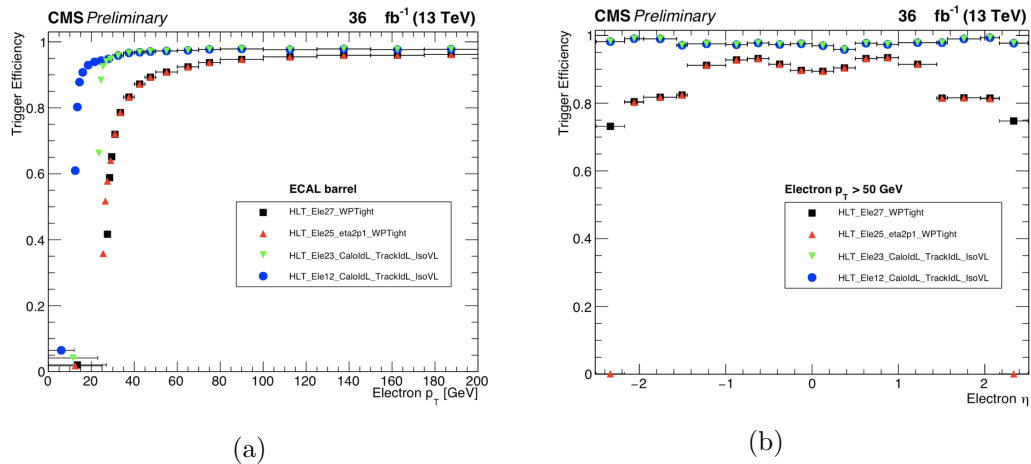


Figure 3.20: Electron trigger efficiency, measured with 2016 data, for several electron trigger paths used in CMS as a function of (a) electron p_T and (b) electron η . The `HLT_Ele25_eta2p1_WPTight` is used in this analysis which requires the presence of an electron of $p_T > 24$ GeV and $|\eta| \leq 2.1$.

for the 2016 data taking period and the data-taking efficiency of CMS is around 92%. The raw data from the detector are grouped in non-exclusive primary datasets according to the results of the HLT selection. The raw data go through the reconstruction step, which will be discussed in the chapter 4, and the reconstructed data are stored for physics analysis. Information of detector calibration, namely alignment, channel inefficiency, gain of electronics etc. are included in the reconstruction step.

A huge amount of Monte Carlo (MC) simulated events are produced for detector studies and physics analysis. In CMS, production of MC events goes through the following steps,

- LHE - the hard collisions are simulated with the help of specialised event gener-

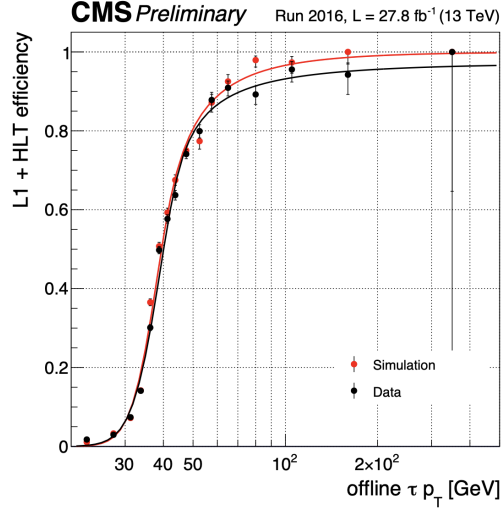


Figure 3.21: Tau trigger efficiency measured with 2016 data, as a function of tau p_T , for the tau trigger path used in the $HH \rightarrow b\bar{b}\tau\tau$ analysis.

ator software (e.g. MADGRAPH5_aMC@NLO [82]) and the final state particle information of the events are written in the LHE format [83].

- Generation (GEN) - final state particles of the hard collision undergo parton showering, hadronization and decay using Pythia [84] primarily.
- Simulation (SIM) - generated particles are passed through the CMS detector simulated by Geant4 [85] (both detector geometry and response). The simulation step results in a collection of time-stamped energy deposits in each detector cell.
- Digitisation (DIGI) - energy deposits obtained in the simulation step are digitised by an emulation of the CMS front-end electronics. The DIGI step results

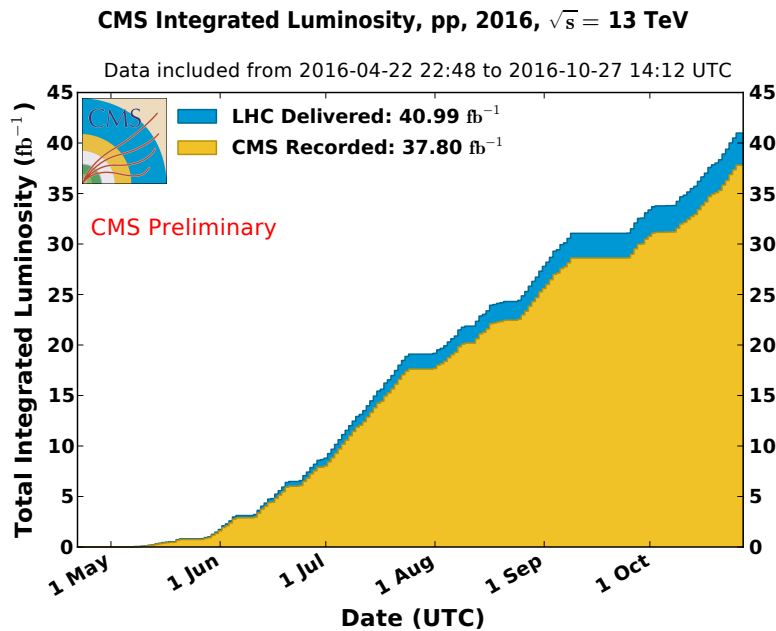


Figure 3.22: The delivered (blue filled region) and recorded (yellow filled region) integrated luminosity to the CMS experiment by the LHC, in p-p collisions during the 2016 data taking period.

in an event format, similar to the raw detector data acquired by the experiment.

- Pile-up (PU) mixing - a number of digitised soft collisions (PU events) are mixed with a digitised hard collision event to emulate the pile-up behaviour of real data.
- Reconstruction (RECO) - digitised simulated events, after PU mixing, are passed through the trigger system and then the reconstruction step.

3.4.1 CMS data tiers

The reconstructed data and MC events contain physics objects of various levels of complexities. To optimise storage of data and MC events several data-tiers with decreasing event size are in use in CMS,

- RECO - contains all the reconstructed objects. The average size of a reconstructed CMS event is $\sim 4 MB$.
- AOD - formed by dropping a large fraction of low level reconstructed objects from the RECO data tier. The AOD data tier has a size of $\sim 500 kB/event$. The AOD data tier was extensively used in CMS Run-1 physics analyses.
- MiniAOD - AOD tier event size turned out to be too large to be used in the CMS Run-2 analyses. For this reason, the MiniAOD data tier was formed by replacing low level reconstructed physics objects with high level ones, increasing the p_T threshold and reducing precision of physics objects from the AOD data tier. The size of the MiniAOD data tier is $\sim 50 kB/event$.
- NanoAOD - formed by dropping most of the tracks from the MiniAOD data tier. The NanoAOD data tier is saved as a flat ROOT [86] Tree structure. The event size in NanoAOD is $1 kB$.

Chapter 4

Physics Object Reconstruction in CMS

The event reconstruction process in CMS, which consists of reconstruction of beam spot, primary vertices and various physics objects, namely, electrons, photons, muons, jets, b-jets, τ leptons and missing transverse energy, and identification of the reconstructed physics objects, is discussed in this chapter.

4.1 Beam spot reconstruction

The beam spot is a 3-D profile of the luminous region inside the CMS detector where the p-p collisions take place. Reconstructed beam spot parameters are the position of the centre and size of the luminous region. The beam spot parameters are usually determined by taking an average over events collected in a period of 23 seconds, which is known as a *Lumi Section*. The details of the beam spot reconstruction in

CMS can be found in reference [1].

4.2 Primary vertex reconstruction

The primary vertices represent the points in space where the proton-proton interactions take place. Reconstruction of primary vertices in an event proceeds in two steps,

- *Vertex finding*, which groups tracks reconstructed in the event according to their z-coordinate at the point of closest approach to the centre of the beam spot. The vertex finding step is performed by a deterministic annealing (DA) algorithm [87].
- *Vertex fitting*, which determines the vertex position assuming that it is formed by the assigned tracks. The vertex fitting step is performed by an adaptive vertex fitter [88].

The primary vertex, with the highest value of $\sum p_T^2$ of the associated tracks, is considered as the event vertex.

The details of the reconstruction of the primary vertices can be found in reference [1]. The vertex resolution in the x and z directions, as a function of the number of tracks associated to the vertex, is shown in Figure 4.1.

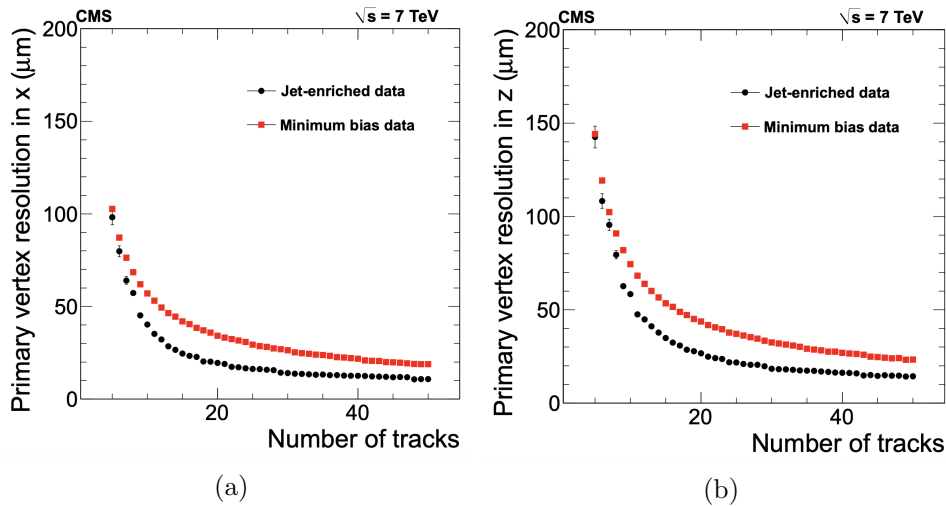


Figure 4.1: Vertex resolution in (a) x direction and (b) z direction, as a function of the number of tracks associated to the vertices [1], using minimum bias and jet enriched events.

4.3 Particle Flow algorithm

To reconstruct and identify final state particles like electrons, photons, muons and hadrons in an event, the Particle Flow (PF) Algorithm [89] is used in CMS which correlates information from different sub-detectors, exploiting the excellent spatial resolution of the detector. Higher level physics objects like jets, hadronic decay of τ leptons, and missing transverse energy (MET) are reconstructed from the basic physics objects reconstructed by the PF algorithm.

A transverse slice of the CMS detector and interaction of the particles, produced in a p-p collision, in the detector is depicted in Figure 4.2, where one can see that,

- All the charged particles bend in the magnetic field and leave traces in the tracking system, from which momentum and charge of the particles can be

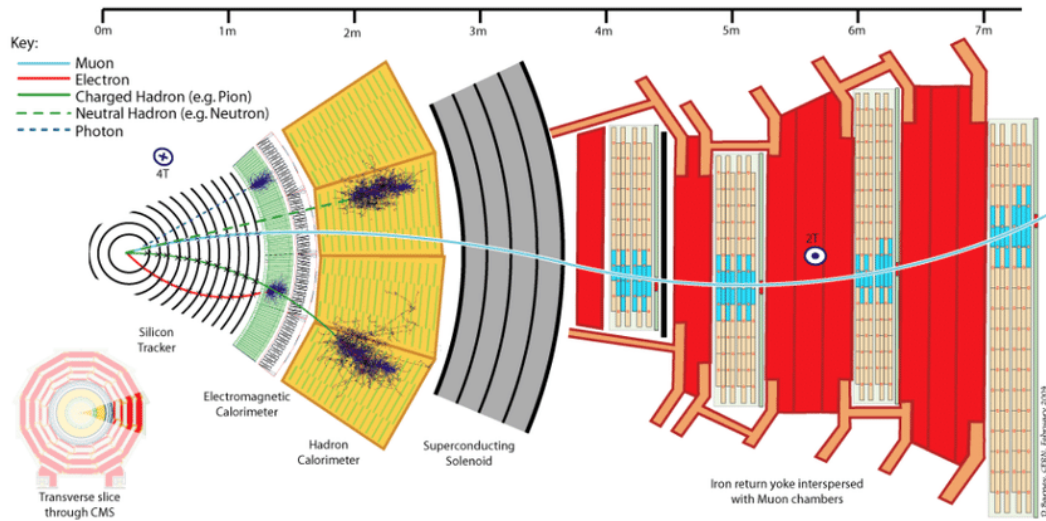


Figure 4.2: A transverse slice of the CMS detector highlighting interaction of different final state particles with the detector materials.

measured

- Electrons and photons are more likely to deposit their energy in the ECAL
- Hadrons are likely to deposit a small fraction of their energy in the ECAL and deposit most of their energy in the HCAL
- Muons produce track in the Muon chambers

A detailed description of reconstruction and identification of the various physics objects is given in the following sections.

4.4 Electron reconstruction and identification

An electron is reconstructed by the PF algorithm by matching an energy deposit in the ECAL with a track in the tracker [90–92]. To get the best estimate of the track parameters, the trajectory of the electron is refitted with a Gaussian-Sum Fitter (GSF) [93; 94].

Energy deposited by an electron in the ECAL is shared among several adjacent crystals. From beam tests, it has been found that 97% of the energy of a 120 GeV electron is contained in a 5×5 crystal matrix around the crystal with the highest energy deposit (seed crystal) [91]. Hence, several crystals around the seed crystal are combined to form a cluster. There is also a finite probability for electrons to lose energy through bremsstrahlung while traversing through the tracker material. The bremsstrahlung photons can form ECAL clusters with the same η value as the cluster formed by an electron, but separated in the ϕ direction. Bremsstrahlung can also lead to energy loss if the secondary electrons, created from pair-production of the bremsstrahlung photons, get trapped partially or completely inside the magnetic field and lose most of their energy before reaching the ECAL. To overcome the situation, electron superclusters are formed by joining clusters in the ϕ direction to also consider the amount of energy carried away by the bremsstrahlung photons. Two separate algorithms are used in the barrel and endcap regions of the ECAL to form clusters and superclusters [91].

A Boosted Decision Tree (BDT) [95] discriminant, which takes variables sensitive to the amount of bremsstrahlung along the electron trajectory as input, as shown in Table 4.1, is used to select the electron candidates. The BDT has been trained

on all the electrons having $p_T > 10 \text{ GeV}$, in three regions based on electron η : two for barrel and one for endcap. For all the three regions, two working points (WP), tight (with 80 % signal efficiency) and loose (with 90 % signal efficiency) are chosen. The definition of the three regions and the cut values on the BDT score corresponding to the tight and loose working points are given in Table 4.2.

Observable type	Observable name
Cluster shape	<ul style="list-style-type: none"> • RMS of the energy-crystal number spectrum along η and ϕ; $\sigma_{i\eta i\eta}$, $\sigma_{i\phi i\phi}$ • Super cluster width along η and ϕ • Ratio of the hadronic energy behind the electron supercluster to the supercluster energy, H/E • Circularity $((E_{5\times 5} - E_{5\times 1})/E_{5\times 1})$ • Sum of the seed and adjacent crystal over the super cluster energy R_9 • For endcap training bins: energy fraction in pre-shower E_{ps}/E_{raw}
track-cluster matching	<ul style="list-style-type: none"> • Energy-momentum agreement E_{tot}/p_{in}, E_{ele}/p_{out}, $1/E_{tot} - 1/p_{in}$ • Position matching $\Delta\eta_{in}$, $\Delta\phi_{in}$, $\Delta\eta_{seed}$
tracking	<ul style="list-style-type: none"> • Fractional momentum loss $f_{brem} = 1 - p_{out}/p_{in}$ • Number of hits of the KF and GSF track N_{KF}, N_{GSF} • Reduced χ^2 of the KF and GSF track χ_{KF}^2, χ_{GSF}^2 • Number of expected but missing inner hits • Probability transform of conversion vertex fit χ^2

Table 4.1: Details of the input variables used in the electron identification classifier.

Regions	Tight WP	Loose WP
Barrel ($ \eta < 0.8$)	0.941	0.837
Barrel ($0.8 < \eta < 1.479$)	0.899	0.715
Endcap ($ \eta > 1.479$)	0.758	0.357

Table 4.2: Minimum BDT scores required for electron identification for tight and loose WPs.

Isolation plays an important role in differentiating between prompt electrons and electrons inside a jet. Electrons are required to originate from the event vertex with

stringent cuts on the distance of the electron track from the event vertex along the longitudinal direction, $|\Delta_z|$ and in the transverse plane, Δ_{xy} .

Electron isolation refers to the total amount of energy deposited in a cone around the electron trajectory by charged and neutral particles from all the interaction vertices. While the charged particles from pileup interactions can be easily excluded from the estimation of isolation using the vertex information, the energy deposited by the neutral particles from pileup interactions can not be subtracted and must be parametrised in some suitable way.

The relative isolation of an electron can be expressed as,

$$I_{rel} = (\sum p_T^{charged} + \max[0, \sum p_T^{neutral-had} + \sum p_T^\gamma - \beta \sum p_T^{PU}]) / p_T \quad (4.1)$$

where $\sum p_T^{charged}$ is the scalar sum of transverse momenta of charged hadrons coming from the event vertex, and $\sum p_T^{neutral-had}$ and $\sum p_T^\gamma$ are the scalar sum of transverse momenta of the neutral hadrons and photons respectively, inside the cone under consideration. The neutral component from pileup interactions is estimated as a fraction (β) of the charged component from pileup ($\sum p_T^{PU}$), where β is estimated to be roughly 0.5 [2].

4.5 Photon Reconstruction

The PF algorithm reconstructs photons from the ECAL superclusters by requiring that no track should match the ECAL supercluster. Formation of an ECAL supercluster for a photon is analogous to that for an electron. The details of photon

reconstruction can be found in reference [92].

4.6 Muon reconstruction

The PF algorithm reconstructs muons combining information from the tracker and muon chambers [2].

- *Global muon reconstruction*: In this case, for each track reconstructed in the muon chambers (standalone muon track), a search is performed to find a matched track in the tracker by comparing the parameters of the two tracks propagated to a common surface. A global muon track is formed from a fit with the hits from the track in the tracker and the standalone muon track.
- *Tracker muon reconstruction*: Here, all the tracks from the tracker with $p_T > 0.5 \text{ GeV}$ and momentum $p > 2.5 \text{ GeV}$ are considered as possible muon candidates and propagated to the muon system taking into account the magnetic field, the average expected energy loss and multiple Coulomb scattering in the detector material. If an extrapolated track matches with at least one muon segment from a muon station (a short track reconstructed by one DT or CSC chamber), the track qualifies as a tracker muon.

A muon, reconstructed as global or tracker muon is usually considered as “loose”. To differentiate between the prompt muons and muons from decays in flight, a “tight” muon requirement is used, as follows,

- the muon must be reconstructed both as a global and tracker muon

- the global fit $\chi^2/d.o.f. < 10$
- the associated track in the tracker must satisfy the following conditions
 - matched with muon segments from at least two muon stations
 - > 10 tracker hits
 - at least one pixel hit
 - transverse impact parameter, $\Delta_{xy} < 2 \text{ mm}$

The efficiency of loose and tight muon reconstruction and identification, as measured with CMS data collected in 2015, is shown in Figure 4.3. The efficiency for the loose muon selection criteria is above 99% over the entire η range. The variation in efficiency for data and Monte-Carlo is within 1%. For the tight muon selection, the efficiency is 95 – 99% depending on η and the variation for data and Monte-Carlo is within 1 – 3%. The dips in efficiency for the tight muon selection near $|\eta| = 0.3$ are due to the effects of less instrumentation between the central muon wheel and the two neighbouring wheels. The tight muon selection efficiency is systematically higher for simulation compared to data due to imperfections in the modelling, which are revealed by the stringent requirements for the muons to satisfy the tight muon selection criteria. More detailed information about the loose and tight muon selection efficiency can be found in the reference [2].

An isolation requirement, similar to that used for electrons, is used to differentiate between prompt muons and muons inside a jet.

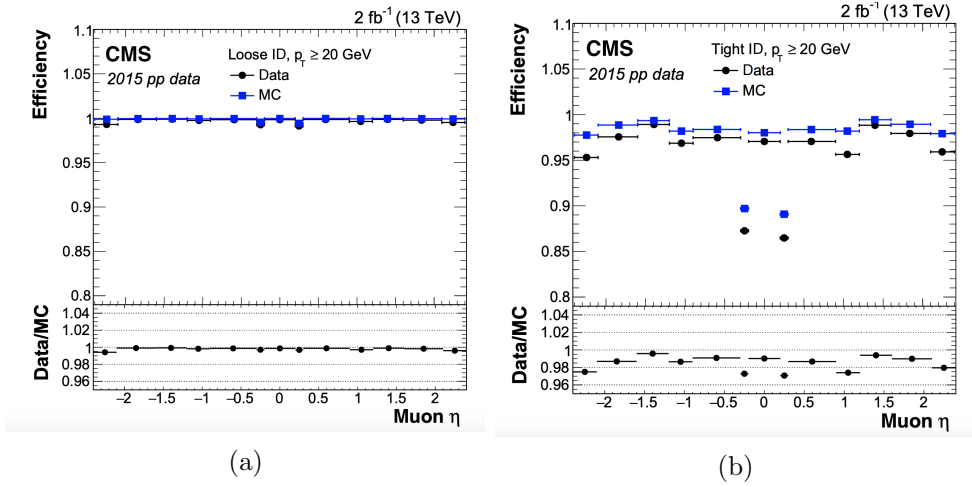


Figure 4.3: Muon reconstruction and identification efficiency for (a) loose and (b) tight muons as a function of η , measured with CMS data collected in 2015 [2].

4.7 Jet Clustering

Jets are experimental representation of quarks and gluons, collectively known as partons, produced in high-energy collisions, such as the p-p collisions at the LHC. The initial and final state partons, involved in a collision, proceed through radiation of gluons off quarks and gluon splitting into quarks to form a parton shower, and eventually produce colourless hadrons through fragmentation and hadronization [96]. The unstable hadrons decay and the final clusters of collimated energetic particles form jets. A precise understanding of the jet properties is essential as a test of QCD and to estimate the contribution of multi-jet background to Standard Model measurements and New Physics searches.

To know the properties of the quarks and gluons produced in the collision, it is important to properly reconstruct the jets in an event. Jet reconstruction proceeds

through clustering the final state particles or energy deposits in the detector using suitable jet clustering algorithms to form jets. A jet clustering algorithm should be infrared and collinear safe, i.e. the jet configuration should be independent of soft emission or collinear splitting of any parton [97]. In CMS, jets are reconstructed by clustering PF objects. By default, the anti- k_T [98; 99] clustering algorithm is used with the distance parameter, $R = 0.4$ (AK4 jets) and 0.8 (AK8 jets). The jet momentum is calculated by taking vectorial sum of the momenta of all the constituent PF objects in the jet. The invariant mass of the AK8 jets is calculated by the Soft Drop Algorithm [100; 101]. A series of calibration steps is performed to properly estimate the jet momentum and the uncertainty related to it [102; 103].

4.7.1 b-Jet

Hadrons containing bottom quarks have an average lifetime of 1.5 ps and an average $c\tau = 450\ \mu\text{m}$. A B-hadron having an energy of $50\ \text{GeV}$ travels about $5\ \text{mm}$ before decaying. Therefore, events with B-hadrons are characterised by displaced secondary vertices along the b-jet direction, as depicted in Figure 4.4. The secondary vertices can be reconstructed, thanks to the excellent vertex resolution of the CMS tracking detector, as shown in Figure 4.1. In CMS, a Combined Secondary Vertex (CSV) [104] algorithm is used to separate b-jets from light quark or gluon jets. The CSV algorithm combines all the variables sensitive to the presence of secondary vertices, in a single discriminant. The threshold on the CSV discriminant for three b-tagging working points are shown in Table 4.3.

The b-tagging efficiency and mis-tagging efficiency for c-jets and light quark jets,

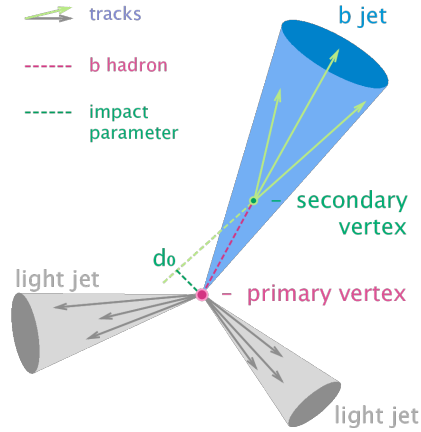


Figure 4.4: Secondary vertex formation for the b-jets.

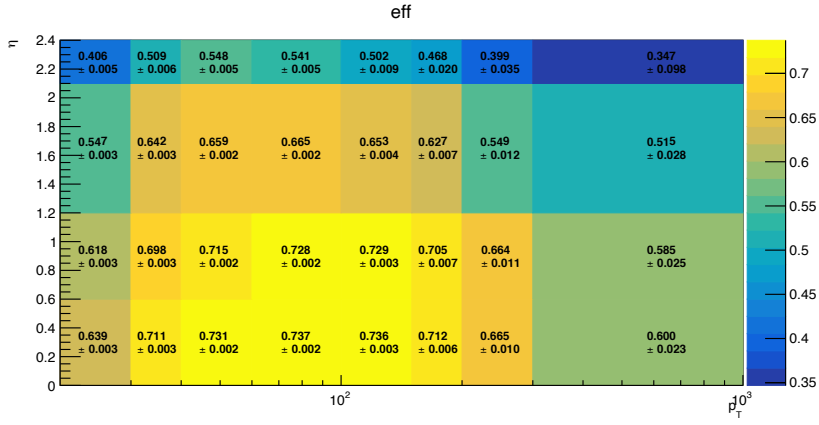
Working Point	Cut on CSV discriminant
Loose	0.5426
Medium	0.8484
Tight	0.9535

Table 4.3: b-Tagging working points and corresponding threshold on the CSV discriminant.

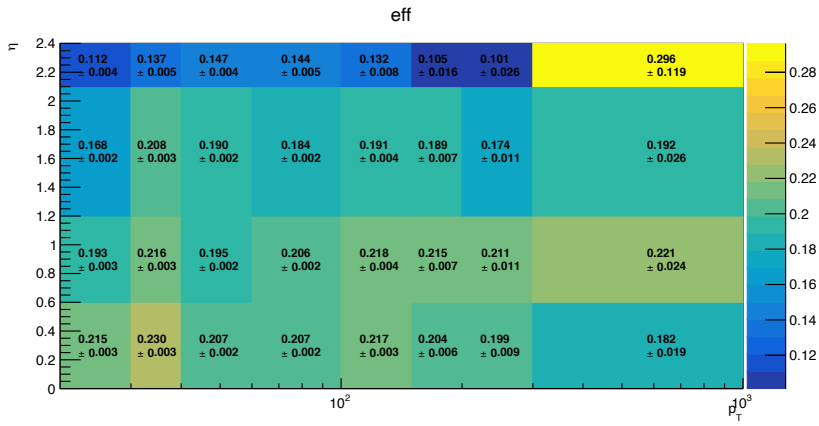
for the medium b-tagging working point is shown in Figure 4.5. The efficiency and mis-tagging efficiency are calculated with $t\bar{t}$ + jets events using Monte Carlo (MC) truth information.

4.8 Reconstruction of hadronic τ decays

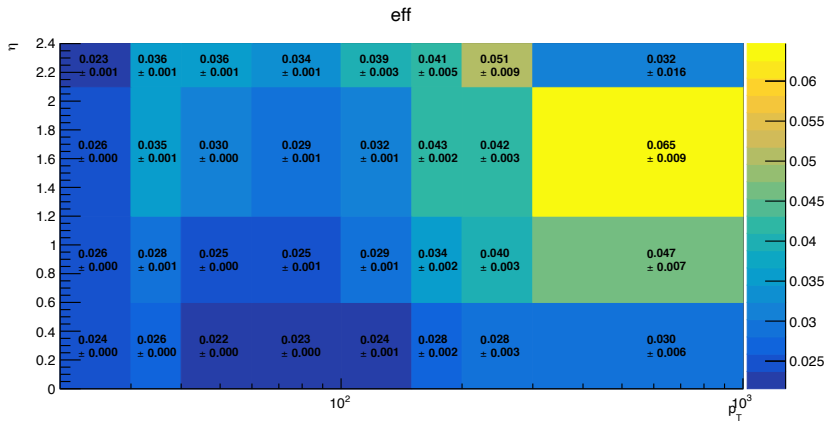
The τ lepton decays dominantly to hadrons (BR $\sim 66\%$), giving rise to narrow jets in the detector. The reconstruction of the hadronic decay of τ is performed by the Hadron Plus Strip (HPS) algorithm [3]. The HPS algorithm can reconstruct two



(a) b-jets



(b) c-jets



(c) light quark jets

Figure 4.5: The b-tagging efficiency for (a) b-jets, (b) c-jets and (c) light quark and gluon jets respectively.

hadronic τ (τ_h) decay modes:

- One prong - one charged hadron + ≥ 0 neutral hadrons
- Three prong - three charged hadrons + ≥ 0 neutral hadrons

The HPS algorithm considers anti- k_T jets in an event as input, with $R = 0.5$, with $p_T > 14 \text{ GeV}$ and $|\eta| < 2.5$. The algorithm tries to identify a jet as a τ_h candidate by checking the compatibility of the constituents of the jet to be reconstructed as one of the τ_h decay modes.

Isolation of the τ_h candidates is an important tool to differentiate between τ_h and quark or gluon induced jets. The MVA based isolation discriminant is computed by a BDT which takes the following variables as input,

- the charged part of the isolation within a cone of size $\Delta R < 0.5$ around the τ_h candidate, similar to what has been discussed for electron isolation in Section 4.4
- the neutral part of the isolation, calculated with a cone size $\Delta R < 0.5$ and $\beta = 0.46$, similar to what has been discussed for electron isolation in Section 4.4
- the decay mode of τ_h
- the transverse impact parameter of the leading track of τ_h and its significance
- the distance between the production and decay vertices of τ_h and its significance

The τ_h identification efficiencies for different MVA isolation working points, as measured in $Z/\gamma^* \rightarrow \tau\tau \rightarrow \mu\tau_h$ events with 19.7 fb^{-1} CMS data at 8 TeV , are shown

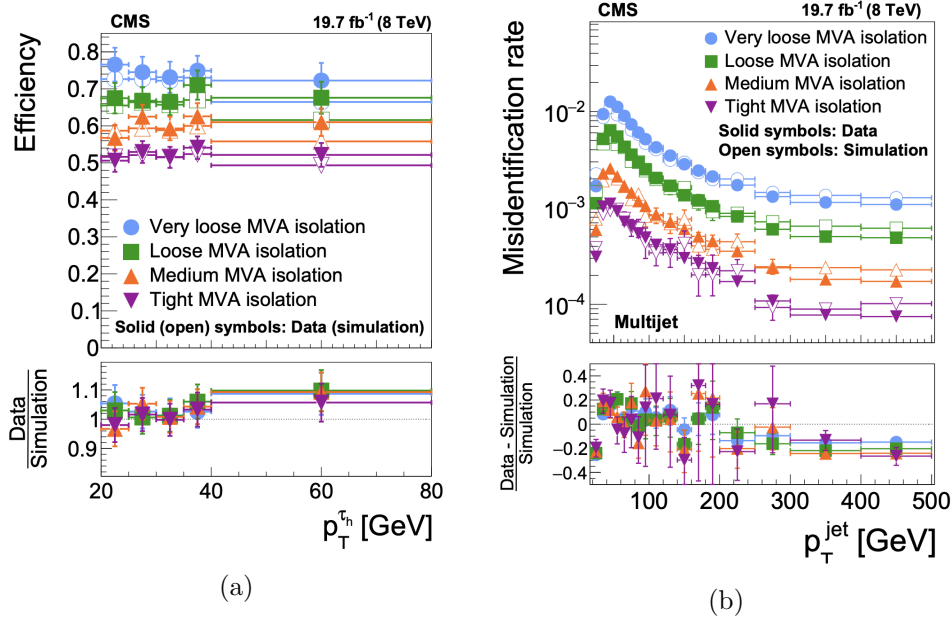


Figure 4.6: (a) τ_h identification efficiency as measured in the $Z/\gamma^* \rightarrow \tau\tau \rightarrow \mu\tau_h$ events and (b) Mis-identification efficiency of the jets as measured in the multi-jet events [3]. Values obtained for different MVA isolation discriminant working points are represented by different colours. The solid symbols represent the value obtained with 8 TeV CMS data corresponding to an integrated luminosity of 19.7 fb^{-1} . The open symbols represent the value obtained from the MC events.

in Figure 4.6a. The mis-identification efficiencies of the jets to be selected as τ_h candidates, for different MVA isolation working points, are shown in Figure 4.6b. The mis-identification efficiency is measured using multi-jet events with 19.7 fb^{-1} CMS data at 8 TeV. In both the figures, the value obtained with data is compared with the expected value obtained from MC events.

There is also a finite probability of an electron or a muon to be reconstructed as a τ_h candidate. Specific discriminants have been constructed to veto the electrons (*against electron discriminant*) and muons (*against muon discriminant*), erro-

neously reconstructed as τ_h candidates, using calorimeter and muon chamber informations. The mis-identification efficiency of the *against electron discriminant*, as measured in $Z/\gamma^* \rightarrow ee$ events, for 8 TeV CMS data with an integrated luminosity of 19.7 fb^{-1} is shown in Figure 4.7a and compared with estimates from MC. The identification efficiency of the *against electron discriminant* is $\sim 70\% - 85\%$, depending on the working point. Similarly, the mis-identification efficiency of the *against muon discriminant*, as measured in $Z/\gamma^* \rightarrow \mu\mu$ events, for 8 TeV CMS data with an integrated luminosity of 19.7 fb^{-1} is shown in Figure 4.7b and compared with estimates from MC. The identification efficiency of the *against muon discriminant* is above 99%.

4.8.1 Missing Transverse Momentum

Weakly interacting neutral particles, like the neutrinos in τ decays, escape detection. The presence of such particles can only be estimated from the imbalance in the total transverse momentum in the event, known as the missing transverse momentum, denoted by \vec{p}_T^{miss} . The magnitude of \vec{p}_T^{miss} is called missing transverse energy (MET) and is denoted by \cancel{E}_T .

The details of MET reconstruction in CMS can be found in reference [105]. The \vec{p}_T^{miss} is calculated by taking the negative of the vector sum of the momentum of all the reconstructed PF candidates.

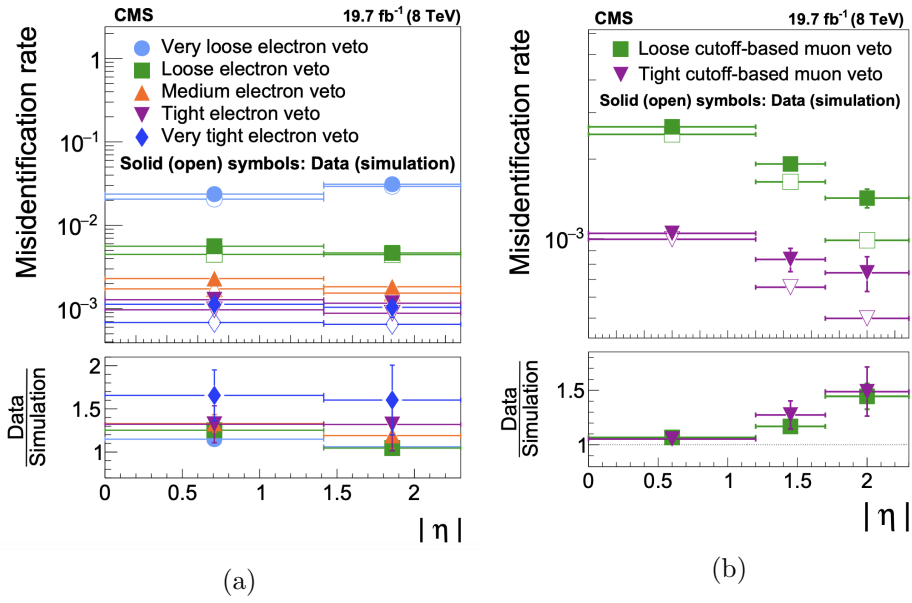


Figure 4.7: (a) Mis-identification efficiency for electrons for different *against electron discriminant* working points, as measured in $Z/\gamma^* \rightarrow ee$ events [3]. (b) Mis-identification efficiency for muons for different *against muon discriminant* working points, as measured in $Z/\gamma^* \rightarrow \mu\mu$ events. [3]. The solid symbols represent the values obtained with $19.7 fb^{-1}$ 8 TeV CMS data. The open symbols represent the value obtained with MC events.

Chapter 5

Search for Higgs boson pair production in the $b\bar{b}\tau\tau$ final state

In this chapter, a search for HH production in the $HH \rightarrow b\bar{b}\tau\tau$ final state will be described and the results based on data collected by CMS in 2016, corresponding to an integrated luminosity of 35.9 fb^{-1} , will be presented. The $HH \rightarrow b\bar{b}\tau\tau$ final state has a branching fraction of 7.3% of overall HH decay. Three decay modes of the τ lepton pair, namely, $\mu\tau_h$, $e\tau_h$ and $\tau_h\tau_h$, where τ_h represents the hadronically decaying τ lepton, are considered. The three decay modes constitute 80% of the total τ lepton pair decay.

The dominant sources of background to the $HH \rightarrow b\bar{b}\tau\tau$ final state are,

- $t\bar{t}$ + jets, where both the top quarks decay to bW . Leptonic or hadronic decay of the two W 's may give rise to topologies similar to the signal. A representative Feynman diagram for the process is shown in Figure 5.1a.

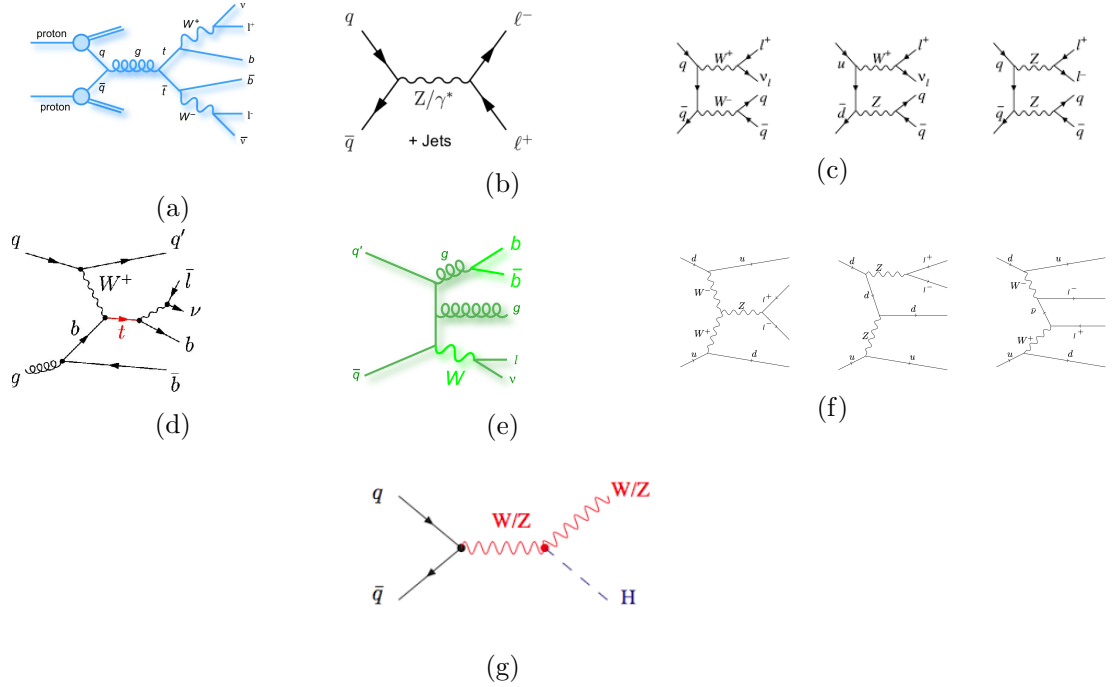


Figure 5.1: Feynman diagrams of various background processes to the $HH \rightarrow b\bar{b}\tau\tau$ final state, (a) $t\bar{t}$ + jets, (b) $Z/\gamma^* \rightarrow ll$ + jets, (c) di-boson, (d) single top, (e) W + jets, (f) Electroweak + two-jets, and (g) SM Higgs boson production.

- $Z/\gamma^* \rightarrow ll$ + jets (Drell-Yan), where the τ lepton pair from Z/γ^* and jets, which may be tagged as b-jets, can act as potential background. Figure 5.1b represents the Feynman diagram of the process.
- Jets, in QCD multi-jets events, can potentially mimic both b-jets and τ leptons.

There are also small contributions from di-boson, single top, $W \rightarrow l\nu$ + jets, Electroweak + two-jets, and associated production of the SM Higgs boson processes. Feynman diagrams for all such processes are shown in Figure 5.1.

5.0.1 High Level Trigger

The τ lepton pair decay signature has been used to trigger the events. For the $b\bar{b}\mu\tau_h$ and $b\bar{b}e\tau_h$ final states, SingleMuon and SingleElectron trigger paths are used to select events. Similarly, for the $b\bar{b}\tau_h\tau_h$ final state, double Tau trigger paths have been used.

The trigger paths used for each final state is shown in Table 5.1.

Channel	HLT path name
$b\bar{b}\mu\tau_h$	HLT_IsoMu22_eta2p1_v* HLT_IsoTkMu22_eta2p1_v* HLT_IsoMu22_v* HLT_IsoTkMu22_v*
$b\bar{b}e\tau_h$	HLT_Ele25_eta2p1_WPTight_Gsf_v*
$b\bar{b}\tau_h\tau_h$	HLT_DoubleMediumIsoPFTau35_Trk1_eta2p1_Reg_v* HLT_DoubleMediumCombinedIsoPFTau35_Trk1_eta2p1_Reg_v*

Table 5.1: Trigger paths used for the $b\bar{b}\mu\tau_h$, $b\bar{b}e\tau_h$ and $b\bar{b}\tau_h\tau_h$ final states.

5.1 Collision datasets

SingleMuon, SingleElectron and Tau primary CMS datasets of 2016 have been used in the analysis of $b\bar{b}\mu\tau_h$, $b\bar{b}e\tau_h$, and $b\bar{b}\tau_h\tau_h$ final states respectively. The details of the datasets are provided in Tables 10.1, 10.2 and 10.3 of Appendix 10.

5.2 Simulated events

The background and signal events are generated using various Monte-Carlo (MC) physics process generators, namely MADGRAPH5_aMC@NLO [82], POWHEG 2.0 [106];

[107] etc. The NNPDF3.0 [108] PDF set is used in the physics generation process. After the generation of the hard interaction step, events are interfaced with Pythia8.212 [84] with the CUETP8M1 [109] tune to simulate multi-parton interactions, parton showering and hadronization effects. The generated events are then passed through the standard CMS simulation and reconstruction procedure.

The simulated events are also required to pass the trigger selection for trigger paths mentioned in Table 5.1. To correct for the difference between the trigger efficiency in data and simulation, the simulated events are weighted by the trigger scale factors, defined as the ratio of the trigger efficiencies in data and simulation. The trigger scale factors are computed using $Z \rightarrow l^+l^-$ events.

5.2.1 Background datasets

The $Z/\gamma^* \rightarrow ll + \text{jets}$, $W \rightarrow l\nu + \text{jets}$, di-boson and SM Higgs boson background events have been generated with MADGRAPH5_aMC@NLO 2.3.2 at Leading Order (LO) with MLM merging [110]. The Electroweak + two-jets events have been generated with MADGRAPH5_aMC@NLO 2.3.2 at LO precision. The $t\bar{t} + \text{jets}$ and single top events have been generated with POWHEG 2.0 at Next-to-Leading Order (NLO) precision. The background datasets are listed in Tables 10.4, 10.5, 10.6 and 10.7 of Appendix 10.

The $t\bar{t} + \text{jets}$, $Z/\gamma^* \rightarrow ll + \text{jets}$, $W \rightarrow l\nu + \text{jets}$ and single top events are normalised to the respective cross-sections at the Next-to-Next-to-Leading Order (NNLO) precision [111–113]. The di-boson events are normalised to the cross-section at NLO precision [114]. The SM Higgs boson production is normalised to the cross-section,

computed with QCD corrections at NNLO precision and Electroweak corrections at the NLO precision [115–118].

The datasets for the $Z/\gamma^* \rightarrow ll + \text{jets}$ and $W \rightarrow l\nu + \text{jets}$ processes are shown in Table 10.4 of Appendix 10. The “inclusive” $Z/\gamma^* \rightarrow ll + \text{jets}$ and $W \rightarrow l\nu + \text{jets}$ events are generated with all possible values of,

- parton multiplicity
- b-parton multiplicity
- scalar sum of the transverse momentum of the partons (HT)

available at the matrix element level. There are also “exclusive” $Z/\gamma^* \rightarrow ll + \text{jets}$ and $W \rightarrow l\nu + \text{jets}$ datasets which are produced in certain selected regions of the above mentioned variables. In order to increase the statistics, exclusive datasets are merged with the inclusive dataset. The total simulated events are divided in mutually exclusive sets (S) depending on the parton multiplicity, b-parton multiplicity and HT. The obtained exclusive sets are merged with an event weight,

$$Weight(S) = \frac{n_S^{Inclusive}}{N_S} \quad (5.1)$$

where $n_S^{Inclusive}$ is the number of events in the inclusive dataset belonging to the particular set and N_S is the total number of events belonging to the particular set.

5.2.2 Signal datasets

MADGRAPH5_aMC@NLO 2.3.2 at LO precision has been used for both resonant and non-resonant signal event generation. Resonant $gg \rightarrow X \rightarrow HH \rightarrow b\bar{b}\tau\tau$ events

are generated under the assumption of narrow width of the resonant particle, X . Separate datasets are produced for the resonant particle mass ranging from 250 GeV to 900 GeV , and spin values of 0 and 2. The details of the resonant $HH \rightarrow b\bar{b}\tau\tau$ datasets are provided in Tables 10.8, and 10.9 of Appendix 10.

In the case of non-resonant signal events, from all possible values of the BSM couplings of the EFT, twelve shape benchmark points [11; 12] have been chosen, as shown in Table 5.2. The benchmark points are representative of the kinematics of all possible values of the coupling parameters of the EFT. Non-resonant signal datasets for four benchmark points, namely 2, 10, 11 and 12 and two SM points (shown in Table 5.3) have been produced. The box benchmark point in Table 5.3 corresponds to the Feynman diagram shown in Figures 5.2a, whereas, the SM benchmark point in Table 5.3 refers to the combination of both the Feynman diagrams shown in 5.2. The simulated datasets are re-weighted, based on their matrix-level kinematics, to model the non-resonant signal with additional values of the coupling parameters. The details of the simulated non-resonant signal datasets are provided in Table 10.10 of Appendix 10.

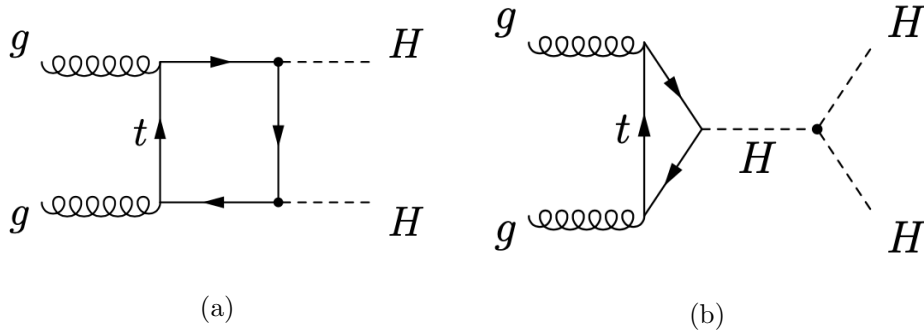


Figure 5.2: Feynman diagrams for the SM HH production.

Benchmark	κ_λ	κ_t	c_2	c_g	c_{2g}
1	7.5	1.0	-1.0	0.0	0.0
2	1.0	1.0	0.5	-0.8	0.6
3	1.0	1.0	-1.5	0.0	-0.8
4	-3.5	1.5	-3.0	0.0	0.0
5	1.0	1.0	0.0	0.8	-1.0
6	2.4	1.0	0.0	0.2	-0.2
7	5.0	1.0	0.0	0.2	-0.2
8	15.0	1.0	0.0	-1.0	1.0
9	1.0	1.0	1.0	-0.6	0.6
10	10.0	1.5	-1.0	0.0	0.0
11	2.4	1.0	0.0	1.0	-1.0
12	15.0	1.0	1.0	0.0	0.0

Table 5.2: The BSM shape benchmark points for the non-resonant $HH \rightarrow b\bar{b}\tau\tau$ production [11; 12].

Benchmark	κ_λ	κ_t	c_2	c_g	c_{2g}
Box	0.0	1.0	0.0	0.0	0.0
SM	1.0	1.0	0.0	0.0	0.0

Table 5.3: SM shape benchmark points for non-resonant $HH \rightarrow b\bar{b}\tau\tau$ production.

5.3 Event Selection

The event selection steps are as follows,

- electron, muon, τ_h and b-jet selection
- $H \rightarrow \tau\tau$ candidate selection
- $H \rightarrow b\bar{b}$ candidate selection
- Categorisation of events based on the jet configuration

- HH candidate selection
- Choice of the final discriminating variable

Reconstruction and identification of electron, muon, τ_h and b-jet have been discussed in Chapter 4.

5.3.1 Muon selection

Muon candidates are required to satisfy the following requirements,

- $p_T > 23 \text{ GeV}$
- $|\eta| < 2.1$
- tight muon selection
- $I_{rel} < 0.15$ calculated with a cone size of $\Delta R < 0.4$
- $\Delta_{xy} < 0.045 \text{ mm}$ and $|\Delta_z| < 0.2 \text{ mm}$ from the event vertex

5.3.2 Electron selection

Electron candidates should satisfy the conditions listed below,

- $p_T > 27 \text{ GeV}$
- $|\eta| < 2.1$
- pass the tight MVA selection requirement
- $I_{rel} < 0.1$ calculated with a cone size of $\Delta R < 0.3$

Variables	$\mu\tau_h$	$e\tau_h$	$\tau_h\tau_h$
$p_T (GeV)$	> 20	> 20	> 45
$ \eta $	< 2.3	< 2.3	< 2.1
MVA Isolation discriminator	Medium	Medium	Medium
Against Electron discriminator	Very loose	Tight	Very Loose
Against Muon discriminator	Tight	Loose	Loose
Δ_{xy} from event vertex (mm)	0.045	0.045	0.045
$ \Delta_z $ from event vertex (mm)	0.2	0.2	0.2

Table 5.4: Selection conditions for the τ_h candidate for different final states.

- $\Delta_{xy} < 0.045 \text{ mm}$ and $|\Delta_z| < 0.2 \text{ mm}$ from the event vertex

5.3.3 τ_h selection

The selection conditions for the τ_h candidates for the three different final states are shown in Table 5.4.

5.3.4 Selection of the $H \rightarrow \tau\tau$ candidate

In the $b\bar{b}\mu\tau_h$ ($b\bar{b}e\tau_h$) final state, events are required to have one muon (electron) candidate which passes the muon (electron) selection conditions mentioned above and matches with the trigger object. The events are further required to have one τ_h candidate passing the τ_h selection requirement listed in the $\mu\tau_h$ ($e\tau_h$) column in Table 5.4. The muon (electron) and τ_h candidates should have opposite charges and should be separated by, $\Delta R > 0.1$. In case there are more than one τ_h candidates, the one with the highest value of the MVA Isolation discriminant is chosen.

For the $b\bar{b}\tau_h\tau_h$ final state, the events are required to have two τ_h candidates, both

passing the τ_h selection criteria given in the $\tau_h\tau_h$ column of Table 5.4 and matching with the trigger objects. The τ_h candidates should have opposite charges and should be separated by, $\Delta R > 0.1$.

Events are rejected if an additional muon or electron other than the candidate muon or electron is present in the event. The selection requirements for veto muons are,

- $p_T > 10 \text{ GeV}$
- $|\eta| < 2.4$
- loose muon selection
- $I_{rel} < 0.3$ calculated with a cone size of $\Delta R < 0.4$
- $\Delta_{xy} < 0.045 \text{ mm}$ and $|\Delta_z| < 0.2 \text{ mm}$ from the event vertex

Similarly, the selection requirements for the veto electrons are,

- $p_T > 10 \text{ GeV}$
- $|\eta| < 2.5$
- pass the loose MVA requirement
- $I_{rel} < 0.3$ calculated with a cone size of $\Delta R < 0.3$
- $\Delta_{xy} < 0.045 \text{ mm}$ and $|\Delta_z| < 0.2 \text{ mm}$ from the event vertex

5.3.5 Selection of the $H \rightarrow b\bar{b}$ candidate

Events are required to have at least two jets, passing the selection requirements shown in Table 5.5. Jets should be separated from the lepton candidates by, $\Delta R > 0.5$. The two jets having the highest CSV discriminator value are considered to form the $H \rightarrow b\bar{b}$ candidate.

Variable	Condition
p_T	$> 20 \text{ GeV}$
$ \eta $	< 2.4
Neutral hadron fraction	< 0.99
Neutral electro-magnetic fraction	< 0.99
Number of constituents	> 1
Charged hadron fraction	> 0
Charged multiplicity	> 0
Charged electro-magnetic fraction	< 0.99

Table 5.5: Jet selection criteria.

5.3.6 Categorisation of events based on jet configuration

$H \rightarrow b\bar{b}$ decay may give rise to the following possible scenarios depending on the separation between the two b-quarks.

- if the b-quarks are separated by a distance of $\Delta R(b, b) > 0.8$, each quark will be clustered as a jet by itself, with both AK4 and AK8 algorithms, as shown in Figure 5.3a.
- if the b-quarks are separated by a distance $0.4 < \Delta R(b, b) < 0.8$, they will be clustered as separate jets with the AK4 algorithm, but as a single jet with the

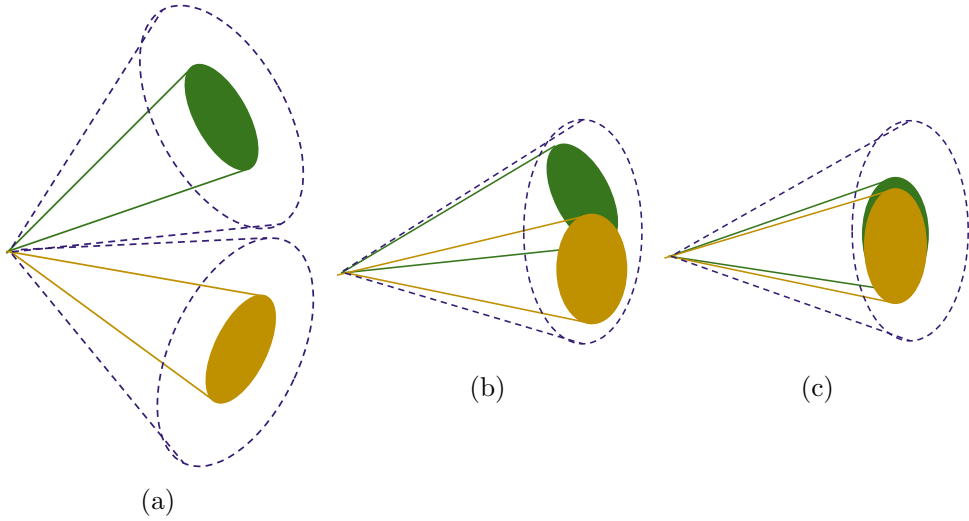


Figure 5.3: Different possible scenarios depending on the separation of the two b -quarks, (a) $\Delta R(b, b) > 0.8$, (b) $0.4 < \Delta R(b, b) < 0.8$ and (c) $\Delta R(b, b) < 0.4$. In all the cases, green and yellow cones represent AK4 jets and violet cones represent AK8 jet.

AK8 algorithm, as shown in Figure 5.3b.

- if the b -quarks are separated by a distance $\Delta R < 0.4$, both the quarks will be clustered into a single jet with both AK4 and AK8 algorithms, as shown in Figure 5.3c, and highly sophisticated techniques would be required to reconstruct the $H \rightarrow b\bar{b}$ candidate, which was not attempted in the present study.

The first two scenarios fall in the “Resolved” and “Boosted” categories, respectively. It is verified from simulation that the third possibility is relevant only for the resonant HH production, when the mass of the resonant particle is above 900 GeV . In the present analysis, the resonant particle mass is considered upto 900 GeV and therefore, the third scenario is not considered.

In the “Boosted” category, the events are required to have an AK8 jet, with $m_{AK8,jet} > 30 \text{ GeV}$, consisting of at least two sub-jets which geometrically match the selected AK4 jets. The selected AK4 jets are required to pass the loose b-tagging working point.

The rest of the selected events are classified as “Resolved” which is further classified depending on number of b-tagged jets in the event as,

- **resolved 2jet-1tag (1b1j)**, where only one of the two AK4 jet passes the medium b-tagging working point
- **resolved 2jet-2tag (2b0j)**, where both the jets pass the medium b-tagging working point

5.3.7 HH candidate selection

To select the HH candidate(s) in an event, invariant masses of the $H \rightarrow \tau\tau$ and $H \rightarrow b\bar{b}$ candidates are used.

The invariant mass of the $H \rightarrow \tau\tau$ candidate is reconstructed using a dynamic likelihood fitting technique, called SVFit [119]. The SVFit algorithm quantifies the level of compatibility between a Higgs mass hypothesis and the measured momenta of the visible decay products of the τ leptons along with the MET reconstructed in the event.

In the “Resolved” category, the invariant mass of the $H \rightarrow b\bar{b}$ candidate is estimated using the two selected AK4 jets. An elliptical mass cut on the $H \rightarrow \tau\tau$ and

$H \rightarrow b\bar{b}$ candidate is applied,

$$\frac{(m_{\tau\tau} - 116 \text{ GeV})^2}{(35 \text{ GeV})^2} + \frac{(m_{bb} - 111 \text{ GeV})^2}{(45 \text{ GeV})^2} < 1 \quad (5.2)$$

The radii (35 GeV for the $H \rightarrow \tau\tau$ candidate and 45 GeV for $H \rightarrow b\bar{b}$ candidate) and the centre of the ellipse (116 GeV and 111 GeV for $H \rightarrow \tau\tau$ and $H \rightarrow b\bar{b}$ candidates respectively) are chosen according to the mass resolutions and expected positions of the 125 GeV Higgs boson peak for the $\tau\tau$ and jet pair systems, estimated using simulated events. This condition is optimised for the SM HH events with 80% signal efficiency and 85% background reduction in the $\mu\tau_h$ channel.

In the ‘‘Boosted’’ category, the invariant mass of the $H \rightarrow b\bar{b}$ candidate is estimated using the AK8 jet. The invariant mass of the $H \rightarrow b\bar{b}$ and $H \rightarrow \tau\tau$ candidates are required to satisfy the following condition,

$$\begin{aligned} 80 < m_{\tau\tau} < 152 \text{ GeV}, \\ 90 < m_{bb} < 160 \text{ GeV}. \end{aligned} \quad (5.3)$$

To further reduce the $t\bar{t}$ background in the semi-leptonic channels, two separate BDTs, with two different sets of kinematic variables as input, have been used in the search for resonant production. The BDTs for the resonant particle mass $> 350 \text{ GeV}$ and $< 350 \text{ GeV}$ are termed as high-mass (HM) and low-mass (LM) BDTs respectively. For non-resonant production, the LM BDT is found to be useful with a different training performed with the non-resonant HH signal events. The output ROC curves for all the signal scenarios have been shown in Figure 5.4. For resonant production, the point with 90% background rejection is chosen as the working point

while for non-resonant production, the point with 70 % background rejection is chosen as the working point.

5.3.8 Final discriminating variables

To look for any excess in the data over background expectation, one or more suitable variables, with good discriminating power, must be selected.

For resonant production, the combined invariant mass of the two Higgs candidates (m_{HH}) is the natural choice, which is computed from the informations of two lepton candidates, two jet candidates and MET in the event by the HHKinFit algorithm [120], and is denoted by m_{HH}^{KinFit} . HHKinFit is based on the hypothesis that the candidate leptons and jets originated from two 125 GeV Higgs bosons.

For non-resonant production, a mass bound variable called the stransverse mass (m_{T2}) [4; 121; 122] is used which is designed for those cases, where two parent particles of equal mass decay into a visible and an invisible components,

$$A \rightarrow B + C, A' \rightarrow B' + C' \quad (5.4)$$

Where A and A' are particles of equal mass and B (B') and C (C') denote the visible and invisible components respectively. m_{T2} is designed to provide the maximum allowed mass of the particle A (A').

The dominant background $t\bar{t} \rightarrow b\bar{b} WW \rightarrow b\bar{b}\tau\tau\nu\nu$ is such an example, where the two identical mass parents both decay into a visible component (i.e. b-jets and visible product of the τ decay) and an invisible component (neutrinos in W decay chain). In contrast, for signal (HH) events, one Higgs boson decays to $b\bar{b}$ (visible)

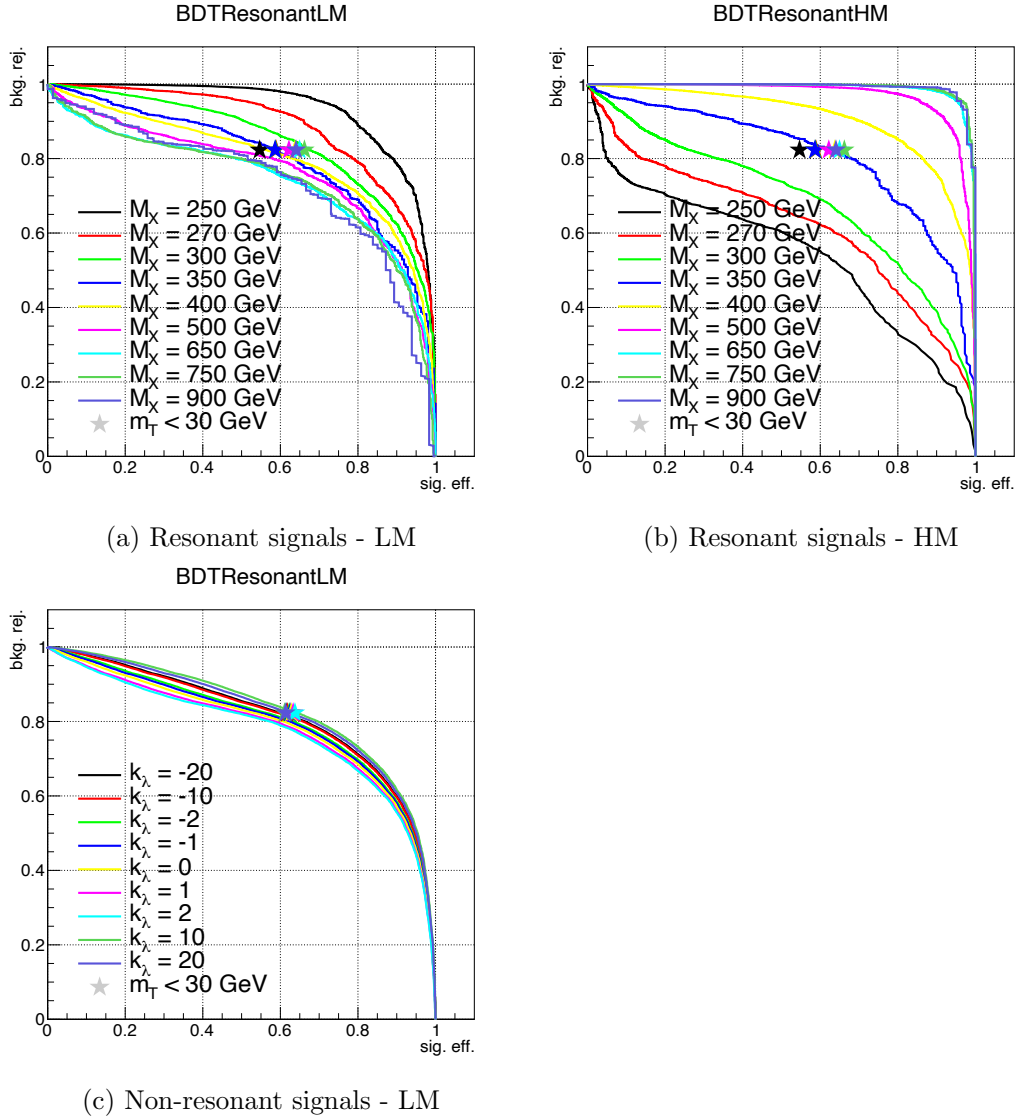


Figure 5.4: ROC curves for $t\bar{t}$ background rejection and signal efficiencies for (a) low-mass resonant production, (b) high-mass resonant production and (c) non-resonant production with low-mass BDT.

while the other decays to $\tau_h \tau_h$ (both visible and invisible). m_{T2} may, therefore, be used to separate signal from $t\bar{t}$ background as proposed in reference [4].

The transverse mass (m_T) of the particle A, decaying to a visible part B and an invisible part C, can be calculated as,

$$m_T(\vec{b}_T, \vec{c}_T, m_b, m_c) = \sqrt{m_b^2 + m_c^2 + 2(e_b e_c - \vec{b}_T \cdot \vec{c}_T)}, \quad (5.5)$$

where

- \vec{b}_T and m_b are the transverse momentum and mass of the visible part (B) respectively
- \vec{c}_T and m_c are the transverse momentum and mass of the invisible part (C), both being unknown and hypothesized
- e s are the transverse energy, defined as $e = \sqrt{m^2 + p_T^2}$

A similar equation can be written for the particle A' decaying to a visible part B' and an invisible part C'.

The m_{T2} of the event is calculated from the transverse masses of two A particles as,

$$m_{T2}(m_b, m_{b'}, \vec{b}_T, \vec{b}'_T, \vec{p}_T^\Sigma, m_c, m_{c'}) = \min_{\vec{c}_T + \vec{c}'_T = \vec{p}_T^\Sigma} \max(m_T, m'_T), \quad (5.6)$$

where,

- \vec{p}_T^Σ is the vector sum of the transverse components of the momentum of the two C particles, which is experimentally measured as \vec{p}_T^{miss}

The minimisation of the Equation 5.6 is performed over all the hypothesized values of the \vec{c}_T and \vec{c}'_T , where $\vec{c}_T + \vec{c}'_T = \vec{p}_T^\Sigma$.

In the $HH \rightarrow b\bar{b}\tau\tau$ analysis, the m_{T2} is calculated in a slightly different way, following Reference [4], by assigning,

- m_b and $m_{b'}$ as mass of the two selected jets
- \vec{b}_T and \vec{b}'_T as transverse momenta of the jets
- m_c and $m_{c'}$ as the experimentally measured mass of the two τ candidates
- $\vec{p}_T^\Sigma = \vec{p}_T(\tau_1) + \vec{p}_T(\tau_2) + \vec{p}_T^{miss}$

As can be seen from Figure 5.5, the m_{T2} variable is bounded by the top quark mass for the $t\bar{t}$ background, by definition. As a result, m_{T2} is expected to have a good discriminating power for signal and background. However, in $t\bar{t}$ decay, due to detector resolution effects and presence other decay modes of $t\bar{t}$ (like the jets from W decay erroneously detected as τ_h candidate), there will be an extension of the tail of the m_{T2} distribution beyond the top quark mass.

5.4 Background estimation

Different sources of background events survive the complete chain of event selection and must be correctly estimated. Shape and normalisation of background events are estimated in the following way,

- Both the shape and normalisation of the $t\bar{t}$ + jets, SM Higgs boson production,

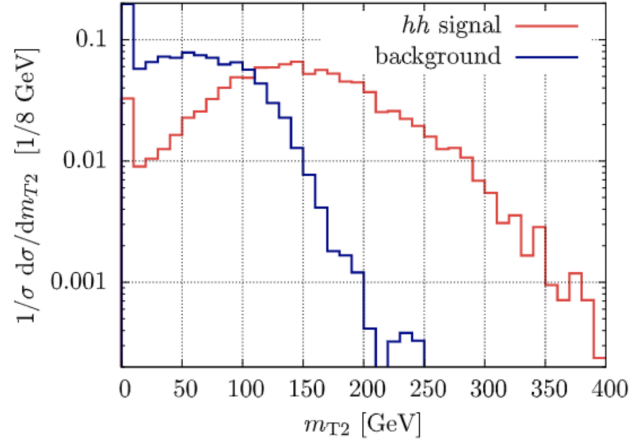


Figure 5.5: m_{T2} distribution for non-resonant HH signal events (solid red line) and $t\bar{t}$ background (solid blue line) [4]

$W \rightarrow l\nu + \text{jets}$, di-boson, single top and Electroweak + two-jets background processes are estimated from MC simulated events

- The shape of the Drell-Yan background is estimated from the Drell-Yan LO MC simulated events. However, jet emission in the Drell-Yan LO MC simulated events may not be perfectly modelled. Hence a data-driven approach is used to estimate the normalisation of the Drell-Yan background.
- Due to imperfect modelling of jet emission and limited MC statistics, QCD background contribution is estimated using a data-driven approach

5.4.1 QCD multi-jet event

The contribution of the QCD multi-jet events, where jets can fake τ leptons in the detector, is estimated by a data driven approach using a jet-enriched control region.

The background estimation is performed by a classic *ABCD* [123] method, as shown in Figure 5.6 where charge of the τ pair is plotted along the x axis and isolation requirement on the τ candidates is plotted along the y axis. The definition of each region is as follows,

- Region (A): events in this region must pass the main selection requirements. Therefore, this region is considered as the signal region in the analysis. The τ candidates are isolated and have opposite charges in this region. The region is also referred as the Opposite Sign (OS) isolated region.
- Region (B): selection requirements are the same as in region A, except that the opposite charge requirement between the two τ candidates is inverted. The τ candidates are isolated and have the same charge in this region. The region is also called the Same Sign (SS) isolated region.
- Region (B'): this region is the same as region B, but the isolation requirement is relaxed to increase statistics
- Region (C): selection requirements are the same as in region A, except that the τ candidates are required to fail the isolation requirement. The τ candidates are non-isolated and have opposite charges in this region. The region is also called the Opposite Sign (OS) non-isolated region.
- Region (D): the τ candidates are required to have the same charge and fail the isolation requirement. The τ candidates are non-isolated and have the same charge in this region. The region is also called the Same Sign (SS) non-isolated region.

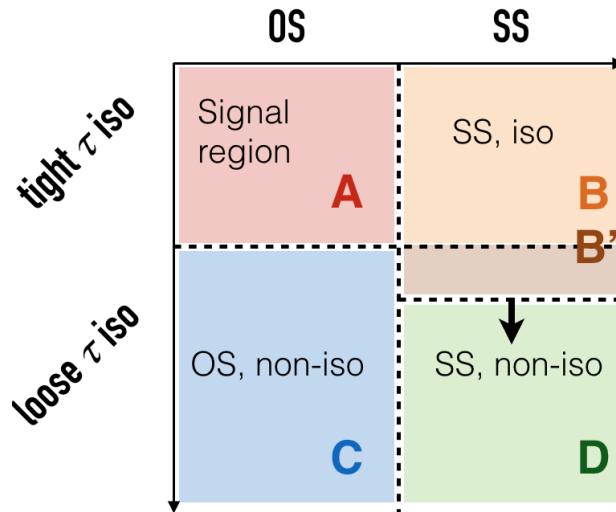


Figure 5.6: A sketch of different regions used for the QCD background estimation. The charge of the τ pair is plotted along the x axis, while the isolation requirement on the τ candidates is plotted along the y axis.

The yield of the QCD events in the signal region A is estimated from the region B, weighting by the OS/SS correction factor, which is estimated from the region C and D, i.e.

$$A = \frac{B \times C}{D} \quad (5.7)$$

The shape of the QCD events in the signal region A, is estimated from the region B', due to low statistics in the region B.

5.4.2 Drell-Yan + jets background estimation

The Drell-Yan + jets is a major source of background in the present analysis. The shape of the Drell-Yan + jets background is estimated from LO MC events, where the modelling of jet emission at LO is known to be imprecise [124]. Therefore, the normalisation of the Drell-Yan background is based on a data driven technique where a $Z/\gamma^* \rightarrow \mu^+\mu^- + \text{jets}$ control region is used which has no contribution from signal events. Physics objects in the control region have kinematics similar to that of the signal region.

Selection of the $Z/\gamma^* \rightarrow \mu^+\mu^- + \text{jets}$ control region requires that events should have two muons with opposite charges. Jet selection is the same as in the main analysis. The invariant mass of the jet pair should satisfy $80 < m_{jj} < 160 \text{ GeV}$ while the invariant mass of the muon pair should satisfy, $m_{\mu\mu} > 60 \text{ GeV}$. To reduce contamination from $t\bar{t}$ events, a cut on the missing transverse momentum, $p_T^{\text{miss}} < 45 \text{ GeV}$ is used. The events are grouped in three categories based on the number of b-tagged jets,

- $Z/\gamma^* + 0$ b-Tagged jet
- $Z/\gamma^* + 1$ b-Tagged jet
- $Z/\gamma^* + 2$ b-Tagged jets

In each category, the MC Drell-Yan events are also split in three MC templates based on the number of b-jets at the generator level,

- $Z/\gamma^* + \text{light jets}$

- $Z/\gamma^* + 1$ b jet
- $Z/\gamma^* + \geq 2$ b jets

A single MC template for all the other backgrounds is also used.

The distribution of the invariant mass of the muon pair ($m_{\mu^+\mu^-}$) is shown in Figure 5.7, for all the three categories.

In all the categories, the $m_{\mu^+\mu^-}$ distribution for data is fitted simultaneously with the four MC templates described above, keeping the normalisation of the MC templates floating. The fit in three categories is shown in Figure 5.8. The normalisation correction factors (scale factors) obtained for the three Drell-Yan MC templates are shown in Table 5.6.

	$Z/\gamma^* + \text{light jets}$	$Z/\gamma^* + 1 \text{ b jet}$	$Z/\gamma^* + \geq 2 \text{ b jets}$
Scale factors	1.412 ± 0.0017	1.187 ± 0.015	1.170 ± 0.029

Table 5.6: Scale factors for normalisation of Drell-Yan + jets background.

The Drell-Yan MC events in the signal region are weighted with the estimated scale factors to correct the normalisation and the error on the scale factors are considered as a source of systematic uncertainty.

5.5 Systematic Uncertainties

Two different sources of systematic uncertainties are considered,

- Uncertainties which affect the normalisation of different processes (shown in Table 5.7)

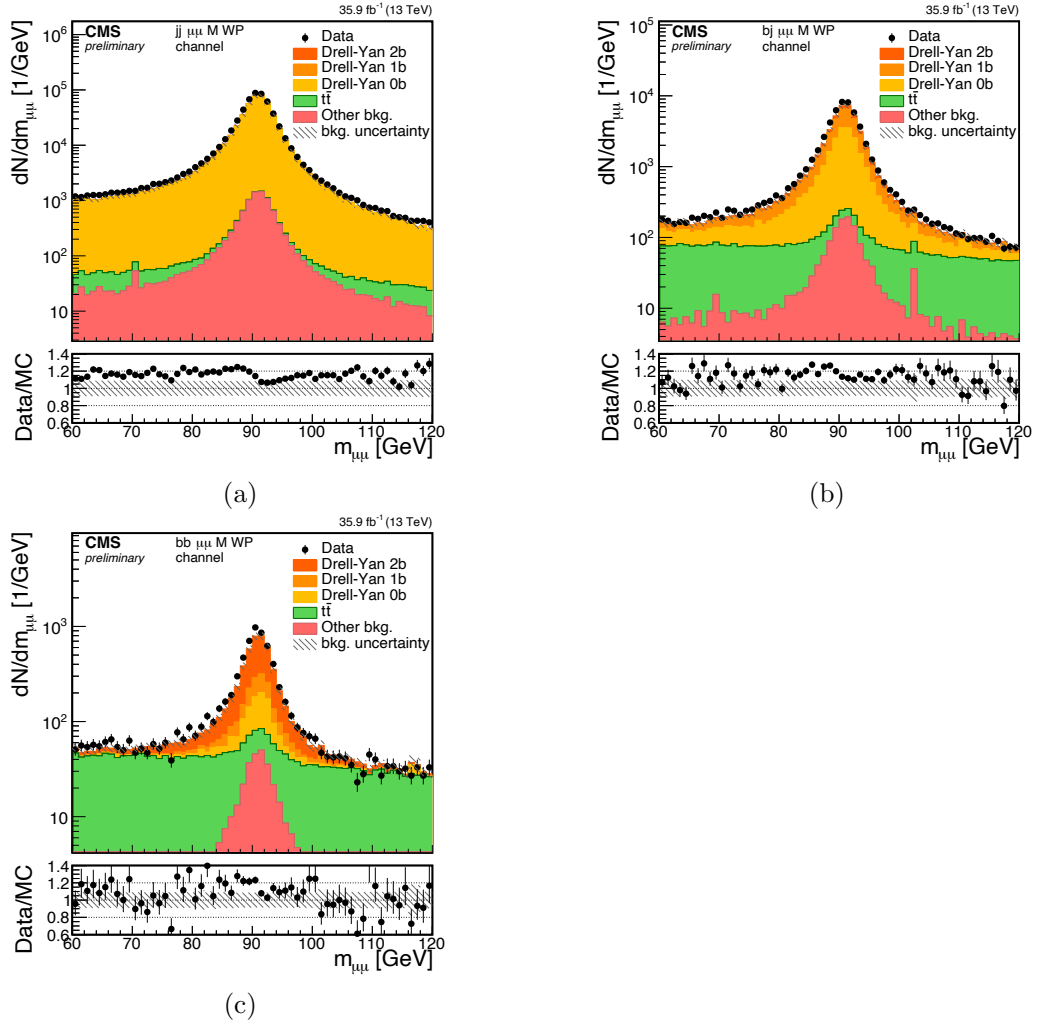


Figure 5.7: $m_{\mu^+\mu^-}$ distribution for (a) $Z + 0$ b-tagged jet, (b) $Z + 1$ b-tagged jet, and (c) $Z + 2$ b-tagged jets categories. The black dots represent data and coloured filled histograms represent MC events. The MC events are stacked up. The ratio between data and MC is also shown.

- Uncertainties which affect the shape of distributions for different processes (shown in Table 5.8)

Systematic	value	processes
Luminosity	2.5 %	all but multi-jet, $Z/\gamma^* \rightarrow ll + \text{jets}$
Lepton trigger and reconstruction	2 – 6 %	all but multi-jet
Uncertainties related to τ_h calibration	3 – 10 %	all but multi-jet
Uncertainties related to jet calibration	2 – 4 %	all but multi-jet
b-tag efficiency	2 – 6 %	all but multi-jet
Background cross-section	1 – 10 %	all but multi-jet, $Z/\gamma^* \rightarrow ll + \text{jets}$
$Z/\gamma^* \rightarrow ll + \text{jets}$ SF uncertainty	0.1 – 2.5 %	$Z/\gamma^* \rightarrow ll + \text{jets}$
multi-jet normalisation	5 – 30 %	multi-jet
scale unc.	+4.3 % / – 6 %	signals
Theory unc.	5.9 %	signals

Table 5.7: Systematic uncertainties, which affect normalisation of different processes.

Shape Uncertainties
Uncertainties related to τ_h calibration
Uncertainties related to jet calibration
top p_T reweighing
QCD background estimation
additional uncertainties for bins with low statistics

Table 5.8: Systematic uncertainties, which affect shape of distributions for different processes.

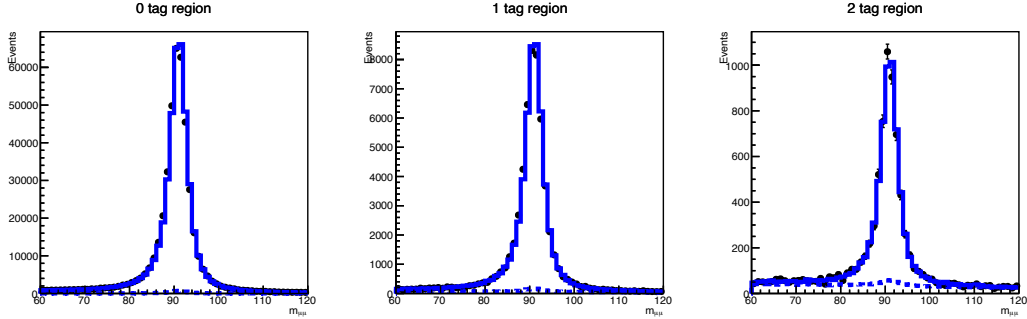


Figure 5.8: $m_{\mu^+\mu^-}$ distribution after the simultaneous fit in (left) $Z + 0$ b-tagged jet, (centre) $Z + 1$ b-tagged jet and (right) $Z + 2$ b-tagged jets. The black dots represent data points, The solid blue lines represent the obtained pdf combining the three Drell-Yan MC templates. The dashed blue lines represent the MC template for all other backgrounds.

5.6 Results

Figures 5.9, 5.10 and 5.11 show distributions of m_{HH}^{KinFit} and m_{T2} in the $b\bar{b}\mu\tau_h$, $b\bar{b}e\tau_h$ and $b\bar{b}\tau_h\tau_h$ final states respectively, for different categories. The presence of resonant signal should result in a localised excess in the m_{HH}^{KinFit} distribution while that for the non-resonant signal will end up in an excess of events in the tail of the m_{T2} distribution. A binned maximum likelihood fit is performed simultaneously in all the categories for the three final states. The fit is performed by the CMS Higgs Combined Tool [125] where the m_{HH}^{KinFit} and m_{T2} distributions for data, background, and signal events are used as input. The systematic uncertainties, discussed in the previous section, are used as the nuisance parameters of the fit. As there is no evidence of signal, a 95 % CL upper limit is set on $\sigma_{HH} \times \mathcal{B}(HH \rightarrow b\bar{b}\tau\tau)$ using the asymptotic modified frequentist approach [126; 127].

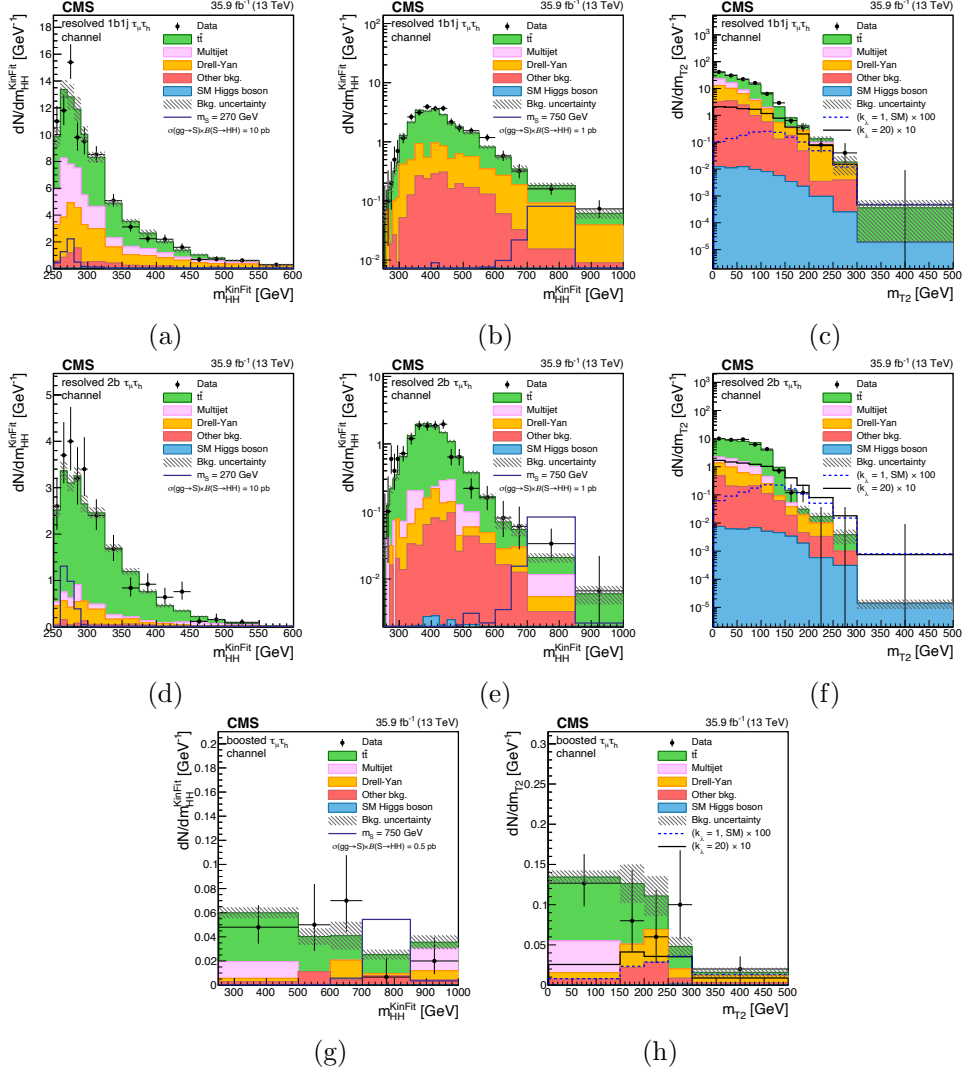


Figure 5.9: Distribution of the final discriminating variables for the $bb\bar{\mu}\tau_h$ final state. Panels a and d, show the distribution of m_{HH}^{KinFit} in the low-mass (LM) resonant signal region for resolved 1b1j and 2b categories respectively. Panels b and e show the distribution of m_{HH}^{KinFit} in the high-mass (HM) resonant signal regions for resolved 1b1j and 2b categories respectively. g shows the distribution of m_{HH}^{KinFit} in the resonant signal region for the boosted category. Panels c, f and h show the distribution of m_{T2} in the non-resonant signal region for resolved 1b1j, 2b and boosted categories respectively. Data are represented by points with error bars and expected signal contributions are represented by the solid (BSM HH signals) and dashed (SM non-resonant HH signal) lines. Expected background contributions (shaded histograms) and associated systematic uncertainties (dashed areas) are also shown. The background histograms are stacked.

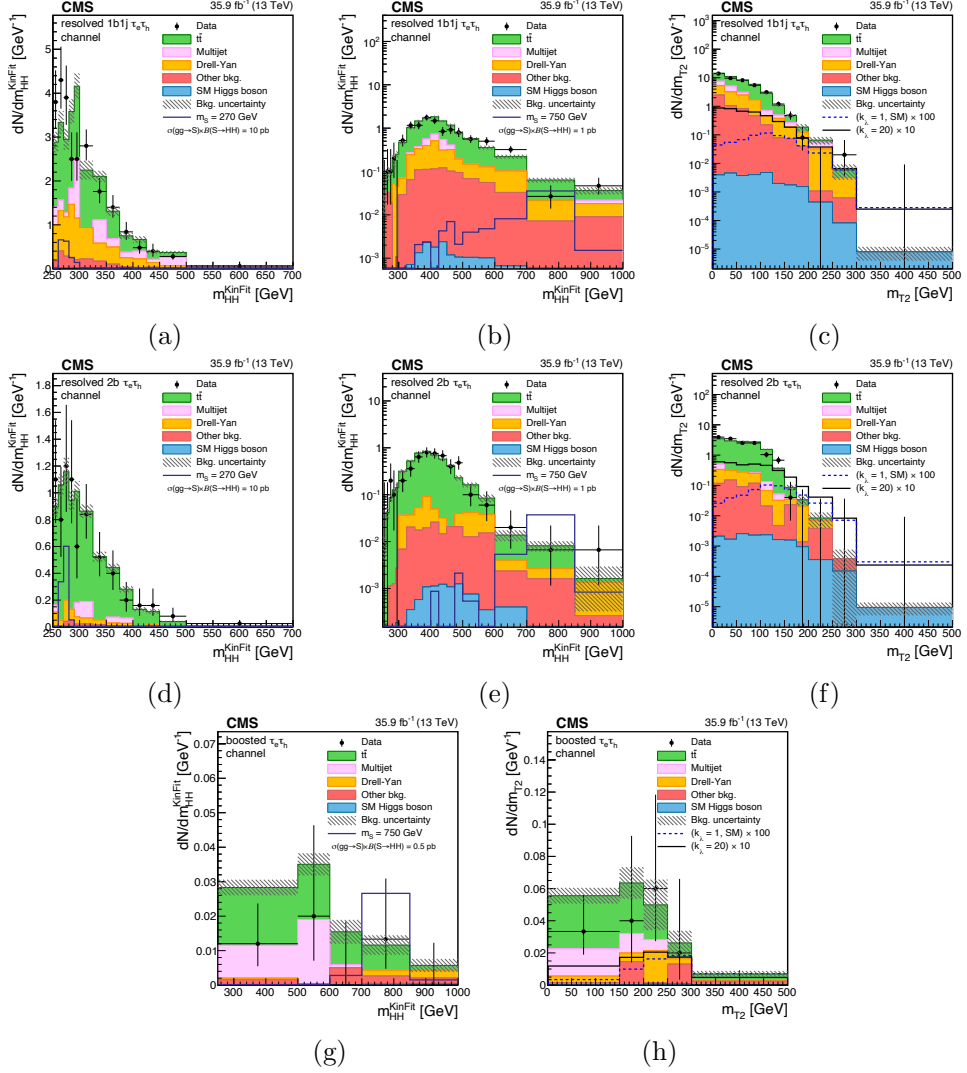


Figure 5.10: Distributions of the final discriminating variables for the $b\bar{b}e\tau_h$ final state. Panels **a** and **d** show distribution of m_{HH}^{KinFit} in the low-mass (LM) resonant signal region for resolved 1b1j and 2b categories respectively. Panels **b** and **e** show distribution of m_{HH}^{KinFit} in the high-mass (HM) resonant signal regions for resolved 1b1j and 2b categories respectively. **g** shows distribution of m_{HH}^{KinFit} in the resonant signal region for the boosted category. Panels **c**, **f** and **h** show distribution of m_{T2} in the non-resonant signal region for resolved 1b1j, 2b and boosted categories respectively. Data are represented by points with error bars and expected signal contributions are represented by solid (BSM HH signals) and dashed (SM non-resonant HH signal) lines. Expected background contributions (shaded histograms) and associated systematic uncertainties (dashed areas) are also shown. The background histograms are stacked.

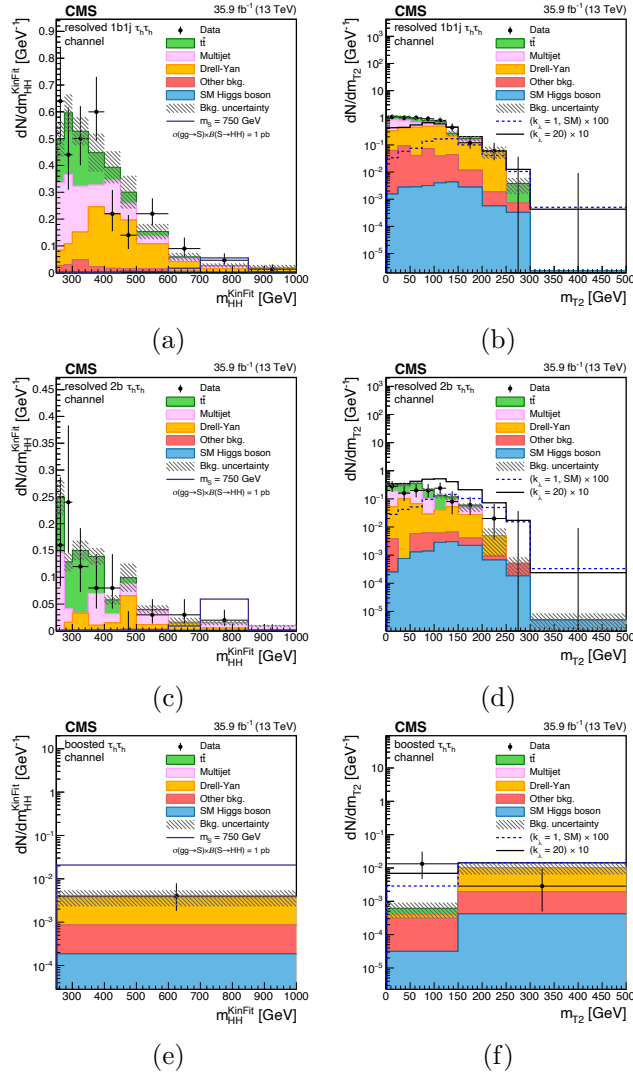


Figure 5.11: Distributions of the final discriminating variables for the $b\bar{b}\tau_h\tau_h$ final state. Panels a, c, e show distribution of m_{HH}^{KinFit} in the resonant signal region for resolved 1b1j, 2b and boosted categories respectively. Panels b, d and f show distribution of m_{T2} in the non-resonant signal region for resolved 1b1j, 2b and boosted categories respectively. Data are represented by points with error bars and expected signal contributions are represented by solid (BSM HH signals) and dashed (SM non-resonant HH signal) lines. Expected background contributions (shaded histograms) and associated systematic uncertainties (dashed areas) are also shown. The background histograms are stacked.

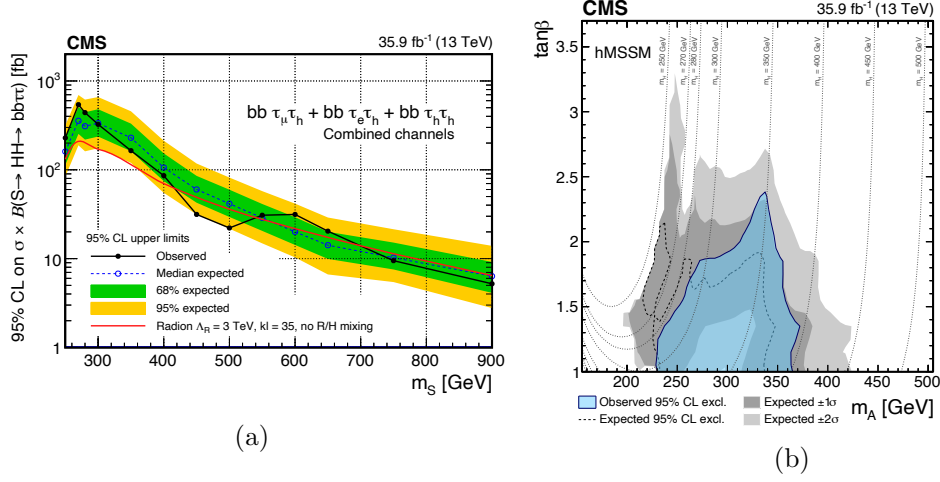


Figure 5.12: (a) 95% CL upper limits on the resonant HH production cross-section times branching fraction as a function of the resonant particle mass (m_S) [5]. The red line denotes the expectation for production of a radion. (b) Excluded regions in the $m_A - \tan\beta$ plane in the hMSSM scenario [5].

For resonant production, the 95% CL upper limit on $\sigma_{HH} \times \mathcal{B}(HH \rightarrow b\bar{b}\tau\tau)$ was set as a function of the resonant particle mass which is shown in Figure 5.12a. Figure 5.12a also shows the expected production cross-section of a radion, with mass scale, $\Lambda_R = 3$ TeV and size of extra dimensions, $kl = 35$, assuming absence of mixing with the SM Higgs boson. The radion production cross-section and branching fraction to HH are taken from [128]. Limits from Figure 5.12a were also used to interpret in the hMSSM scenario. In the hMSSM interpretation of the results of this analysis, the resonant particle is considered as the heavy CP-even Higgs state (H). The excluded regions as a function of m_A and $\tan\beta$ are shown in Figure 5.12b.

For non-resonant production, considering the theoretical uncertainties, the observed 95% CL upper limit on $\sigma_{HH} \times \mathcal{B}(HH \rightarrow b\bar{b}\tau\tau)$ is 75.4 fb (30 times the SM

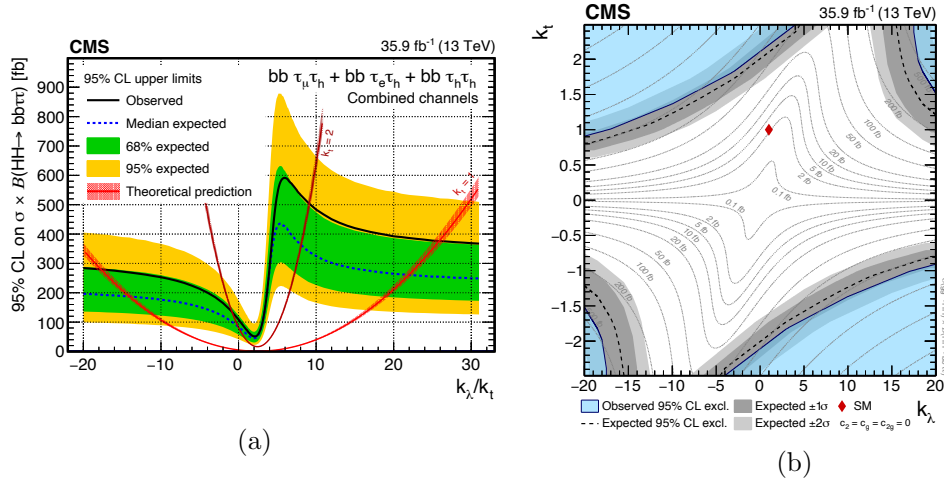


Figure 5.13: (c) 95% CL upper limits on the non-resonant HH production times branching fraction as a function of κ_λ/κ_t [5], (d) Excluded regions in the $\kappa_\lambda - \kappa_t$ plane [5].

prediction) whereas the expected 95% CL upper limit is 61.0 fb (25 times the SM prediction). Limits are also set for different hypotheses with different values of $\kappa_\lambda = \lambda_{HHH}/\lambda_{HHH}^{SM}$ and $\kappa_t = y_t/y_t^{SM}$ assuming all other BSM couplings to be zero. The signal kinematics depends on the ratio of κ_λ and κ_t and therefore, the 95% CL upper limit is set as a function of κ_λ/κ_t . The result is shown in Figure 5.13a, and the exclusion is compared to the theoretical prediction for cross-section with $\kappa_t = 1$ and 2. These upper limits are used to set constraints on κ_λ and κ_t values, as shown in Figure 5.13b, with all other couplings set to zero. The branching fractions of $H \rightarrow b\bar{b}$ and $H \rightarrow \tau\tau$ are set to be equal to the SM values.

Chapter 6

CMS Phase-2 Tracker and Level1 Tracking

The LHC is scheduled to undergo a major luminosity upgrade starting from ~ 2025 for about three years. The upgraded LHC, with a design instantaneous luminosity of $5 - 7 \times 10^{34} \text{ cm}^{-2} \text{ s}^{-1}$, will be known as the High Luminosity LHC (HL-LHC). The HL-LHC is expected to commence operation at the end of 2027, and should deliver 3 ab^{-1} of data to both ATLAS and CMS experiments in the next 10 years, which will significantly enhance the physics potential of each experiment to look for rare physics processes.

Along with the increased instantaneous luminosity, the $\langle \text{PU} \rangle$ per bunch crossing will also increase to $140 - 200$, which will pose new challenges to the experiments. Increased instantaneous luminosity and pile-up will increase the trigger rates at each experiment and induce higher radiation level, especially in the forward regions of the

detector. To work efficiently in the extremely harsh radiation environment of the HL-LHC, the experiments will have to undergo major upgrade, termed as Phase-2 upgrade. The key goals of the Phase-2 upgrade are to replace those parts of the detector which will become inefficient due to radiation damage and at the same time increase coverage and granularity of the detector taking advantage of the improved electronics.

The CMS experiment has decided to incorporate the following upgrades,

- The η coverage of the muon chambers will be increased from $|\eta| \leq 2.4$ to $|\eta| \leq 2.8$ [129].
- The endcap electromagnetic and hadron calorimeters and the pre-shower detector will be replaced by a new forward calorimeter, called the High-Granularity Calorimeter (HGCAL) [130].
- To mitigate the effect of the pileup interactions at the HL-LHC, a MIP Timing Detector (MTD) [131], with a timing precision of 30 ps , will be installed between the tracker and calorimeter.
- After the LHC Run-3, the current CMS tracker will become significantly inefficient due to radiation induced damage. Therefore, a new, improved tracker with better radiation hardness, lower material budget and higher granularity will be installed [6].

The CMS trigger system will also be upgraded in order to take advantage of the detector upgrade. Higher granularity of the sub-detectors will require larger number of readout channels. The upgraded trigger system will have the following features,

- The L1 trigger output rate is expected to increase from the current value of 100 kHz to $\sim 750\text{ kHz}$. The L1 trigger latency will increase from the current value of $3.8\ \mu\text{s}$ to $12.5\ \mu\text{s}$.
- Tracking information will be included in taking the L1 trigger decision.
- The output rate of the HLT is expected to increase from the current value of 1 kHz to 7.5 kHz .

In this chapter, the CMS Phase-2 tracker and inclusion of tracking information at the Level1 trigger, which are relevant for the studies presented in this thesis, will be discussed.

6.1 The CMS Phase-2 Tracker

The layout of the proposed CMS Phase-2 tracker is shown in Figure 6.1. The full tracker is divided in two regions, the inner tracker (IT) made of pixel detectors and the outer tracker (OT) made of pixel and strip detectors.

The inner tracker, which is placed closest to the interaction point, consists of four barrel layers, within the radial region $\sim 30\text{ mm} < r < \sim 160\text{ mm}$ and 12 discs on either side of the barrel, extending up-to $z \approx 2500\text{ mm}$ from the interaction point. The inner tracker provides a pseudorapidity coverage up-to $|\eta| < 4$. The pixel detectors provide high resolution three-dimensional hit co-ordinates which in turn provide excellent vertex measurement.

The outer tracker is made up of six barrel layers, covering a radial region $21\text{ cm} < r < 112\text{ cm}$ and five endcap discs on each side of the barrel region, covering 1200

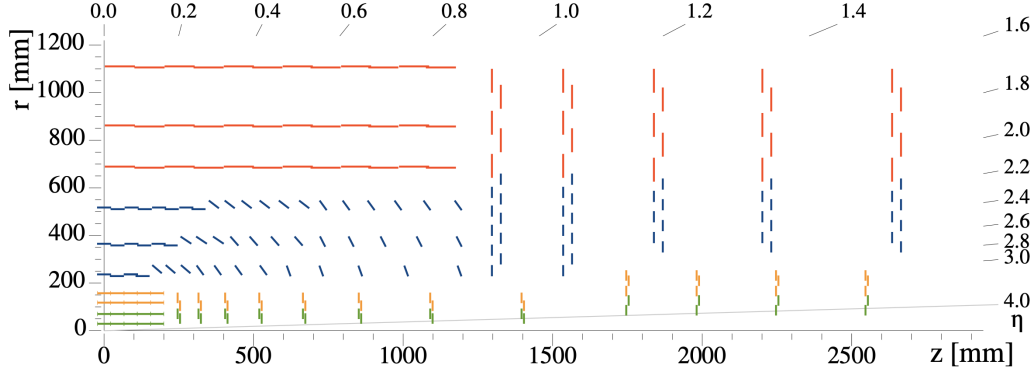


Figure 6.1: The layout of the CMS Phase-2 tracker. The inner tracker is represented by green and yellow colours, while blue and red colours represent the outer tracker.

$|z| < 2700 \text{ mm}$. The CMS Phase-2 tracker is designed in such a way that the outer tracker information can be used to reconstruct tracks at the L1 trigger. For this purpose, the outer tracker detector modules perform local data reduction in the front-end electronics, in order to limit the volume of data that has to be sent to the off-detector L1 tracking system at 40 MHz. The proposed OT modules will have two silicon sensors (top and bottom) separated by a few mm and the attached front-end electronics will have the capability to select high- p_T tracks in the presence of 3.8 Tesla magnetic field of CMS. The concept of high- p_T track selection will be discussed in section 6.2. Two types of modules have been used in the outer tracker, namely,

- **Pixel-Strip (PS) module**: built with one macro-pixel sensor and one micro-strip sensor (shown in blue in Figure 6.1).
- **Strip-Strip (2S) module**: built with two micro-strip sensors (shown in red Figure 6.1).

The actual specifications of the PS and 2S modules are shown in Table 6.1. The three inner barrel layers of the outer tracker, immediately after the inner pixel detector, will be made up of PS modules and the outermost three layers will comprise 2S modules. The endcap discs of the outer tracker will consist of both PS and 2S modules, organised radially outwards from the beam-line, as shown in Figure 6.1.

Table 6.1: Main parameters of the 2S and PS modules of the proposed CMS Phase-2 tracker [6].

2S module			PS module		
$\sim 2 \times 90 \text{ cm}^2$ active area			$\sim 2 \times 45 \text{ cm}^2$ active area		
No. of strips/sensor plane	Strip length	Pitch	No. of strips/macro-pixels	Strip/macro-pixel length	Pitch
2×1016	$\sim 5 \text{ cm}$	$90 \mu\text{m}$	$2 \times 960/32 \times 960$	$\sim 2.4 \text{ cm}/\sim 1.5 \text{ mm}$	$100 \mu\text{m}$

6.2 Concept of p_T discrimination

The concept of p_T discrimination by the modules is demonstrated in Figure 6.2. The readout electronics of a module is capable of correlating hits in the two sensors to create an entity known as *stub*. The distance between the two hits in the two sensors depends on the separation between the sensors and the p_T of the particle forming the hits. Since the low- p_T particles bend more in the magnetic field, the two hits in the two sensors will be more separated than that of a high- p_T particle, for a fixed separation between the two sensors. As shown in Figure 6.2, the stub formation succeeds if the hits (or clusters) in the two sensors fall within a programmable search window and fails otherwise. The outer tracker modules are designed to have a minimum allowed p_T threshold of 2 GeV for a stub to be accepted. The hit (or cluster)

position in the bottom sensor, i.e. the sensor facing the interaction point, will be assigned as the position of the stub.

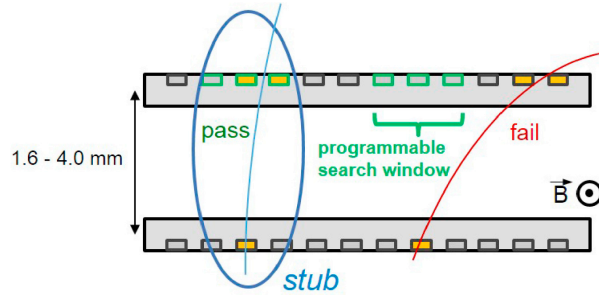


Figure 6.2: The concept of p_T discrimination.

The front-end electronics, attached to the PS and 2S modules, process analog input signals from the detector, and produce binary hit information. The front-end electronics subsequently use the hit information from adjacent channels which are connected to top and bottom sensors to form stubs.

For the PS modules, the information of the strip sensor will be read out by a chip known as the Short Strip ASIC (SSA) [132]. Similarly, the chip to read out the pixel sensor is known as the Macro Pixel ASIC (MPA) [133]. The stub finding logic will be implemented in the MPA.

Both the sensors of a 2S module will be read out by a chip called the CMS Binary Chip (CBC) [7–9]. Each CBC will have 254 channels, with 127 channels connected to the strips of the top sensor and the remaining channels connected to the strips of the bottom sensor. The stub finding logic will be implemented in the CBC.

6.3 L1 Tracking

At the L1 trigger, the stub data will be read out for each bunch crossing and the L1 track finding algorithm will perform pattern recognition to reconstruct tracks with $p_T > 2 \text{ GeV}$ by joining the stubs in different outer tracker layers. The L1 tracks are tracking primitives and will be combined with the information from the other sub-detectors to form the L1 trigger decision.

The analysis presented in this thesis uses tracks formed by a tracklet based tracking algorithm [6]. The algorithm forms track seeds or tracklets by joining a pair of stubs in adjacent layers or discs, considering a helical trajectory from the nominal interaction point. The tracklets are projected in other layers or discs. The projection is performed using both inside-out and outside-in methods. If a stub is matched in the projected layer or disc, the matched stub is included in the trajectory. A linearised χ^2 fit is performed on the stubs matched to a trajectory to obtain the final track parameters p_T , η , ϕ_0 , the longitudinal impact parameter, z_0 and optionally the transverse impact parameter, d_0 . Variables related to the quality of the track is also returned by the algorithm. The schematic diagram of the tracklet based tracking algorithm is shown in Figure 6.3. The L1 tracks will also be used for primary vertex reconstruction [6] at L1.

The tracklet based tracking algorithm is implemented in the FPGA. The Phase-2 tracker is divided in 28 sectors along the azimuthal angle, for the implementation of the tracklet algorithm. The number of sectors are chosen to contain the tracks with highest curvature, i.e. $p_T = 2 \text{ GeV}$, within at most 2 sectors. Track finding in the 28 sectors is performed in parallel by the ATCA (Advanced Telecommunication

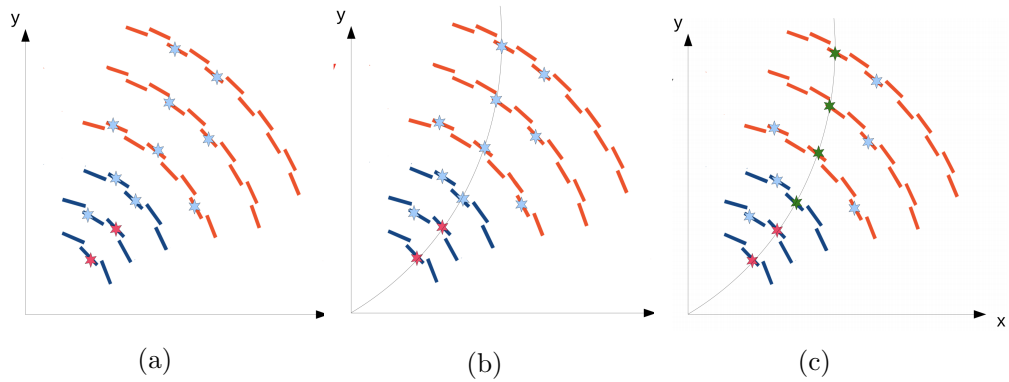


Figure 6.3: The schematic of the tracklet based tracking algorithm. A portion of the barrel outer tracker in the $x - y$ view is shown. The blue and red lines represent PS and 2S modules respectively. The light blue stars represent stubs. (a) The formed seed or tracklet is represented by red stars. (b) A helical trajectory from the nominal interaction point is formed using the tracklet and the trajectory is propagated to other layers. (c) The matched stubs to the trajectory are represented by green stars.

Computing Architecture) blades. The ATCA blades are equipped with FPGAs and each sector has one dedicated ATCA blade assigned to it. Tracklet formation is also performed within sectors. A small amount of data is duplicated in the even layers so that the tracklets can be formed locally in a sector processing unit. This also allows to avoid gaps in any area of the detector coverage.

To reduce the combinatorics during tracklet formation and also to allow additional parallel processing, each sector is further divided in small sections in z and ϕ , called “virtual modules” or “VM”s. Very few VM pairs can produce a valid tracklet and the majority of the tracklets, produced by the VM pairs, will be inconsistent with a high p_T track originating from the interaction point.

The implementation of the tracklet algorithm in the FPGA consists of the fol-

lowing steps:

- Stub organisation : The input stubs are sorted according to their layers and virtual modules.
- Tracklet formation : Stub pairs are selected to form tracklets. An initial estimation of the tracklet parameters is performed and the tracklets are projected in other layers.
- Projections : The projections of the tracklets, which are pointed towards other sectors, are transmitted. Also, the projections are routed according to the virtual modules.
- Stub matching : A matching between the stubs and the projected tracklets are performed and the difference in position between the stubs and the projected tracklets are also calculated. The information of the matching is transmitted between the sectors.
- Track fit : The track fit is performed and the initial estimation of the tracklet parameters are updated.
- Duplicate Removal : The duplicate tracks are removed.

A schematic diagram of the implementation of the tracklet algorithm is shown in Figure 6.4. The processing modules are represented by red boxes, whereas the blue boxes represent the memory where the data are stored.

The system of 28 sectors is replicated n times using a round-robin time multiplexing approach. Each time multiplexed unit is independent from each other and hence

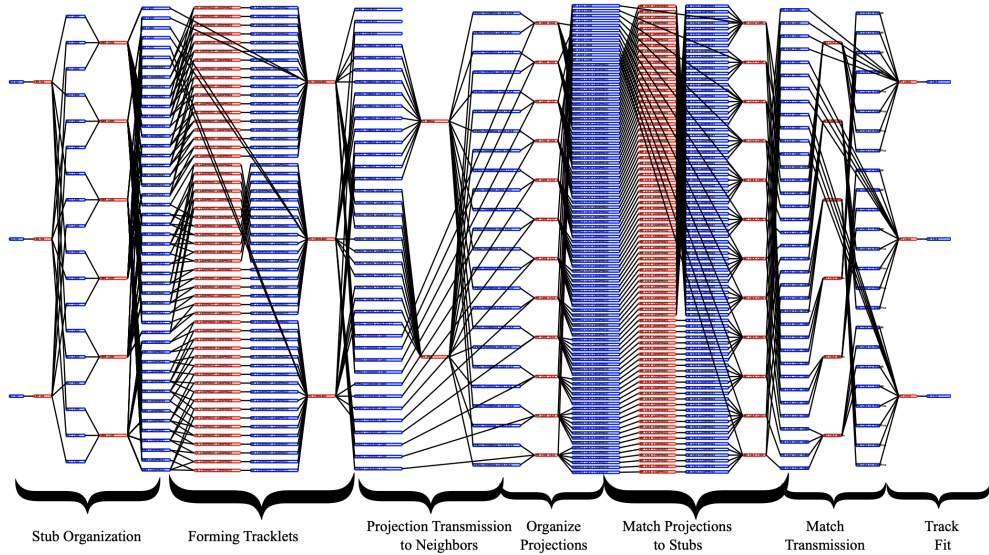


Figure 6.4: A schematic diagram of the implementation of the tracklet algorithm in the hardware [6]. The red boxes represent the processing modules and the blue boxes are the memory blocks, where the data is stored. The data flows from left to right in the figure.

each unit gets a new event to process after $n \times 25 \text{ ns}$. The choice of number of time multiplexed factor, n , is driven by a balance of cost, efficiency and needed processing power. By construction, the system operates in a fixed latency. Each step, discussed above, is performed for a fixed amount of time. If there are too many objects, some may not get processed which will lead to an algorithmic inefficiency. For the system in question, $n=4-8$ have been considered to balance the mentioned factors.

A more detailed description of the tracklet based tracking algorithm and also other methods for the Level-1 tracking can be found in reference [6].

Chapter 7

Test Beam Results for Prototype 2S modules

As described in Chapter 6, the outermost three barrel layers and the outer rings of the endcap discs (with radius above 600 *mm*), of the CMS Phase-2 outer tracker will be made of Strip-Strip (2S) modules. The front-end readout electronics attached to the modules have been designed to be able to select high- p_T tracks.

The performance of the 2S modules is estimated under realistic beam (described in section 7.3) conditions by studying the efficiency to find high p_T tracks, uniformity of the stub finding efficiency over the length of the detector module and ability of the detector modules to work efficiently upto the expected overall HL-LHC radiation level. In this chapter, test beam results for the prototype 2S modules, equipped with the second revision of the CMS Binary Chip (CBC2), will be discussed.

7.1 The CBC2

The block diagram of one of the 254 channels of the CBC2 is shown in Figure 7.1. There are three I²C registers to control the main settings of each channel of the CBC2,

- V_{CTH} : controls the comparator threshold.
- V_{PLUS} : controls the global DC baseline of the post-amplifier output.
- V_{offset} : fine tunes the baseline of the post-amplifier output for individual channels on the CBC2.

The analog signal in a CBC2 channel from a strip, goes through the amplifiers and if the amplified signal is higher than the comparator threshold (V_{CTH}), a hit is registered in that channel.

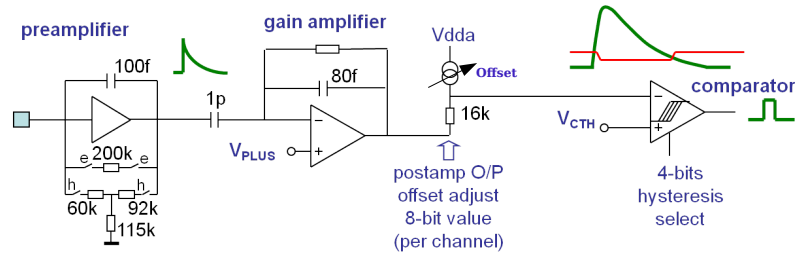


Figure 7.1: Block diagram of one of 254 channels of the CBC2 ASIC [7–9].

When a particle passes through a sensor, it deposits energy in one or more adjacent strips (channels). To get a more reliable estimate of the position of the incident particle, adjacent hits are combined to form a *cluster*. The CBC2 uses the clusters in the top and bottom sensors of a module to form stubs. In the CBC2, the central

strip number in the cluster, in integer precision, is assigned as the cluster position. The block diagram of the stub finding algorithm of the CBC2 is shown in Figure 7.2. The stub finding algorithm consists of three steps,

- Cluster-Width-Discrimination (CWD) - The number of strips inside a cluster is called the cluster width. Low p_T tracks produce clusters with large width. For stub formation, clusters with width ≤ 3 are used. In the CBC2, a global 2-bit register is used to set the maximum allowed cluster width to 1, 2 or 3 strips and wider clusters are rejected.
- offset correction and correlation - The p_T discrimination algorithm, discussed in section 6.2, is implemented in the logical block called offset correction and correlation which looks for valid clusters within a programmable window in the top sensor, for each cluster in the bottom sensor. In the CBC2, the programmable window can be set to a maximum value of ± 8 strips, around the cluster position in the bottom sensor. The shift between the clusters of the top and bottom sensors, depending on the position of the strips in $r - \phi$ plane inside the module, can be corrected with an offset correction window. The offset correction window can be set to a maximum value of ± 3 strips.
- stubs readout - The CBC2 provides a binary value about the success or failure of stub creation. A final version of the CBC chip will also be able to provide the stub position which was not yet available in CBC2.

The details of the stub finding algorithm can be found in the references [7–9].

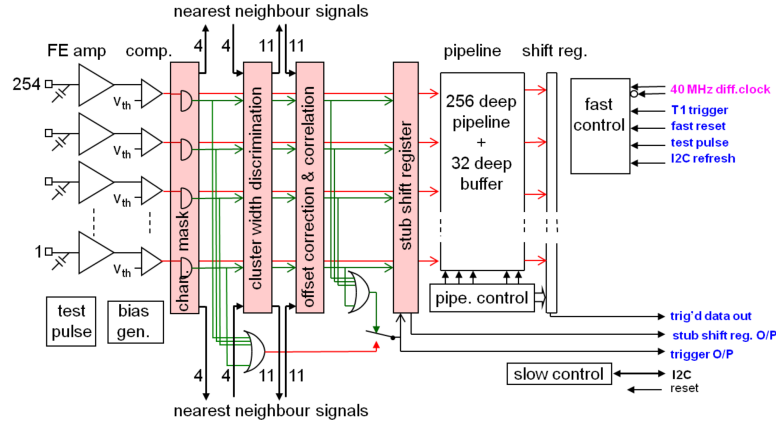


Figure 7.2: Block diagram of the CBC2 ASIC [7–9].

7.2 Prototype 2S Modules

Two prototype mini-modules and one full-sized module have been studied in the CERN test beam facility. The mini-modules have 254 strips connected to 2 CBC2s, whereas, the full-sized module has two columns of 1016 strips connected to 8 CBC2s in each column, on both sides. Each sensor of a module has n-type strips, with 5 cm length and 90 μm pitch, on $\sim 300 \mu\text{m}$ thick p-type bulk. The key parameters of the modules are shown in Table 7.1, where only the absolute values of the bias voltages are provided.

Table 7.1: Details of modules used in various test beams at CERN.

Module type	Number of CBC2s	Sensor active thickness (μm)	Sensor separation (mm)	Bias voltage (V)
Non-irradiated mini-module	2	270	2.75	250
Irradiated mini-module	2	240	3.05	600
Full-sized module	16	240	1.80	240

It is important to study whether the 2S modules will be able to operate efficiently throughout the HL-LHC period. For that purpose, one mini-module was irradiated with 23 MeV protons at the Irradiation Center Karlsruhe [134] to a fluence of $6 \times 10^{14} n_{eq}/cm^2$ with an annealing of approximately two weeks at room temperature. This is equivalent to 2 times the total amount of radiation expected in the 2S layers during the HL-LHC phase. The irradiated mini-module has an active sensor thickness of $240 \mu m$ and a sensor separation of $3.05 mm$. The irradiated mini-module is shown in Figure 7.3. The non-irradiated mini-module has an active sensor thickness of $270 \mu m$ and a separation of $2.75 mm$ between the two sensors.

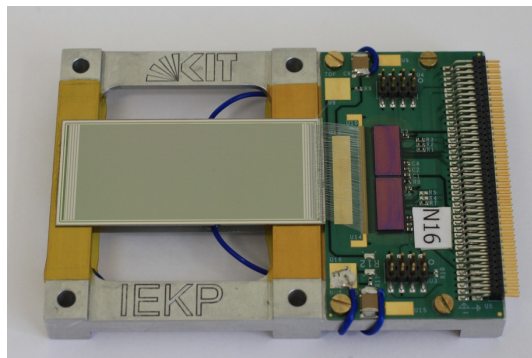


Figure 7.3: An irradiated 2S mini-module consisting of 254 strips and 2 CBC2s.

The current-voltage characteristics of the sensors of the irradiated mini-module before and after irradiation is shown in Figure 7.4. The effect of irradiation can be seen as an increase in the leakage current by three orders of magnitude.

The full-sized module has sensors with a dimension of $10 \times 10 cm^2$, an active sensor thickness of $240 \mu m$ and $1.8 mm$ separation between the two sensors. The full-sized module is shown in Figure 7.5. There are 8 CBC2s on either side of the

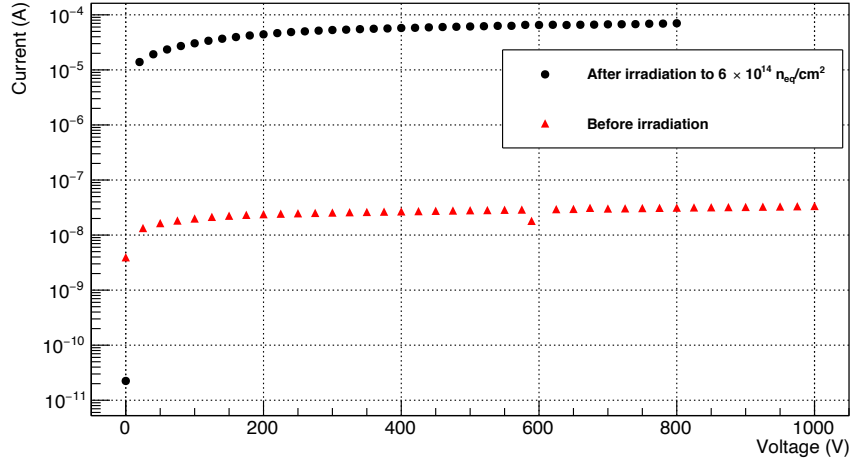


Figure 7.4: The current-voltage characteristics of a sensor of the irradiated mini-module before (red) and after (black) irradiation to $6 \times 10^{14} n_{eq}/cm^2$ which shows an increase in leakage current after irradiation. The measurements before and after irradiation were taken at $20^\circ C$ and $-20^\circ C$ respectively.

module. The rotation angle between the strips of the two sensors is kept below $400 \mu rad$. As the stub formation logic ideally assumes the strips of the two sensors to be parallel to each other, the performance will deteriorate if the angle between the two strips is higher than the tolerance of $400 \mu rad$.

7.3 Test beam setup

The schematic diagram of the test beam setup at CERN is shown in Figure 7.6. A $120 GeV$ pion beam has been used in the H2 beam line [135] in the north area with (a) 2×10^8 particles per spill, (b) 4.8s – 9.6s spill length, debunched and (c) 1 spill

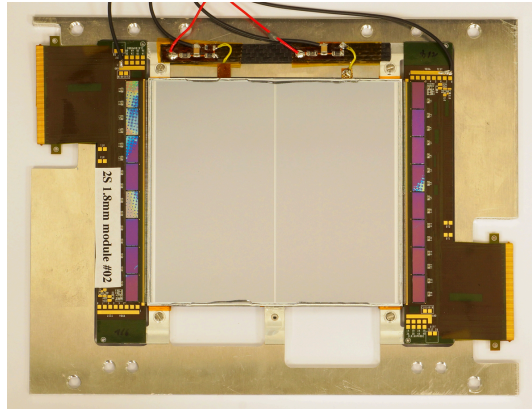


Figure 7.5: The full-sized 2S module used in the test beam.

every 14s – 48s. The direction of the beam is from left to right in the figure.

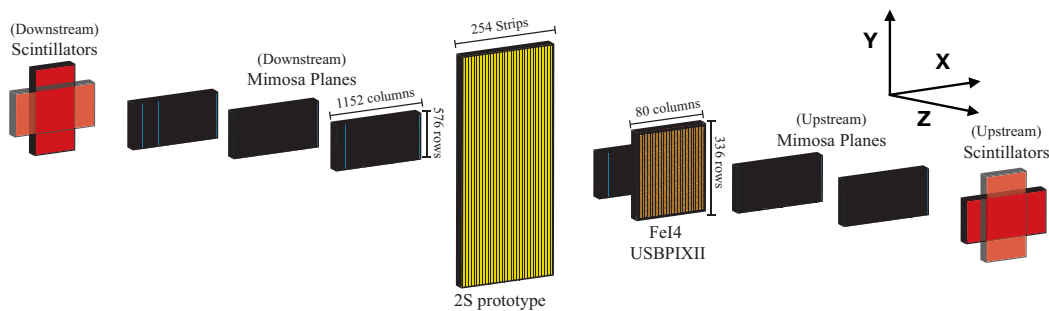


Figure 7.6: The schematic diagram of the CERN test beam setup. The four scintillators used to generate the trigger, the six MIMOSA-26 planes and the fast timing plane equipped with the FE-I4 chip are shown. The prototype detector under test (DUT) is placed within the telescope system as shown.

The test beam setup consists of,

- Trigger system: fast timing detectors are placed at the front and rear of the test beam setup to ensure that an incoming particle has traversed the full setup. A pair of crossed scintillators, with photomultiplier tubes (PMTs), is used for

trigger generation.

- Telescope system : the trajectory of the incident particle is reconstructed by a tracking detector called a telescope. The EUDET telescope [136] used in the test beam has six planes of MIMOSA-26 [137] silicon pixel sensors and a fast timing reference plane, equipped with the FE-I4 [138] chip. The active area of the MIMOSA-26 sensor planes is $10.6 \times 21.1 \text{ mm}^2$. The MIMOSA-26 planes are made up of square pixels with an area of $18.4 \times 18.4 \mu\text{m}^2$ and $50 \mu\text{m}$ thickness. The pixels are arranged in 576 rows and 1152 columns. The MIMOSA-26 planes provide a position resolution of $3.24 \mu\text{m}$. The active area of the fast-timing plane is $16.8 \times 20.0 \text{ mm}^2$. The fast-timing plane has 336 rows and 80 columns of $200 \mu\text{m}$ thick pixels. The FE-I4 chip has a timing resolution of 25 ns , which is the same as the CBC chip on the prototype 2S modules. The tracking is performed with the EU Telescope [136] software framework. At first, tracks are reconstructed using the hits on the MIMOSA-26 planes. If a hit is found in the fast timing plane, which is compatible with the track, then the timestamp of the hit is used as the timestamp of the track.
- Detector under test (DUT) : the detector unit which is being examined is placed within the telescope. The prototype 2S modules were placed in such a way that there are three MIMOSA-26 sensor planes on either side of the DUT. The performance of the DUT is studied using the track reconstructed by the telescope as reference.

7.4 Reconstruction

When a particle passes through a sensor, it deposits energy in one or more adjacent strips (channels). If the deposited energy in a channel crosses the threshold (V_{CTH}), the channel fires, which is commonly referred to as a *hit*. The CBC2 provides the position of the hits. To get a better estimate of the position of the incident particle, adjacent hits are combined to form a *cluster* and the central strip number, in integer precision, of the cluster is assigned as the cluster position. The number of strips inside a cluster is known as the cluster width. Figure 7.7a shows the cluster formation logic. As mentioned in Section 6.2, a stub is formed successfully, if the clusters in the two sensors are within a predefined matching window. The stub formation logic is shown in Figure 7.7b. The clusters of width > 3 are not considered for stub formation. The CMS binary chip is designed to correlate clusters in the two sensors of a module using an embedded logic to form stubs and provide stub position. However, the current revision of the CBC (i.e CBC2) provides the information on whether a stub formation succeeds or not. Therefore, in the test beam data analysis presented in this chapter, both clusters and stubs were reconstructed from the raw hit data.

In the analysis, an alignment is performed to correct for the possible offset between the DUT and the telescope. The alignment step performs a chi-square minimisation of the residual between the hits in the DUT and the expected impact point of the track on the DUT to constrain the degrees of freedom of the system. The

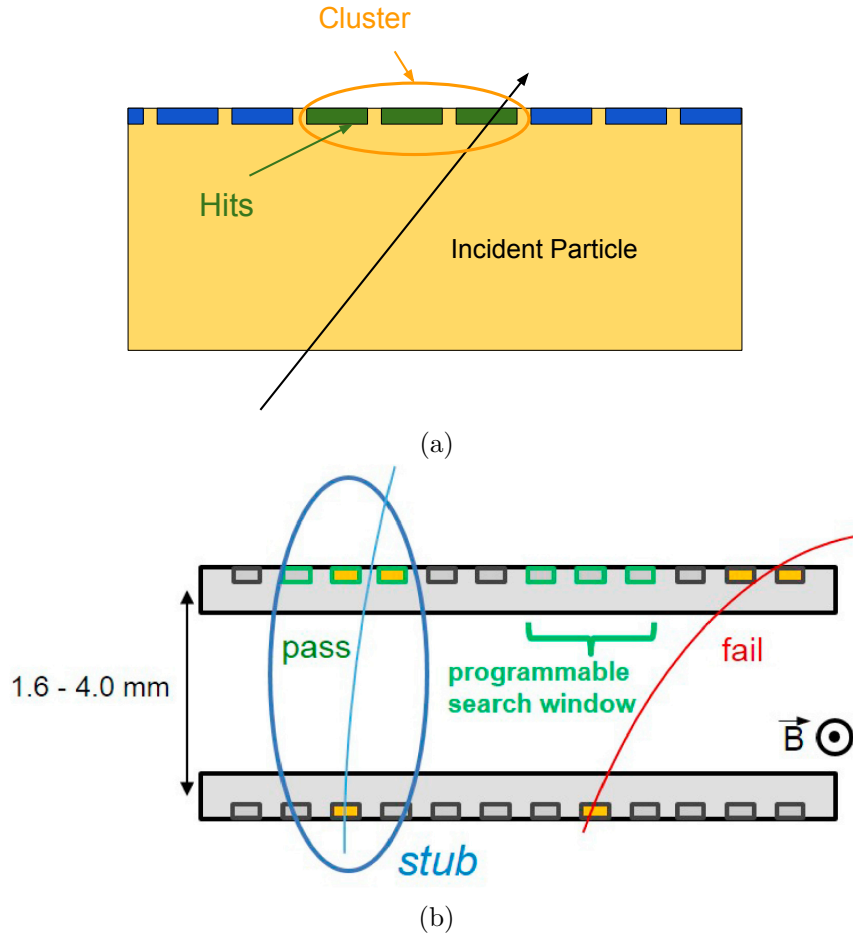


Figure 7.7: (a) Cluster formation from multiple hits in a single sensor. The big yellow rectangle represents the sensor. The strips with no hit are represented by the blue rectangles and the strips with a hit are represented by the green rectangles. Multiple adjacent hits with no gap in between are grouped together to form a cluster. (b) Stub formation from two clusters in two sensors.

chi-square is constructed in the following way,

$$\chi^2 = \frac{1}{N} \sum_{i=0}^N \left(\frac{x_{DUT}^i - x_{TkAtDUT}^i}{\sigma_{tkres}} \right)^2, \quad (7.1)$$

where

- x_{DUT} is the hit position in X, as defined in Figure 7.6
- $x_{TkAtDUT}$ is the expected impact point on the DUT, calculated by extrapolating the track from the telescope to the DUT surface facing the beam direction
- σ_{tkres} is the **average** track pointing resolution

The sum in Equation 7.1 runs over all the events with at least one cluster in each sensor of the DUT and one reconstructed track. The X and Z positions of the first plane of the DUT, rotation (θ) of the DUT around the Y-axis and the distance between the two sensors of the DUT are kept as floating parameters of the minimisation. If more than one clusters are present in any sensor, the one closest to the expected impact point of the track is considered. To remove outliers, the sum is further restricted to the events where the residual $|x_{DUT}^i - x_{TkAtDUT}^i|$ is within a $3\sigma_{tkres}$ distance from the mean value of the residual distribution.

7.5 Test beam measurements

During the test beam, for any study to be meaningful, it is crucial to establish the optimal channel threshold (V_{CTH}) of the DUT. For this reason, V_{CTH} scans are performed whenever any detector condition changes. Angular scans are also performed with the angle of rotation around the Y-axis to study cluster and stub properties as a function of the incident angle.

7.6 Results

7.6.1 Performance of mini-modules

The average number of hits per event as a function of V_{CTH} , for both top and bottom sensors of the irradiated and non-irradiated mini-modules, is shown in Figure 7.8. Similarly, the average number of clusters per event as a function of V_{CTH} is shown in Figure 7.9.

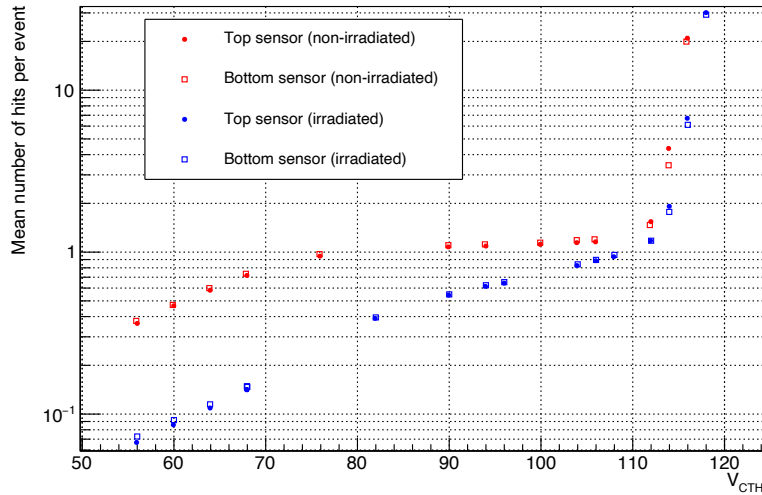


Figure 7.8: Average number of hits per event for non-irradiated and irradiated mini-modules as a function of V_{CTH} . A bias voltage of 250 V (600 V) was applied to the non-irradiated (irradiated) module.

In the test beam setup, one V_{CTH} unit corresponds to 375 electrons, as measured in the laboratory with an external X-ray source. Higher numerical values of V_{CTH} represent lower threshold in the CBC2. In both Figures 7.8 and 7.9, it can be seen

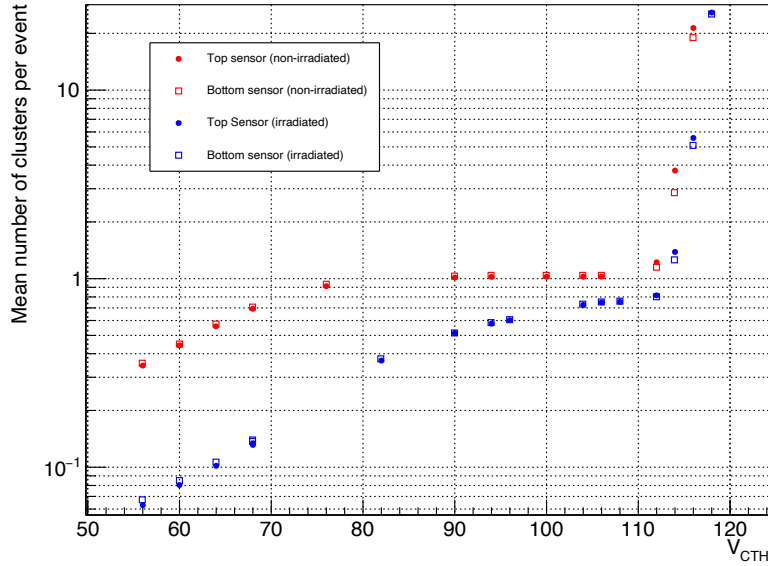


Figure 7.9: Average number of clusters per event for non-irradiated and irradiated mini-modules as a function of V_{CTH} . A bias voltage of 250 V (600 V) was applied to the non-irradiated (irradiated) module.

that at low threshold (i.e. high V_{CTH}), the number of hits or clusters are very high, as noise dominates. With increasing threshold (decreasing V_{CTH}), the number of hits or clusters decreases and reaches a plateau region dominated by signal. When the threshold is increased beyond the plateau region, the signal also gets rejected and the number of hits or clusters decreases further.

For the non-irradiated module, the average number of hits or clusters in the plateau region is 1 and for the irradiated module, the value is less than 1. The lower charge collection of the irradiated module, due to smaller sensor thickness (as shown in Table 7.1) and radiation induced effects, is the reason for lower average number

of hits or clusters compared to the non-irradiated one.

The differential cluster occupancy as a function of V_{CTH} is shown in Figure 7.10. For both the irradiated and non-irradiated modules, two peaks, for signal and noise, are visible. For the non-irradiated module, the peak in the region $V_{\text{CTH}} > 100$ DAC units, which is the low threshold region, corresponds to the noise while the peak in the region $V_{\text{CTH}} < 100$ DAC units, which is the high threshold region, corresponds to the signal. The optimal threshold to collect the signal is set to $V_{\text{CTH}} = 106$ DAC units, since noise is very low at this value. For the irradiated module, the separation between the signal and noise peak gets distorted due to radiation damage. However, the noise peak in the region $V_{\text{CTH}} > 106$ DAC units and the signal peak in the region $V_{\text{CTH}} < 106$ DAC units, are still visible. The optimal threshold is set to $V_{\text{CTH}} = 110$ DAC units for the irradiated module.

The stub efficiency is measured with respect to the tracks reconstructed by the telescope using only single-track events. The track is extrapolated to the DUT plane and the expected impact point of the track on the DUT (x_{TkAtDUT}) is obtained. The residual between the measured stub position (x_{DUT}) and x_{TkAtDUT} is calculated and if the value is within 4σ of the residual distribution, the stub is considered to be matched with the track. The stub efficiency is calculated from the events where a track is matched to a stub with respect to the total number of single-track events considered.

An angular scan is performed to emulate the effect of particle p_T in the absence of the magnetic field. The effective p_T of a particle, traversing through the module

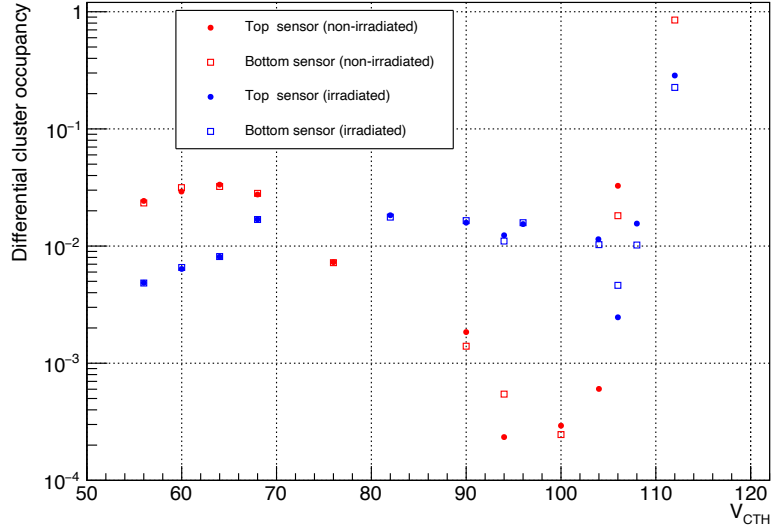


Figure 7.10: Differential cluster occupancy for non-irradiated and irradiated mini-modules as a function of V_{CTH} . A bias voltage of 250 V (600 V) was applied to the non-irradiated (irradiated) module.

inside a magnetic field of 3.8 Tesla, can be estimated with the following formula,

$$p_T [\text{GeV}] \approx \frac{0.57 \cdot R [\text{m}]}{\sin(\alpha)} \quad (7.2)$$

where R is the radial distance of the module from the centre of the CMS detector and α is the incident angle of the particle on the DUT plane. The test beam setup aimed to keep multiple scattering at the minimum. The effective p_T is estimated from the measurement of the angle. In this test beam, the angle measurement was not very accurate which resulted in a less precise estimate of the effective p_T . The stub efficiency for the two mini-modules as a function of the effective p_T as well as

beam incident angle is shown in Figure 7.11, where the effective p_T was calculated using $R = 60 \text{ cm}$. For low p_T (high incident angle), the relative shift in cluster positions in two sensors of the module is large and hence there is a lower probability of correlating the two clusters to form a stub. Hence, the stub efficiency at low p_T (high incident angle) is small. In Figure 7.11, a stub correlation window of 5 strips has been used. The different sensor spacing of the two mini-modules results in different turn-on curves.

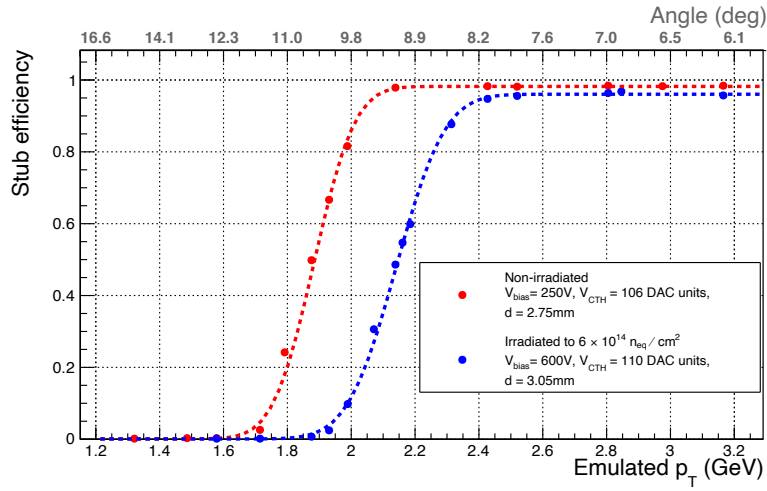


Figure 7.11: Stub efficiency for the irradiated (blue) and non-irradiated (red) mini-modules as a function of the incident angle (top x-axis) or the effective p_T (bottom x-axis). As expected, for large angle of incidence, which corresponds to low effective p_T , the stub efficiency drops. A radius of 60 cm is used to calculate p_T . The stub correlation window is set to 5 strips.

The turn-on curves of Figure 7.11 are fitted with an error function of the form,

$$f(p_T) = 0.5A \left(1 + \operatorname{erf} \left(\frac{p_T - p_{T\mu}}{\sigma_{p_T}} \right) \right), \quad (7.3)$$

where,

- A is the efficiency at the plateau
- $p_{T\mu}$ is the turn-on threshold for which the efficiency is 50%
- σ_{p_T} is the width of the Gaussian in the error function

The relative p_T resolution can be obtained from the ratio of the absolute resolution σ_{p_T} and $p_{T\mu}$.

For the non-irradiated module, the turn-on threshold is 1.88 GeV and p_T resolution is 5%. The stub efficiency at the plateau is 99%. From the high plateau efficiency and sharp turn-on, it can be concluded that the non-irradiated module will be able to select stubs with $p_T > 2 GeV$ efficiently.

For the irradiated module, the stub efficiency at the plateau is 97% and the p_T resolution is 6%. From the results, it can be concluded that the stub finding logic of the 2S modules will work with high efficiency throughout the lifetime of the HL-LHC.

For the irradiated module, three different angular scans were performed with three different stub correlation windows. The stub efficiency as a function of the effective p_T for the three stub correlation windows is shown in Figure 7.12. From the figure, it can be seen that the turn-on depends on the correlation window but the efficiency value at the plateau does not.

7.6.2 Performance of the full-sized module

For the full-sized 2S module, the primary goal was to check the uniformity of response over the dimension of the module. The stub efficiency per strip for the full-sized 2S

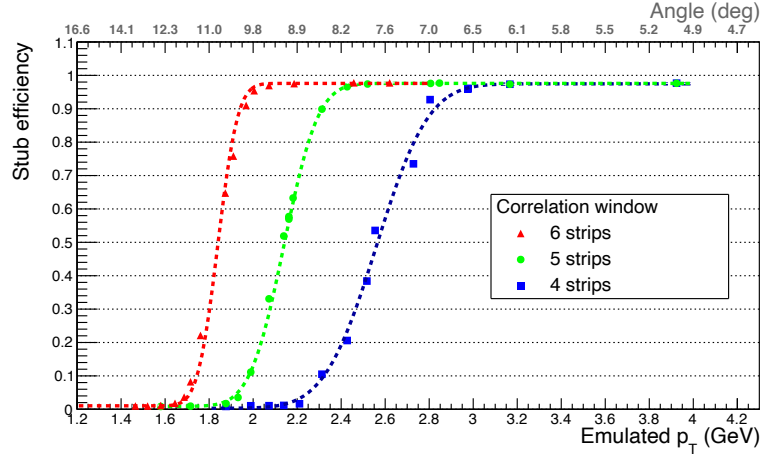
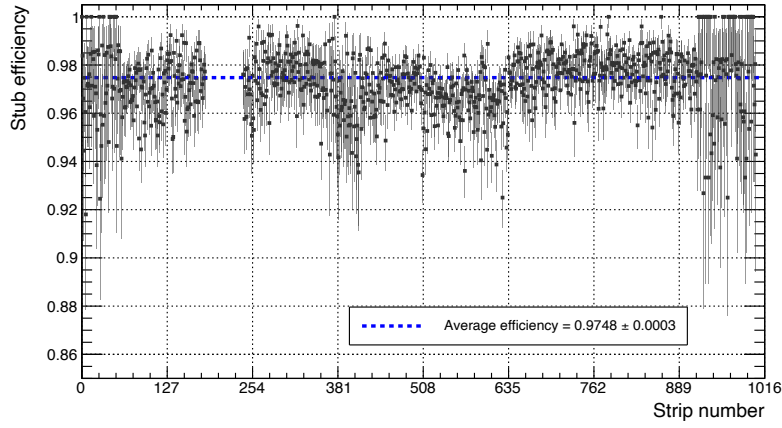
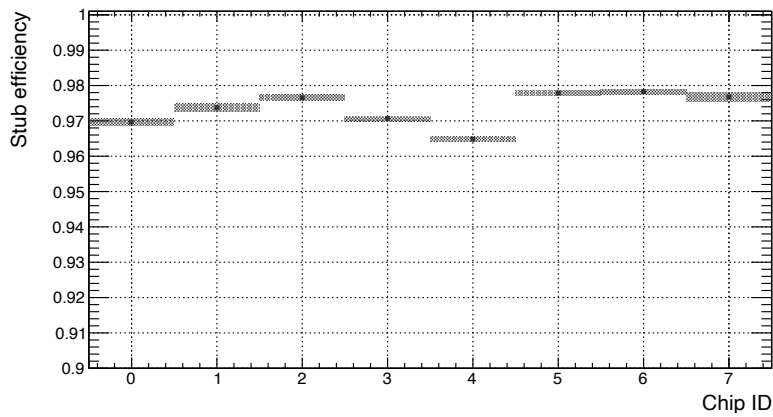


Figure 7.12: Comparison of stub efficiency for different angular scans with different correlation windows for the irradiated mini-module. The incident angle is shown in top x-axis and the effective p_T is shown in bottom x-axis. The choice of window size leads to a shift in the turn-on p_T , but the efficiency at the plateau remains the same. A bias voltage of 600 V was applied to the irradiated mini-module.

module is shown in Figure 7.13a. The module was operated at a bias voltage of 250 V and the V_{CTH} was set to 115 DAC units. The operating points are derived with a similar way, as of the mini-modules. The region between strips 185 and 239 was not scanned by the beam and therefore, no data are available from that region. The large statistical uncertainty in efficiency, seen at the module edges, is due to the limited amount of data obtained from the scans performed at the module edges. From Figure 7.13a, it can be seen that the stub efficiency is 94–98% for most of the detector region. The mean stub efficiency, obtained by performing a linear fit, using asymmetric errors on each measurement, is 97.4% and the strip-to-strip variation of the stub efficiency is 1.3%. The stub efficiency per CBC is shown in Figure 7.13b.



(a)



(b)

Figure 7.13: Stub efficiency of a full-sized 2S module. The module was operated at a bias voltage of 250 V and the V_{CTH} value was set to 115 DAC units. (a) Stub efficiency per strip and (b) stub efficiency per CBC computed using data from strips scanned by the beam.

7.7 Conclusions

From the results presented in this chapter, it can be seen that the 2S modules will be able to select tracks with $p_T > 2 \text{ GeV}$ with high efficiency, which is the main design goal of these modules. The stub efficiency over the full detector dimension of the full-sized 2S module is 94–98%. The performance of the irradiated mini-module also demonstrates that the 2S modules will be able to work efficiently even after the radiation damage equivalent to the full HL-LHC running period.

Chapter 8

Trigger level study of $B_s^0 \rightarrow \phi\phi \rightarrow 4$ Kaons using L1 Tracks for HL-LHC

Triggering on rare, low- p_T , fully hadronic final states, e.g. $B_s^0 \rightarrow \phi\phi \rightarrow 4$ Kaons is not possible with the current CMS detector due to the lack of a proper trigger. Inclusion of tracking information in the L1 trigger decision during Phase-2, as discussed in chapter 6, will enable CMS for the first time to trigger on such final states by reconstructing the ϕ candidates from the L1 tracks and subsequently the B_s^0 candidates. In this chapter, the capability of CMS to trigger on the $B_s^0 \rightarrow \phi\phi \rightarrow 4$ Kaons process will be discussed. The main goal of the study is to optimise the signal efficiency and additional trigger rate that will be introduced in order to include the $B_s^0 \rightarrow \phi\phi \rightarrow 4$ Kaons final state in the CMS L1 trigger menu for HL-LHC.

8.1 Dataset

This analysis is primarily based on tracks reconstructed at L1. The signal and background datasets used in the analysis are listed below,

- Signal
 - $pp \rightarrow B_s^0 \bar{B}_s^0$ events are produced with Pythia8 [84].
 - Decays of B_s^0 and \bar{B}_s^0 have been simulated with EvtGen [139].
 - Appropriate filters have been used at the generation step to select only those events where the B_s^0 decays exclusively to a ϕ pair with at least one ϕ subsequently decaying to $K^+ K^-$, with both kaons having $p_T(K) > 1.9 \text{ GeV}$. Figure 8.1 shows the true p_T distribution of the softest kaon in the generated events at this stage.

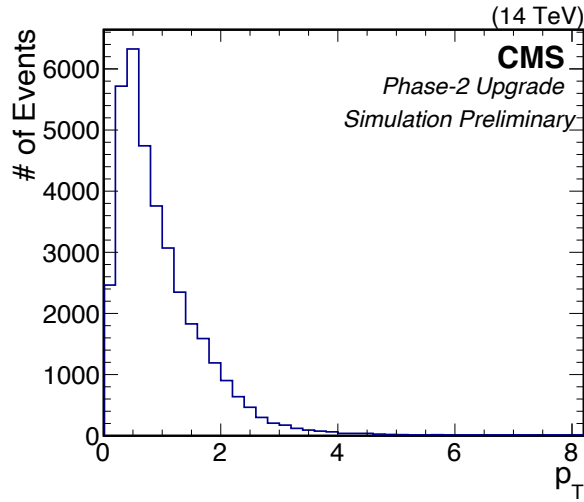


Figure 8.1: True p_T of the softest kaon in generated $B_s^0 \rightarrow \phi\phi \rightarrow 4 \text{ Kaons}$ events.

- The generated events are passed through the Geant4 based CMS Phase-2 detector simulation, digitisation and L1 trigger simulation including L1 tracking (discussed in chapter 6).
 - Signal event datasets with $\langle \text{PU} \rangle = 140$ and 200 were used for the study, with ~ 30 K events for each pileup scenario.
 - At the analysis level, signal events, where all the four kaons originating from $B_s^0 \rightarrow \phi\phi$ have $p_T(K) \geq 2 \text{ GeV}$, are considered as the denominator to calculate signal efficiency. It should be noted that the signal efficiency is slightly underestimated, as at the generator level acceptance or η cut was not applied on the kaons.
- Background
 - Single Neutrino gun events, with $\langle \text{PU} \rangle = 140$ and 200 have been used, with ~ 500 K events for each pileup scenario.

A similar analysis is also performed with tracks reconstructed at the physics (or offline) level to ensure that, once an event is triggered, there is no further loss of efficiency.

8.2 Event Selection

The analysis strategy is kept simple because the final goal is to implement the algorithm on the L1 trigger hardware.

8.2.1 Track Selection

In the analysis, only tracks with $p_T \geq 2 \text{ GeV}$ (minimum p_T threshold possible in the tracker design), and $|\eta| \leq 2.5$ (geometrical coverage of the Phase-2 outer tracker), have been considered.

8.2.2 Reconstruction of ϕ candidates

In the first pass, ϕ candidates are formed. All the selected tracks in an event are considered to be kaons. A pair of tracks, which satisfies the following conditions, is considered as a ϕ candidate:

- Tracks have opposite charges.
- Tracks are required to originate from the same vertex. To check the vertex compatibility of the tracks, d_z and d_{xy} , defined as the distance between two tracks along the beam axis (z), and in the plane perpendicular to the beam axis (xy) respectively, are used. Figure 8.2a shows the distribution of d_z between all the oppositely charged track pairs. Figure 8.2b shows the distribution of d_{xy} between all the track pairs with opposite charges and $|d_z| \leq 1 \text{ cm}$.
- Finally, the invariant mass of the two tracks should be compatible with the true ϕ mass, i.e the invariant mass should lie within 0.99 and 1.04 GeV . The invariant mass distribution of all the track pairs, with opposite charges, $|d_z| \leq 1 \text{ cm}$ and $d_{xy} \leq 1 \text{ cm}$, is shown in Figure 8.3.

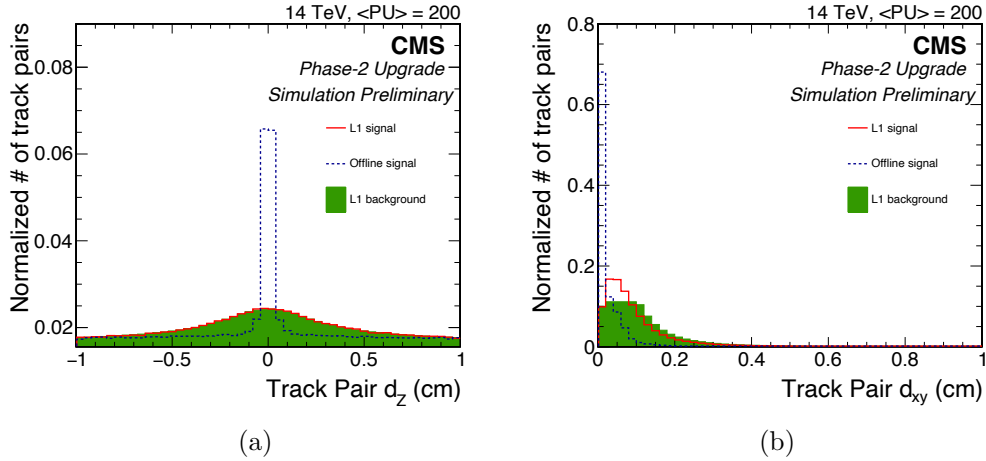


Figure 8.2: (a) d_z between all the oppositely charged track pairs, (b) d_{xy} between all the track pairs having opposite charges and $|d_z| \leq 1 \text{ cm}$ for $\langle \text{PU} \rangle = 200$. The distributions are normalised to unit area. The dashed blue and solid red histograms correspond to the Offline and L1 signal events respectively, while the green filled area represents the background events.

8.2.3 Reconstruction of B_s^0 candidates

In the subsequent pass, reconstructed ϕ candidates are combined pair-wise to form B_s^0 candidates with the following algorithm,

- ϕ pairs are required to come from the same vertex, which is ensured by checking the vertex compatibility of the four tracks. For each ϕ candidate a vertex position is assigned, which is equal to the average of the vertex positions of the two tracks which form the ϕ candidate. Vertex compatibility of a ϕ pair is checked using d_z and d_{xy} between the two ϕ candidates.
- The angular separation in the $\eta - \phi$ plane (ΔR) between the two ϕ candidates should be $0.2 \leq \Delta R(\phi\text{-pair}) \leq 1$. Figure 8.4a shows the distribution of $\Delta R(\phi\text{-pair})$.

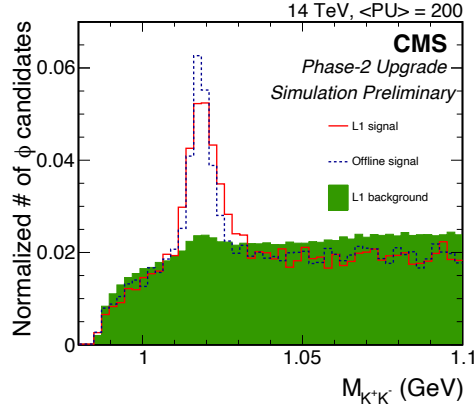


Figure 8.3: Invariant mass distribution of all the tracks pairs, having opposite charges, $|d_z| \leq 1 \text{ cm}$ and $d_{xy} \leq 1 \text{ cm}$ for $\langle \text{PU} \rangle = 200$. The distributions are normalised to unit area. The dashed blue and solid red histograms correspond to the Offline and L1 signal events respectively while the green filled area represents the background events.

pair) between all the ϕ pairs, with $|d_z|(\phi\text{-pair}) \leq 1 \text{ cm}$ and $d_{xy}(\phi\text{-pair}) \leq 1 \text{ cm}$, for $\langle \text{PU} \rangle = 200$.

- The ΔR separation between the two tracks forming a ϕ candidate should be $\Delta R(K^+K^-) \leq 0.12$. Figure 8.4b shows the $\Delta R(K^+K^-)$ distribution between the tracks of the ϕ candidates, which form ϕ pairs with $|d_z|(\phi\text{-pair}) \leq 1 \text{ cm}$, $d_{xy}(\phi\text{-pair}) \leq 1 \text{ cm}$ and $0.2 \leq \Delta R(\phi\text{-pair}) \leq 1$, for $\langle \text{PU} \rangle = 200$.
- The invariant mass of the ϕ pair should be compatible with the true B_s^0 mass. Figure 8.5 shows the distribution of the invariant mass of the ϕ pairs, with $|d_z|(\phi\text{-pair}) \leq 1 \text{ cm}$, $d_{xy}(\phi\text{-pair}) \leq 1 \text{ cm}$, $0.2 \leq \Delta R(\phi\text{-pair}) \leq 1.0$ and $\Delta R(K^+K^-) \leq 0.12$, for $\langle \text{PU} \rangle = 200$.

Events, where at least one B_s^0 candidate is found, are selected. If more than one

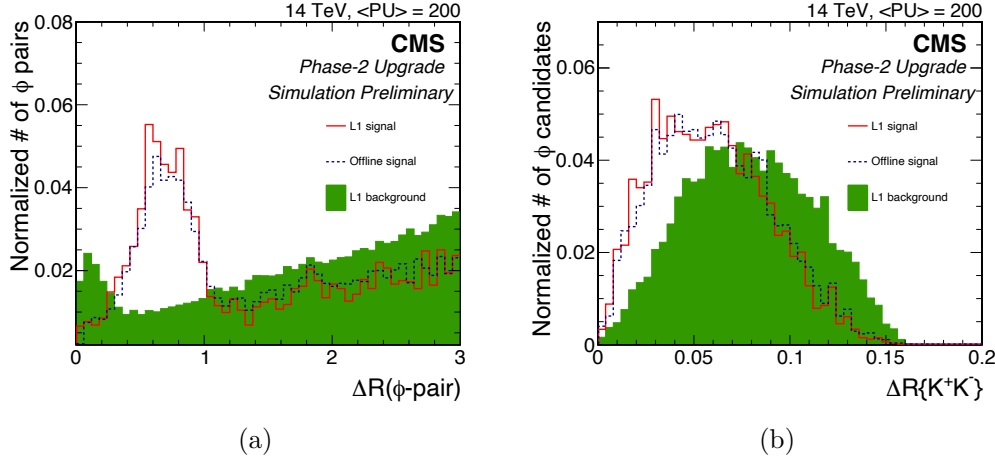


Figure 8.4: (a) $\Delta R(\phi\text{-pair})$ distribution for all the ϕ -pairs, with $|d_z|(\phi\text{-pair}) \leq 1$ cm and $d_{xy}(\phi\text{-pair}) \leq 1$ cm, (b) $\Delta R(K^+K^-)$ distribution of the ϕ candidates, which form ϕ pairs with $|d_z|(\phi\text{-pair}) \leq 1$ cm, $d_{xy}(\phi\text{-pair}) \leq 1$ cm and $0.2 \leq \Delta R(\phi\text{-pair}) \leq 1$, for $\langle \text{PU} \rangle = 200$. The distributions are normalised to unit area. The dashed blue and solid red histograms correspond to the Offline and L1 signal events respectively, while the green filled area represents the background events.

B_s^0 candidates are found in an event, the one having the mass closest to the true B_s^0 mass is selected as the B_s^0 candidate in the event for further analysis. For the signal events, a geometrical matching between the selected B_s^0 candidate and generator level B_s^0 candidate is performed. Signal efficiency is calculated with events, where the selected B_s^0 candidate matches with the generated one, as numerator and events, which pass the analysis level generator filter mentioned in section 8.1, as denominator.

In each bunch crossing at the LHC, even if there is no hard collision, a large number of minimum bias collisions always take place, which depend on the instantaneous luminosity. Therefore, it is meaningful to measure the L1 trigger rate using the minimum bias collision events. In this analysis, two different background datasets,

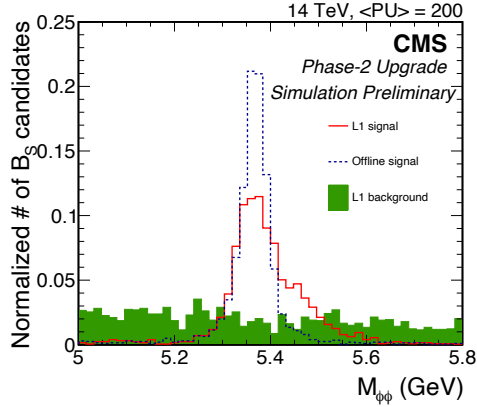


Figure 8.5: Invariant mass distribution of all the ϕ -pairs, with $|d_z| \leq 1$ cm, $d_{xy} \leq 1$ cm, $0.2 \leq \Delta R(\phi\text{-pair}) \leq 1.0$ and $\Delta R(K^+K^-) \leq 0.12$, for $\langle \text{PU} \rangle = 200$. The distributions are normalised to unit area. The dashed blue and solid red histograms correspond to the Offline and L1 signal events respectively, while the green filled area represents the background events.

one with 140 minimum bias collisions per bunch crossing (i.e $\langle \text{PU} \rangle = 140$) and the other with 200 minimum bias collisions per bunch crossing (i.e $\langle \text{PU} \rangle = 200$), have been used. With the expected collision rate of HL-LHC as 30 MHz, the L1 trigger rate is defined as, background efficiency \times 30000 kHz.

Three selection working points, namely loose, medium and tight, have been chosen to have three different representative values of the event rate at the L1 trigger level. Table 8.1 lists the optimised cut values for the three working points.

8.3 Results

The signal efficiency measured at the L1 trigger and Offline levels and the corresponding L1 trigger rate are shown in Table 8.2 for $\langle \text{PU} \rangle = 140$ and in Table 8.3

Table 8.1: Baseline event selection conditions.

Working point	loose	medium	tight
Tracks	$p_T \geq 2 \text{ GeV}, \eta \leq 2.5$		
Track pair	$d_{xy} \leq 1 \text{ cm}, d_z \leq 1 \text{ cm}$	$d_{xy} \leq 0.5 \text{ cm}, d_z \leq 0.3 \text{ cm}$	
ϕ -pair	$d_{xy} \leq 1 \text{ cm}, d_z \leq 1 \text{ cm}$	$d_{xy} \leq 0.5 \text{ cm}, d_z \leq 1 \text{ cm}$	
ϕ -pair	$0.2 \leq \Delta R(\phi_1, \phi_2) \leq 1, \Delta R(K^+, K^-) \leq 0.12$		
ϕ mass (GeV)	$0.99 \leq M_{K^+K^-} \leq 1.04$	$1.0 \leq M_{K^+K^-} \leq 1.03$	
B_s^0 mass (GeV)	$5.27 \leq M_{\phi\phi} \leq 5.49$	$5.29 \leq M_{\phi\phi} \leq 5.48$	

for $\langle \text{PU} \rangle = 200$. The pile-up dependence of the trigger rate is shown in Figure 8.6, where the efficiency values are used for $\langle \text{PU} \rangle = 140$. As can be seen from the tables and the graph, for $\langle \text{PU} \rangle = 200$, a rate of ~ 15 kHz must be added to the overall L1 bandwidth for a signal efficiency of $\sim 30\%$ with the medium working point. The L1 trigger rate for the loose working point is 37.9 ± 1.5 kHz for $\langle \text{PU} \rangle = 200$ which is too high, while for the tight working point, the L1 signal efficiency is only $17.6 \pm 0.8\%$ for $\langle \text{PU} \rangle = 200$. Tables 8.2 and 8.3 also list offline efficiency for all the working points.

Table 8.2: Signal efficiency and trigger rate for loose, medium and tight working points respectively for $\langle \text{PU} \rangle = 140$. Uncertainties are statistical only.

Baseline	Efficiency (%)		Rate (kHz)
	L1	Offline	
Loose	34.0 ± 1.2	58.26 ± 1.7	18.0 ± 1.0
Medium	28.4 ± 1.1	51.8 ± 1.6	7.7 ± 0.7
Tight	19.6 ± 0.8	51.7 ± 1.6	2.9 ± 0.4

The p_T distributions of the four kaon tracks, which constitute the selected B_s^0 candidate in an event, are shown in Figure 8.7, for medium baseline and $\langle \text{PU} \rangle = 200$.

Table 8.3: Signal efficiency and trigger rate for loose, medium and tight working points respectively for $\langle \text{PU} \rangle = 200$. Uncertainties are statistical only.

Baseline	Efficiency (%)		Rate (kHz)
	L1	Offline	
Loose	32.2 ± 1.2	57.7 ± 1.7	37.9 ± 1.5
Medium	27.5 ± 1.1	51.9 ± 1.6	13.7 ± 0.9
Tight	17.6 ± 0.8	51.9 ± 1.6	4.7 ± 0.5

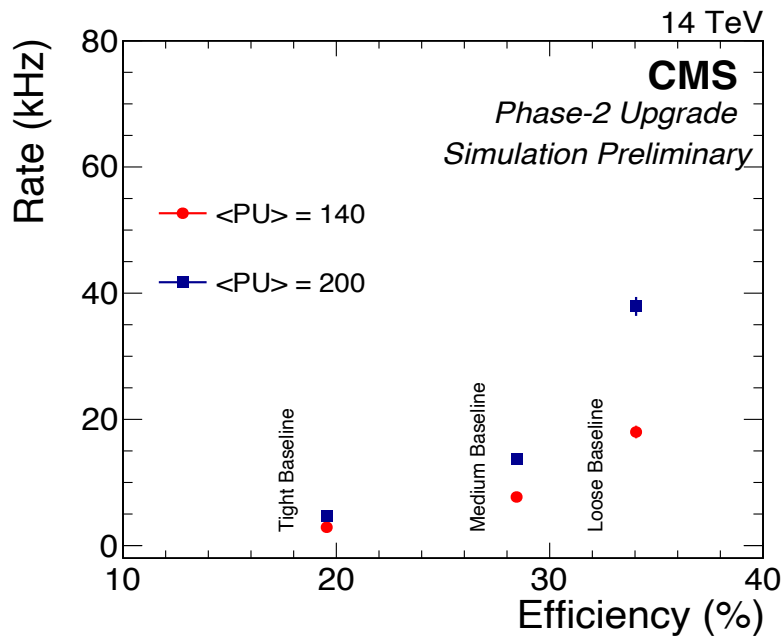


Figure 8.6: Signal efficiency and trigger rate for different selection baselines and for different pileup scenarios. Uncertainties are statistical only.

The effect of the p_T threshold on efficiency is clearly visible on the p_T distribution of the lowest p_T track.

Figure 8.8 shows the number of ϕ candidates in an event, whereas Figure 8.9 shows the transverse momentum of the two ϕ candidates which form the selected B_s^0

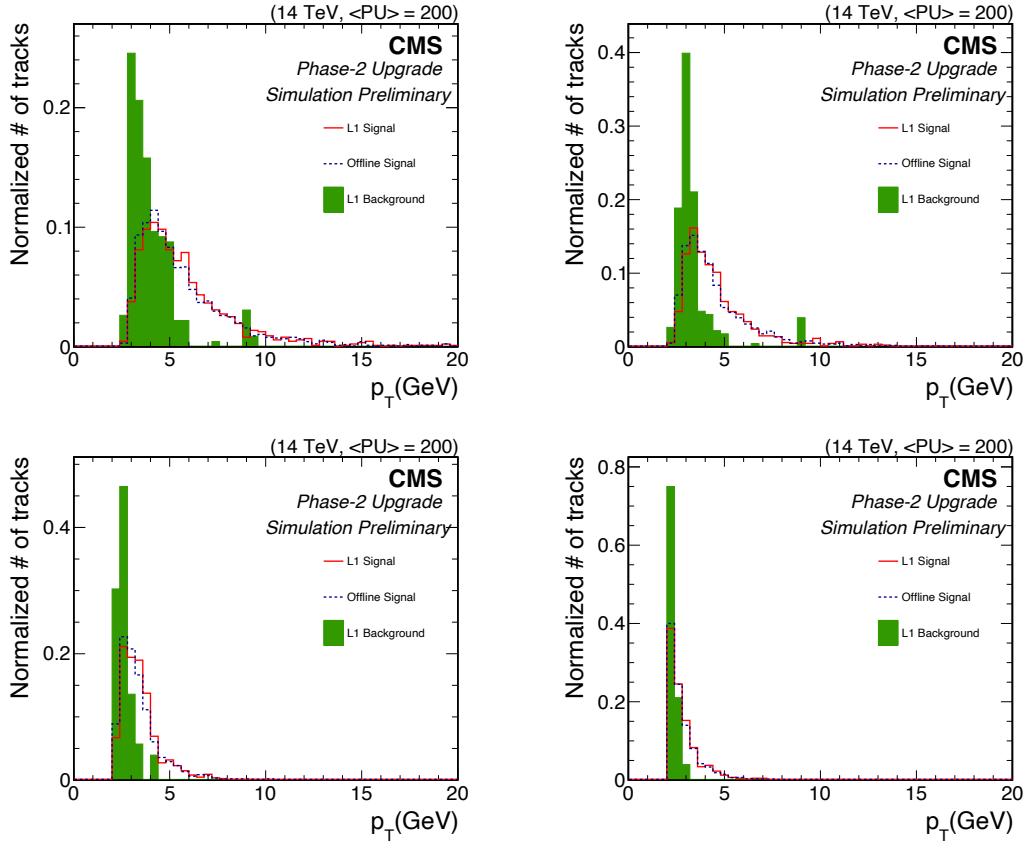


Figure 8.7: p_T of the four (kaon) tracks that from the selected B_s^0 candidates, ordered in terms of descending p_T for $\langle \text{PU} \rangle = 200$. The events are selected with the medium baseline. The distributions are normalised to unit area. The dashed blue and solid red histograms correspond to the Offline and L1 signal events respectively, while the green filled area represents the background events.

candidate. No further optimisation could be achieved with these variables.

The p_T of the selected B_s^0 candidate is shown in Figure 8.10 for medium baseline and $\langle \text{PU} \rangle = 200$.

To study the effect of the $|d_z|$ cut between any track pair on signal efficiency and

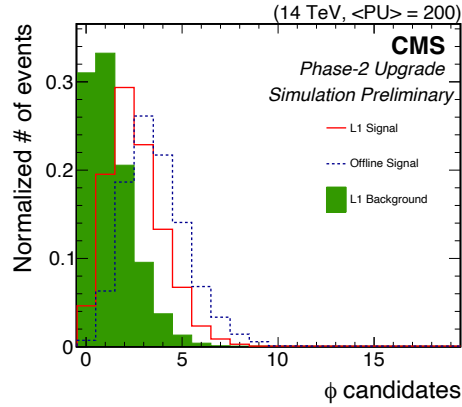


Figure 8.8: Number of ϕ candidates reconstructed in an event, for medium baseline and $\langle\text{PU}\rangle = 200$. The distributions are normalised to unit area. The dashed blue and solid red histograms correspond to the Offline and L1 signal events respectively, while the green filled area represents the background events.

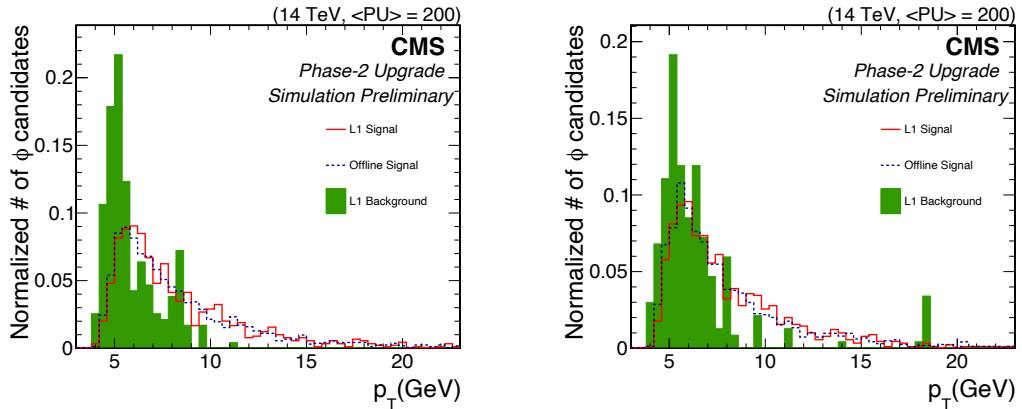


Figure 8.9: Transverse momentum of the two reconstructed ϕ candidates which form the selected B_s^0 candidate, for medium baseline and $\langle\text{PU}\rangle = 200$. The distributions are normalised to unit area. The dashed blue and solid red histograms correspond to the Offline and L1 signal events respectively, while the green filled area represents the background events.

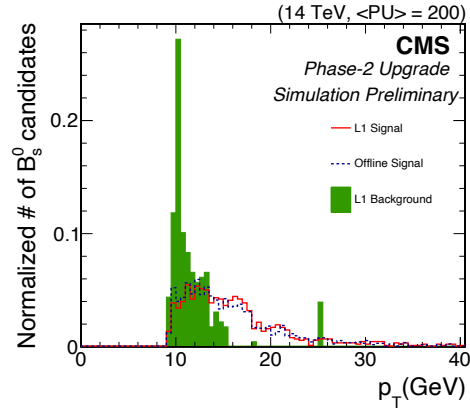


Figure 8.10: Transverse momentum of the selected B_s^0 candidate, for medium baseline and $\langle\text{PU}\rangle = 200$. The distributions are normalised to unit area. The dashed blue and solid red histograms correspond to the Offline and L1 signal events respectively, while the green filled area represents the background events.

trigger rate, the quantities are estimated by varying the $|d_z|$ cut in the range 0.3 – 1.0 cm . The results are shown in Tables 8.4 and 8.5 for the medium baseline and $\langle\text{PU}\rangle = 200$ and 140 respectively. For this study d_{xy} was set to 0.5 cm for both track and ϕ pairs.

Table 8.4: Signal efficiency and trigger rate as a function of the $|d_z|$ cut between the pair of tracks, for $\langle\text{PU}\rangle = 200$. Uncertainties are statistical only.

$ d_z $ (cm)	Efficiency (%)	Rate (kHz)
1.0	27.5 ± 1.1	13.6 ± 0.9
0.9	27.2 ± 1.0	12.0 ± 0.9
0.8	26.8 ± 1.0	10.0 ± 0.8
0.7	26.0 ± 1.0	9.0 ± 0.7
0.6	25.3 ± 1.0	7.6 ± 0.7
0.5	23.9 ± 1.0	6.7 ± 0.6
0.4	21.5 ± 0.9	5.9 ± 0.6
0.3	17.6 ± 0.8	4.8 ± 0.5

Table 8.5: Signal efficiency and trigger rate as a function of the $|d_z|$ cut between the pair of tracks, for $\langle \text{PU} \rangle = 140$. Uncertainties are statistical only.

$ d_z $ (cm)	Efficiency (%)	Rate (kHz)
1.0	28.4 ± 1.1	7.8 ± 0.7
0.9	28.0 ± 1.0	7.3 ± 0.7
0.8	27.6 ± 1.0	6.1 ± 0.7
0.7	27.0 ± 1.0	5.2 ± 0.6
0.6	26.1 ± 1.0	5.1 ± 0.6
0.5	25.1 ± 1.0	4.8 ± 0.6
0.4	23.1 ± 0.9	4.0 ± 0.5
0.3	19.6 ± 0.8	3.2 ± 0.5
0.2	13.5 ± 0.7	1.8 ± 0.4
0.1	4.7 ± 0.4	1.0 ± 0.3

The results presented in Table 8.4 have also been shown as a ROC curve for signal efficiency vs trigger rate in Figure 8.11. The results obtained with $\langle \text{PU} \rangle = 140$ are also shown in the same figure.

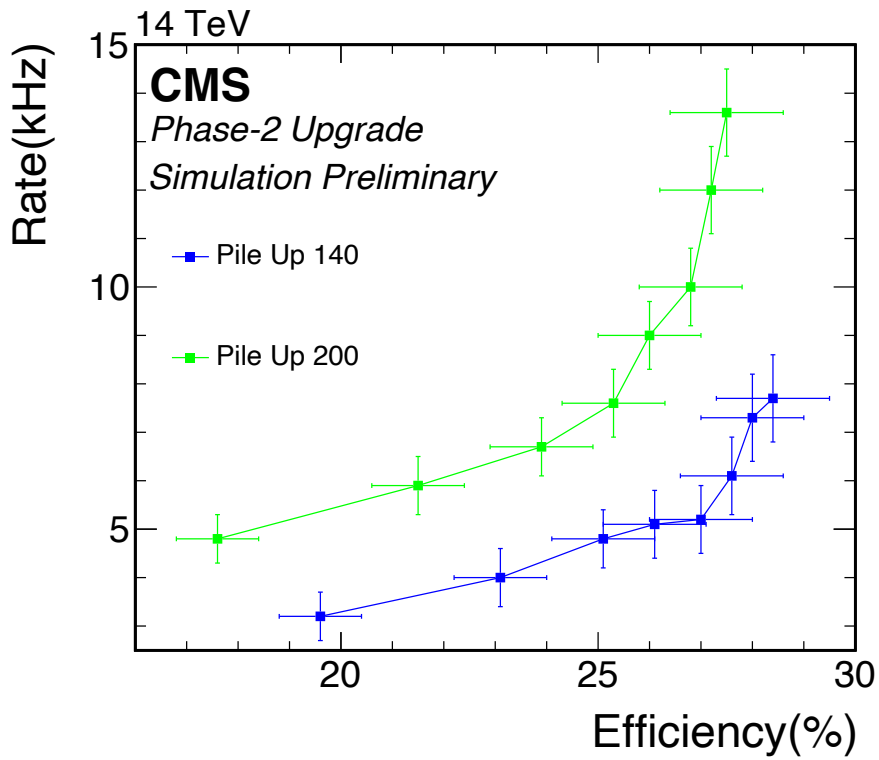


Figure 8.11: ROC curve of signal efficiency vs trigger rate due to variation of $|d_z|$ between a pair of tracks over the range 0.3 – 1.0 cm for $\langle \text{PU} \rangle = 140$ and 200.

8.3.1 Effect of Level-1 tracking p_T threshold on signal efficiency and trigger rate

In order to study the effect of p_T threshold on signal efficiency and trigger rate, the minimum p_T cut on the tracks was increased from 2 GeV to 3 GeV in steps of 100 MeV . The results obtained for $\langle\text{PU}\rangle = 200$ with the medium baseline are shown in Table 8.6. Figure 8.12 shows the ROC curves of signal efficiency vs trigger rate for all the three selection baselines for $\langle\text{PU}\rangle = 140$ and 200 scenarios. From Table 8.6, it can be seen that increasing the L1 tracking p_T threshold will severely affect the signal efficiency.

Table 8.6: Signal efficiency and trigger rate as a function of L1 tracking p_T threshold on the lowest- p_T kaon track of the B_s^0 candidates, for medium baseline selection and $\langle\text{PU}\rangle = 200$. Uncertainties are statistical only.

p_T (GeV)	Efficiency (%)	Rate (kHz)
2.0	27.5 ± 1.1	13.7 ± 0.9
2.1	24.9 ± 1.0	9.4 ± 0.8
2.2	22.2 ± 0.9	7.8 ± 0.7
2.3	19.4 ± 0.9	5.8 ± 0.6
2.4	16.8 ± 0.8	3.6 ± 0.5
2.5	15.0 ± 0.7	2.4 ± 0.4
2.6	13.2 ± 0.7	2.1 ± 0.4
2.7	11.4 ± 0.6	1.2 ± 0.3
2.8	10.1 ± 0.6	0.7 ± 0.2
2.9	8.7 ± 0.5	0.1 ± 0.1
3.0	7.7 ± 0.5	0.0 ± 0.0

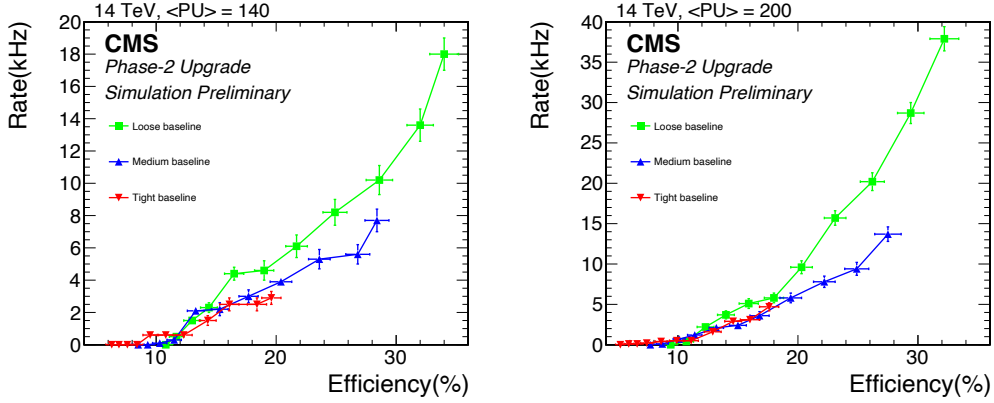


Figure 8.12: ROC curves of signal efficiency vs trigger rate due to variation of L1 tracking p_T threshold on the lowest- p_T kaon track of the B_s^0 candidates over the range 2 – 3 GeV for $\langle \text{PU} \rangle = 140$ and 200. Green, blue and red lines correspond to loose, medium and tight selection baselines respectively. Uncertainties are statistical only.

8.4 Summary

The present study shows that, with the inclusion of tracking at L1 for HL-LHC, CMS can expect to trigger on ~ 30000 $B_s^0 \rightarrow \phi\phi \rightarrow 4$ Kaons signal events with 3000 fb^{-1} data using the medium working point. However, extracting the signal from a huge background at the physics level is very challenging and requires a significant effort.

The encouraging results obtained for $B_s^0 \rightarrow \phi\phi \rightarrow 4$ Kaons at L1 should motivate CMS to look for other physics processes with hadronically decaying light mesons in the final state. For example, in the process $B_s^0 \rightarrow J/\psi\phi$ decay, where J/ψ decays to two muons and ϕ decays to a kaon pair, the reconstructed ϕ candidate and invariant mass of four tracks will allow CMS to lower the muon p_T threshold at L1. Similarly, for rare processes like $H \rightarrow \phi\gamma$ and $H \rightarrow \rho\gamma$, the trigger based on the photon candidate can be combined with a track based light meson trigger to lower the energy

threshold of the photon candidate at the trigger level. In all such cases, lowering the threshold will increase the acceptance of such rare physics processes.

Chapter 10

Appendix

10.1 CMS Datasets for 2016

The single muon datasets, used in the $HH \rightarrow b\bar{b}\tau\tau$ analysis, for the $b\bar{b}\mu\tau_h$ final state are shown in Table 10.1.

Dataset	Run Range	Luminosity (fb^{-1})
/SingleMuon/Run2016B-03Feb2017_ver2-v2/MINIAOD	273150-275376	5.788
/SingleMuon/Run2016C-03Feb2017-v1/MINIAOD	275656-276283	2.573
/SingleMuon/Run2016D-03Feb2017-v1/MINIAOD	276315-276811	4.248
/SingleMuon/Run2016E-03Feb2017-v1/MINIAOD	276831-277420	4.009
/SingleMuon/Run2016F-03Feb2017-v1/MINIAOD	277932-278808	3.102
/SingleMuon/Run2016G-03Feb2017-v1/MINIAOD	278820-280385	7.540
/SingleMuon/Run2016H-03Feb2017_ver2-v1/MINIAOD	281613-284035	8.391
/SingleMuon/Run2016H-03Feb2017_ver3-v1/MINIAOD	284036-284044	0.215

Table 10.1: The single muon datasets, used in the $HH \rightarrow b\bar{b}\tau\tau$ analysis, for the $b\bar{b}\mu\tau_h$ final state.

The single electron datasets, used in the $HH \rightarrow b\bar{b}\tau\tau$ analysis, for the $b\bar{b}e\tau_h$ final

state are shown in Table 10.2.

Dataset	Run Range	Luminosity (fb ⁻¹)
/SingleElectron/Run2016B-03Feb2017_ver2-v2/MINIAOD	273150-275376	5.788
/SingleElectron/Run2016C-03Feb2017-v1/MINIAOD	275656-276283	2.573
/SingleElectron/Run2016D-03Feb2017-v1/MINIAOD	276315-276811	4.248
/SingleElectron/Run2016E-03Feb2017-v1/MINIAOD	276831-277420	4.009
/SingleElectron/Run2016F-03Feb2017-v1/MINIAOD	277932-278808	3.102
/SingleElectron/Run2016G-03Feb2017-v1/MINIAOD	278820-280385	7.540
/SingleElectron/Run2016H-03Feb2017_ver2-v1/MINIAOD	281613-284035	8.391
/SingleElectron/Run2016H-03Feb2017_ver3-v1/MINIAOD	284036-284044	0.215

Table 10.2: The single electron datasets, used in the $HH \rightarrow b\bar{b}\tau\tau$ analysis, for the $b\bar{b}e\tau_h$ final state.

The tau datasets, used in the $HH \rightarrow b\bar{b}\tau\tau$ analysis, for the $b\bar{b}\tau_h\tau_h$ final state are shown in Table 10.3.

Dataset	Run Range	Luminosity (fb ⁻¹)
/Tau/Run2016B-03Feb2017_ver2-v2/MINIAOD	273150-275376	5.788
/Tau/Run2016C-03Feb2017-v1/MINIAOD	275656-276283	2.573
/Tau/Run2016D-03Feb2017-v1/MINIAOD	276315-276811	4.248
/Tau/Run2016E-03Feb2017-v1/MINIAOD	276831-277420	4.009
/Tau/Run2016F-03Feb2017-v1/MINIAOD	277932-278808	3.102
/Tau/Run2016G-03Feb2017-v1/MINIAOD	278820-280385	7.540
/Tau/Run2016H-03Feb2017_ver2-v1/MINIAOD	281613-284035	8.391
/Tau/Run2016H-03Feb2017_ver3-v1/MINIAOD	284036-284044	0.215

Table 10.3: The tau datasets, used in the $HH \rightarrow b\bar{b}\tau\tau$ analysis, for the $b\bar{b}\tau_h\tau_h$ final state.

10.2 Background Monte-Carlo datasets

The $Z/\gamma^* \rightarrow ll + \text{jets}$ and $W \rightarrow l\nu + \text{jets}$ backgrounds datasets are shown in Table 10.4. The datasets for the di-boson and the SM Higgs backgrounds are shown in Table 10.5. The datasets for Electroweak background are shown in Table 10.6. The datasets for $t\bar{t}$ and single top backgrounds are shown in Table 10.7.

	Dataset Name	Cross section (pb)
Drell-Yan datasets		
Inclusive	/DYJetsToLL_M-50_[1]/[2]_v6_ext1-v2/[3]	$5765.4 \pm 1.7\%$
Exclusive	/DY1JetsToLL_M-50_[1]/[2]_v6-v1/[3]	$1175.2 \pm 1.7\%$
	/DY2JetsToLL_M-50_[1]/[2]_v6-v1/[3]	$388.8 \pm 1.7\%$
	/DY3JetsToLL_M-50_[1]/[2]_v6-v1/[3]	$118.0 \pm 1.7\%$
	/DY4JetsToLL_M-50_[1]/[2]_v6-v1/[3]	$64.01 \pm 1.7\%$
	/DYBJetsToLL_M-50_[1]/[2]_v6-v1/[3]	$81.52 \pm 1.7\%$
	/DYBBJetsToLL_M-50_[1]/[2]_v6-v1/[3]	$13.45 \pm 1.7\%$
W + jets datasets		
Inclusive	/WJetsToLNu_[1]/[2]_v6-v1/[3]	$61526.7 \pm 3.8\%$
	/WJetsToLNu_[1]/[2]_v6_ext2-v1/[3]	"
Exclusive	/WJetsToLNu_HT-70To100_[1]/[2]_v6-v1/[3]	$1727.8 \pm 3.8\%$
	/WJetsToLNu_HT-100To200_[1]/[2]_v6-v1/[3]	$1632.5 \pm 3.8\%$
	/WJetsToLNu_HT-100To200_[1]/[2]_v6_ext1-v1/[3]	"
	/WJetsToLNu_HT-100To200_[1]/[2]_v6_ext2-v1/[3]	"
	/WJetsToLNu_HT-200To400_[1]/[2]_v6-v1/[3]	$436.6 \pm 3.8\%$
	/WJetsToLNu_HT-200To400_[1]/[2]_v6_ext1-v1/[3]	"
	/WJetsToLNu_HT-200To400_[1]/[2]_v6_ext2-v1/[3]	"
	/WJetsToLNu_HT-400To600_[1]/[2]_v6-v1/[3]	$59.4 \pm 3.8\%$
	/WJetsToLNu_HT-400To600_[1]/[2]_v6_ext1-v1/[3]	"
	/WJetsToLNu_HT-600To800_[1]/[2]_v6-v1/[3]	$14.6 \pm 3.8\%$
	/WJetsToLNu_HT-600To800_[1]/[2]_v6_ext1-v1/[3]	"
	/WJetsToLNu_HT-800To1200_[1]/[2]_v6-v1/[3]	$6.68 \pm 3.8\%$
	/WJetsToLNu_HT-800To1200_[1]/[2]_v6_ext1-v1/[3]	"
	/WJetsToLNu_HT-1200To2500_[1]/[2]_v6-v1/[3]	$1.61 \pm 3.8\%$
	/WJetsToLNu_HT-1200To2500_[1]/[2]_v6_ext1-v1/[3]	"
	/WJetsToLNu_HT-2500ToInf_[1]/[2]_v6-v1/[3]	$0.0390 \pm 3.8\%$
/WJetsToLNu_HT-2500ToInf_[1]/[2]_v6_ext1-v1/[3]	"	
[1] = TuneCUETP8M1_13TeV-madgraphMLM-pythia8 [2] = RunIISummer16MiniAODv2-PUMoriond17_80X_mcRun2_asymptotic_2016_TracheIV [3] = MINIAODSIM		

Table 10.4: Drell-Yan + jets and W + jets background datasets.

Dataset Name	Cross section (pb)
Di-boson datasets	
/WWTto2L2Nu_[1]/[2]_v6-v1/[3]	12.19 ± 10%
/WWTtoLNUQQ_[1]/[2]_v6-v1/[3]	50.00 ± 10%
/WWTtoLNUQQ_[1]/[2]_v6_ext1-v1/[3]	"
/WWTto4Q_[1]/[2]_v6-v1/[3]	51.72 ± 10%
/WZTo3LNU_[1]/[2]_v6-v1/[3]	4.43 ± 10%
/WZTo1L3NU_[1]/[2]_v6-v1/[3]	3.03 ± 10%
/WZTo1L1Nu2Q_[1]/[2]_v6-v3/[3]	10.71 ± 10%
/WZTo2L2Q_[1]/[2]_v6-v1/[3]	5.60 ± 10%
/ZZTo2L2Nu_[1]/[2]_v6-v1/[3]	0.564 ± 10%
/ZZTo2L2Q_[1]/[2]_v6-v1/[3]	3.22 ± 10%
/ZZTo4L_[1]/[2]_v6_ext1-v1/[3]	1.21 ± 10%
/ZZTo4Q_[1]/[2]_v6-v1/[3]	7.06 ± 10%
SM Higgs	
/ZHToTauTau_M125_[1]/[2]_v6-v1/[3]	0.0559 ^{+4.1%} _{-3.5%}
/ZH_HToBB_ZToLL_M125_[1]/[2]_v6-v1/[3]	0.0515 ^{+4.1%} _{-3.5%}
/ZH_HToBB_ZToLL_M125_[1]/[2]_v6_ext1-v1/[3]	"
/ZH_HToBB_ZToQQ_M125_[1]/[2]_v6-v1/[3]	0.357 ^{+4.1%} _{-3.5%}
[1] = TuneCUETP8M1_13TeV-madgraphMLM-pythia8	
[2] = RunIISummer16MiniAODv2-PUMoriond17_80X_mcRun2_asymptotic_2016-TrancheIV	
[3] = MINIAODSIM	

Table 10.5: Di-boson and the SM Higgs background datasets.

10.3 Signal Monte-Carlo Datasets

10.3.1 Resonant Datasets

The Spin-0 resonant $pp \rightarrow X \rightarrow HH$ datasets, used in the $HH \rightarrow b\bar{b}\tau\tau$ analysis are shown in Table 10.8.

The Spin-2 resonant $pp \rightarrow X \rightarrow HH$ datasets, used in the $HH \rightarrow b\bar{b}\tau\tau$ analysis are shown in Table 10.9.

Dataset Name	Cross section (pb)
Electroweak Datasets	
/EWKWPlus2Jets_WToLNu_M-50_[1]/[2]_v6-v1/[3]	$25.62 \pm 2\%$
/EWKWPlus2Jets_WToLNu_M-50_[1]/[2]_v6_ext1-v1/[3]	"
/EWKWPlus2Jets_WToLNu_M-50_[1]/[2]_v6_ext2-v1/[3]	"
/EWKWMinus2Jets_WToLNu_M-50_[1]/[2]_v6-v1/[3]	$20.25 \pm 2\%$
/EWKWMinus2Jets_WToLNu_M-50_[1]/[2]_v6_ext1-v1/[3]	"
/EWKWMinus2Jets_WToLNu_M-50_[1]/[2]_v6_ext2-v1/[3]	"
/EWKZ2Jets_ZToLL_M-50_[1]/[2]_v6-v1/[3]	$3.987 \pm 2\%$
/EWKZ2Jets_ZToLL_M-50_[1]/[2]_v6_ext2-v1/[3]	"
/EWKZ2Jets_ZToLL_M-50_[1]/[2]_v6_ext1-v1/[3]	"
[1] = TuneCUETP8M1_13TeV-madgraph-pythia8	
[2] = RunIISummer16MiniAODv2-PUMoriond17_80X_mcRun2_asymptotic_2016_TracheIV	
[3] = MINIAODSIM	

Table 10.6: Electroweak background datasets

10.3.2 Non-Resonant Datasets

The non-resonant $pp \rightarrow HH$ datasets, used in the $HH \rightarrow b\bar{b}\tau\tau$ analysis, are shown in Table 10.10.

Dataset Name	Cross section (pb)
<i>t\bar{t}</i> Datasets	
/TTTo2L2Nu_[1]/[2]_v6-v1/[3]	87.3 \pm 4.5
/TTToSemilepton_[1]/[2]_v6-v1/[3]	364.3 \pm 18.6
/TT_[1]/[2]_v6-v1/[3]	831.76 \pm 42.5
/TT_[1]/[2]_v6-v1/[3]	831.76 \pm 42.5
Single top Datasets	
/ST_tW_antitop_5f_inclusiveDecays_[1]/[2]_v6_ext1-v1/[3]	35.6 \pm 1.9
/ST_tW_top_5f_inclusiveDecays_[1]/[2]_v6_ext1-v1/[3]	35.6 \pm 1.9
[1] = TuneCUETP8M1_13TeV-powheg-pythia8	
[2] = RunIISummer16MiniAODv2-PUMoriond17_80X_mcRun2_asymptotic_2016_TrancheIV	
[3] = MINIAODSIM	

Table 10.7: *t \bar{t}* and Single top background datasets

Resonant spin-0 samples	
/GluGluToRadionToHHTo2B2Tau_M-250_[1]/[2]_v6-v1/[3]	
/GluGluToRadionToHHTo2B2Tau_M-270_[1]/[2]_v6-v1/[3]	
/GluGluToRadionToHHTo2B2Tau_M-280_[1]/[2]_v6-v1/[3]	
/GluGluToRadionToHHTo2B2Tau_M-300_[1]/[2]_v6_ext1-v1/[3]	
/GluGluToRadionToHHTo2B2Tau_M-350_[1]/[2]_v6-v1/[3]	
/GluGluToRadionToHHTo2B2Tau_M-400_[1]/[2]_v6_ext1-v3/[3]	
/GluGluToRadionToHHTo2B2Tau_M-450_[1]/[2]_v6-v1/[3]	
/GluGluToRadionToHHTo2B2Tau_M-500_[1]/[2]_v6-v1/[3]	
/GluGluToRadionToHHTo2B2Tau_M-550_[1]/[2]_v6-v1/[3]	
/GluGluToRadionToHHTo2B2Tau_M-600_[1]/[2]_v6-v1/[3]	
/GluGluToRadionToHHTo2B2Tau_M-650_[1]/[2]_v6-v1/[3]	
/GluGluToRadionToHHTo2B2Tau_M-750_[1]/[2]_v6-v1/[3]	
/GluGluToRadionToHHTo2B2Tau_M-900_[1]/[2]_v6-v1/[3]	
[1] = narrow_13TeV-madgraph	
[2] = RunIISummer16MiniAODv2-PUMoriond17_80X_mcRun2_asymptotic_2016_TrancheIV	
[3] = MINIAODSIM	

Table 10.8: List of resonant spin-0 signal samples.

Resonant spin-2 samples
/GluGluToBulkGravitonToHHTo2B2Tau_M-250_[1]/[2]_v6-v1/[3]
/GluGluToBulkGravitonToHHTo2B2Tau_M-260_[1]/[2]_v6-v1/[3]
/GluGluToBulkGravitonToHHTo2B2Tau_M-270_[1]/[2]_v6-v1/[3]
/GluGluToBulkGravitonToHHTo2B2Tau_M-280_[1]/[2]_v6-v1/[3]
/GluGluToBulkGravitonToHHTo2B2Tau_M-300_[1]/[2]_v6_ext1-v1/[3]
/GluGluToBulkGravitonToHHTo2B2Tau_M-340_[1]/[2]_v6-v1/[3]
/GluGluToBulkGravitonToHHTo2B2Tau_M-350_[1]/[2]_v6-v1/[3]
/GluGluToBulkGravitonToHHTo2B2Tau_M-400_[1]/[2]_v6_ext1-v1/[3]
/GluGluToBulkGravitonToHHTo2B2Tau_M-450_[1]/[2]_v6-v1/[3]
/GluGluToBulkGravitonToHHTo2B2Tau_M-550_[1]/[2]_v6-v1/[3]
/GluGluToBulkGravitonToHHTo2B2Tau_M-600_[1]/[2]_v6-v1/[3]
/GluGluToBulkGravitonToHHTo2B2Tau_M-650_[1]/[2]_v6-v1/[3]
/GluGluToBulkGravitonToHHTo2B2Tau_M-750_[1]/[2]_v6-v1/[3]
/GluGluToBulkGravitonToHHTo2B2Tau_M-800_[1]/[2]_v6-v1/[3]
[1] = narrow_13TeV-madgraph
[2] = RunIISummer16MiniAODv2-PUMoriond17_80X_mcRun2_asymptotic_2016_TracheIV
[3] = MINIAODSIM

Table 10.9: List of resonant spin-2 signal samples.

Non-resonant samples
/GluGluToHHTo2B2Tau_node_SM_[1]/[2]_v6-v1/[3]
/GluGluToHHTo2B2Tau_node_box_[1]/[2]_v6-v1/[3]
/GluGluToHHTo2B2Tau_node_2_[1]/[2]_v6-v1/[3]
/GluGluToHHTo2B2Tau_node_10_[1]/[2]_v6-v1/[3]
/GluGluToHHTo2B2Tau_node_11_[1]/[2]_v6-v1/[3]
/GluGluToHHTo2B2Tau_node_12_[1]/[2]_v6-v1/[3]
[1] = 13TeV-madgraph
[2] = RunIISummer16MiniAODv2-PUMoriond17_80X_mcRun2_asymptotic_2016_TracheIV
[3] = MINIAODSIM

Table 10.10: List of non-resonant signal samples.

Bibliography

- [1] CMS collaboration, *Description and performance of track and primary-vertex reconstruction with the CMS tracker*, *JINST* **9** (2014) P10009 [[1405.6569](#)].
- [2] CMS collaboration, *Performance of the CMS muon detector and muon reconstruction with proton-proton collisions at $\sqrt{s} = 13$ TeV*, *JINST* **13** (2018) P06015 [[1804.04528](#)].
- [3] CMS collaboration, *Reconstruction and identification of τ lepton decays to hadrons and ν_τ at CMS*, *JINST* **11** (2016) P01019 [[1510.07488](#)].
- [4] A. J. Barr, M. J. Dolan, C. Englert and M. Spannowsky, *Di-Higgs final states augMT2ed – selecting hh events at the high luminosity LHC*, *Phys. Lett. B* **728** (2014) 308 [[1309.6318](#)].
- [5] CMS collaboration, *Search for Higgs boson pair production in events with two bottom quarks and two tau leptons in proton–proton collisions at $\sqrt{s} = 13$ TeV*, *Phys. Lett. B* **778** (2018) 101 [[1707.02909](#)].
- [6] CMS collaboration, *The Phase-2 Upgrade of the CMS Tracker*, .
- [7] D. Braga, G. Hall, L. Jones, P. Murray, M. Pesaresi, M. Prydderch et al., *Characterization of the CBC2 readout ASIC for the CMS strip-tracker high-luminosity upgrade*, *JINST* **9** (2014) C03001.
- [8] G. Hall et al., *CBC2: A CMS microstrip readout ASIC with logic for track-trigger modules at HL-LHC*, *Nucl. Instrum. Meth. A* **765** (2014) 214.

- [9] D. Braga, G. Hall, L. Jones, P. Murray, M. Pesaresi, M. Prydderch et al., *CBC2: A microstrip readout ASIC with coincidence logic for trigger primitives at HL-LHC*, *JINST* **7** (2012) C10003.
- [10] PARTICLE DATA GROUP collaboration, *Review of Particle Physics*, *PTEP* **2020** (2020) 083C01.
- [11] A. Carvalho, M. Dall’Osso, T. Dorigo, F. Goertz, C. A. Gottardo and M. Tosi, *Higgs Pair Production: Choosing Benchmarks With Cluster Analysis*, *JHEP* **04** (2016) 126 [1507.02245].
- [12] A. Carvalho, M. Dall’Osso, P. De Castro Manzano, T. Dorigo, F. Goertz, M. Gouzevich et al., *Analytical parametrization and shape classification of anomalous HH production in the EFT approach*, **1608.06578**.
- [13] ATLAS collaboration, *The ATLAS Experiment at the CERN Large Hadron Collider*, *JINST* **3** (2008) S08003.
- [14] CMS collaboration, *The CMS Experiment at the CERN LHC*, *JINST* **3** (2008) S08004.
- [15] ATLAS collaboration, *Observation of a new particle in the search for the Standard Model Higgs boson with the ATLAS detector at the LHC*, *Phys. Lett. B* **716** (2012) 1 [1207.7214].
- [16] CMS collaboration, *Observation of a New Boson at a Mass of 125 GeV with the CMS Experiment at the LHC*, *Phys. Lett. B* **716** (2012) 30 [1207.7235].

- [17] ATLAS, CMS collaboration, *Combined Measurement of the Higgs Boson Mass in pp Collisions at $\sqrt{s} = 7$ and 8 TeV with the ATLAS and CMS Experiments*, *Phys. Rev. Lett.* **114** (2015) 191803 [[1503.07589](#)].
- [18] ATLAS, CMS collaboration, *Measurements of the Higgs boson production and decay rates and constraints on its couplings from a combined ATLAS and CMS analysis of the LHC pp collision data at $\sqrt{s} = 7$ and 8 TeV*, *JHEP* **08** (2016) 045 [[1606.02266](#)].
- [19] J. Baglio, A. Djouadi, R. Gröber, M. Mühlleitner, J. Quevillon and M. Spira, *The measurement of the Higgs self-coupling at the LHC: theoretical status*, *JHEP* **04** (2013) 151 [[1212.5581](#)].
- [20] F. Goertz, A. Papaefstathiou, L. L. Yang and J. Zurita, *Higgs boson pair production in the $D=6$ extension of the SM*, *JHEP* **04** (2015) 167 [[1410.3471](#)].
- [21] T. Binoth and J. van der Bij, *Influence of strongly coupled, hidden scalars on Higgs signals*, *Z. Phys. C* **75** (1997) 17 [[hep-ph/9608245](#)].
- [22] R. M. Schabinger and J. D. Wells, *A Minimal spontaneously broken hidden sector and its impact on Higgs boson physics at the large hadron collider*, *Phys. Rev. D* **72** (2005) 093007 [[hep-ph/0509209](#)].
- [23] B. Patt and F. Wilczek, *Higgs-field portal into hidden sectors*, [hep-ph/0605188](#).

- [24] G. Branco, P. Ferreira, L. Lavoura, M. Rebelo, M. Sher and J. P. Silva, *Theory and phenomenology of two-Higgs-doublet models*, *Phys. Rept.* **516** (2012) 1 [[1106.0034](#)].
- [25] P. Fayet, *Supergauge Invariant Extension of the Higgs Mechanism and a Model for the electron and Its Neutrino*, *Nucl. Phys. B* **90** (1975) 104.
- [26] P. Fayet, *Spontaneously Broken Supersymmetric Theories of Weak, Electromagnetic and Strong Interactions*, *Phys. Lett. B* **69** (1977) 489.
- [27] A. Djouadi, L. Maiani, G. Moreau, A. Polosa, J. Quevillon and V. Riquer, *The post-Higgs MSSM scenario: Habemus MSSM?*, *Eur. Phys. J. C* **73** (2013) 2650 [[1307.5205](#)].
- [28] A. Djouadi, L. Maiani, A. Polosa, J. Quevillon and V. Riquer, *Fully covering the MSSM Higgs sector at the LHC*, *JHEP* **06** (2015) 168 [[1502.05653](#)].
- [29] K. Agashe, H. Davoudiasl, G. Perez and A. Soni, *Warped Gravitons at the LHC and Beyond*, *Phys. Rev. D* **76** (2007) 036006 [[hep-ph/0701186](#)].
- [30] A. Fitzpatrick, J. Kaplan, L. Randall and L.-T. Wang, *Searching for the Kaluza-Klein Graviton in Bulk RS Models*, *JHEP* **09** (2007) 013 [[hep-ph/0701150](#)].
- [31] S. King, *Neutrino mass models*, *Rept. Prog. Phys.* **67** (2004) 107 [[hep-ph/0310204](#)].

- [32] D. J. Gross, *The role of symmetry in fundamental physics*, *Proceedings of the National Academy of Sciences* **93** (1996) 14256
[<https://www.pnas.org/content/93/25/14256.full.pdf>].
- [33] A. Lahiri and P. B. Pal, *A First Book of Quantum Field Theory*. 2005.
- [34] E. Fermi, *An attempt of a theory of beta radiation. 1.*, *Z. Phys.* **88** (1934) 161.
- [35] S. Glashow, *Partial Symmetries of Weak Interactions*, *Nucl. Phys.* **22** (1961) 579.
- [36] T. Lee, M. Rosenbluth and C.-N. Yang, *Interaction of Mesons With Nucleons and Light Particles*, *Phys. Rev.* **75** (1949) 905.
- [37] S. Weinberg, *A Model of Leptons*, *Phys. Rev. Lett.* **19** (1967) 1264.
- [38] A. Salam, *Weak and Electromagnetic Interactions*, *Conf. Proc. C* **680519** (1968) 367.
- [39] N. Cabibbo, *Unitary Symmetry and Leptonic Decays*, *Phys. Rev. Lett.* **10** (1963) 531.
- [40] M. Kobayashi and T. Maskawa, *CP Violation in the Renormalizable Theory of Weak Interaction*, *Prog. Theor. Phys.* **49** (1973) 652.
- [41] Y. Nambu, *Axial vector current conservation in weak interactions*, *Phys. Rev. Lett.* **4** (1960) 380.
- [42] J. Goldstone, *Field Theories with Superconductor Solutions*, *Nuovo Cim.* **19** (1961) 154.

- [43] F. Englert and R. Brout, *Broken Symmetry and the Mass of Gauge Vector Mesons*, *Phys. Rev. Lett.* **13** (1964) 321.
- [44] P. W. Higgs, *Broken symmetries, massless particles and gauge fields*, *Phys. Lett.* **12** (1964) 132.
- [45] P. W. Higgs, *Broken Symmetries and the Masses of Gauge Bosons*, *Phys. Rev. Lett.* **13** (1964) 508.
- [46] G. Guralnik, C. Hagen and T. Kibble, *Global Conservation Laws and Massless Particles*, *Phys. Rev. Lett.* **13** (1964) 585.
- [47] PARTICLE DATA GROUP collaboration, *Review of Particle Physics*, *Phys. Rev. D* **98** (2018) 030001.
- [48] LHC HIGGS CROSS SECTION WORKING GROUP collaboration, *Handbook of LHC Higgs Cross Sections: 4. Deciphering the Nature of the Higgs Sector*, [1610.07922](#).
- [49] S. Borowka, N. Greiner, G. Heinrich, S. Jones, M. Kerner, J. Schlenk et al., *Higgs Boson Pair Production in Gluon Fusion at Next-to-Leading Order with Full Top-Quark Mass Dependence*, *Phys. Rev. Lett.* **117** (2016) 012001 [[1604.06447](#)].
- [50] S. Borowka, N. Greiner, G. Heinrich, S. Jones, M. Kerner, J. Schlenk et al., *Full top quark mass dependence in Higgs boson pair production at NLO*, *JHEP* **10** (2016) 107 [[1608.04798](#)].

- [51] D. de Florian and J. Mazzitelli, *Higgs pair production at next-to-next-to-leading logarithmic accuracy at the LHC*, *JHEP* **09** (2015) 053 [[1505.07122](#)].
- [52] G. Degrandi, P. P. Giardino and R. Gröber, *On the two-loop virtual QCD corrections to Higgs boson pair production in the Standard Model*, *Eur. Phys. J. C* **76** (2016) 411 [[1603.00385](#)].
- [53] J. Bernon, J. F. Gunion, H. E. Haber, Y. Jiang and S. Kraml, *Scrutinizing the alignment limit in two-Higgs-doublet models: $m_h=125$ GeV*, *Phys. Rev. D* **92** (2015) 075004 [[1507.00933](#)].
- [54] D0 collaboration, *Measurement of the CP-violating phase $\phi_s^{J/\psi\phi}$ using the flavor-tagged decay $B_s^0 \rightarrow J/\psi\phi$ in 8 fb^{-1} of $p\bar{p}$ collisions*, *Phys. Rev. D* **85** (2012) 032006 [[1109.3166](#)].
- [55] CMS collaboration, *Measurement of the CP-violating weak phase ϕ_s and the decay width difference $\Delta\Gamma_s$ using the $B_s^0 \rightarrow J/\psi\phi(1020)$ decay channel in pp collisions at $\sqrt{s} = 8 \text{ TeV}$* , *Phys. Lett.* **B757** (2016) 97 [[1507.07527](#)].
- [56] M. Bartsch, G. Buchalla and C. Kraus, *$B \rightarrow_j V(L) V(L)$ Decays at Next-to-Leading Order in QCD*, [0810.0249](#).
- [57] M. Beneke, J. Rohrer and D. Yang, *Branching fractions, polarisation and asymmetries of $B \rightarrow_j VV$ decays*, *Nucl. Phys.* **B774** (2007) 64 [[hep-ph/0612290](#)].

- [58] H.-Y. Cheng and C.-K. Chua, *QCD Factorization for Charmless Hadronic B_s Decays Revisited*, *Phys. Rev.* **D80** (2009) 114026 [[0910.5237](#)].
- [59] CDF collaboration, *First evidence for $B_s^0 \rightarrow \phi\phi$ decay and measurements of branching ratio and A_{CP} for $B^+ \rightarrow \phi K^+$* , *Phys. Rev. Lett.* **95** (2005) 031801 [[hep-ex/0502044](#)].
- [60] CDF collaboration, *Measurement of Polarization and Search for CP-Violation in $B_s^0 \rightarrow \phi\phi$ Decays*, *Phys. Rev. Lett.* **107** (2011) 261802 [[1107.4999](#)].
- [61] LHCb collaboration, *First measurement of the CP-violating phase in $B_s^0 \rightarrow \phi\phi$ decays*, *Phys. Rev. Lett.* **110** (2013) 241802 [[1303.7125](#)].
- [62] LHCb collaboration, *Measurement of the polarization amplitudes and triple product asymmetries in the $B_s^0 \rightarrow \phi\phi$ decay*, *Phys. Lett.* **B713** (2012) 369 [[1204.2813](#)].
- [63] LHCb collaboration, *Measurement of CP violation in $B_s^0 \rightarrow \phi\phi$ decays*, *Phys. Rev.* **D90** (2014) 052011 [[1407.2222](#)].
- [64] LHCb collaboration, *Measurement of the $B_s^0 \rightarrow \phi\phi$ branching fraction and search for the decay $B^0 \rightarrow \phi\phi$* , *JHEP* **10** (2015) 053 [[1508.00788](#)].
- [65] LHCb collaboration, *Measurement of CP violation in the $B_s^0 \rightarrow \phi\phi$ decay and search for the $B^0 \rightarrow \phi\phi$ decay*, *JHEP* **12** (2019) 155 [[1907.10003](#)].
- [66] *LHC Machine*, *JINST* **3** (2008) S08001.

- [67] A. Ster, *Linac2 performance optimization*, .
- [68] K. Reich, *The CERN Proton Synchrotron Booster*, *IEEE Trans. Nucl. Sci.* **16** (1969) 959.
- [69] *The CERN proton synchrotron*, .
- [70] L. A. Dyks, D. Posthuma de Boer, A. Ross, M. Backhouse, S. Alden, G. L. D' Alessandro et al., *The Superconducting Super Proton Synchrotron*, .
- [71] ALICE collaboration, *The ALICE experiment at the CERN LHC*, *JINST* **3** (2008) S08002.
- [72] LHCb collaboration, *The LHCb Detector at the LHC*, *JINST* **3** (2008) S08005.
- [73] E. Wilson, *An introduction to particle accelerators*. 11, 2001.
- [74] CMS collaboration, *CMS, the magnet project: Technical design report*, .
- [75] CMS collaboration, *The CMS tracker system project: Technical Design Report*, .
- [76] CMS collaboration, *The CMS tracker: addendum to the Technical Design Report*, .
- [77] W. Leo, *Techniques for Nuclear and Particle Physics Experiments: A How to Approach*. 1987.

- [78] CMS collaboration, *The CMS electromagnetic calorimeter project: Technical Design Report*, .
- [79] CMS collaboration, *CMS: The hadron calorimeter technical design report*, .
- [80] CMS collaboration, *The CMS muon project: Technical Design Report*, .
- [81] *HLTPlotsSummary2016*.
- [82] J. Alwall, R. Frederix, S. Frixione, V. Hirschi, F. Maltoni, O. Mattelaer et al., *The automated computation of tree-level and next-to-leading order differential cross sections, and their matching to parton shower simulations*, *JHEP* **07** (2014) 079 [[1405.0301](#)].
- [83] J. Alwall et al., *A Standard format for Les Houches event files*, *Comput. Phys. Commun.* **176** (2007) 300 [[hep-ph/0609017](#)].
- [84] T. Sjöstrand, S. Ask, J. R. Christiansen, R. Corke, N. Desai, P. Ilten et al., *An Introduction to PYTHIA 8.2*, *Comput. Phys. Commun.* **191** (2015) 159 [[1410.3012](#)].
- [85] GEANT4 collaboration, *GEANT4: A Simulation toolkit*, *Nucl. Instrum. Meth. A* **506** (2003) 250.
- [86] R. Brun and F. Rademakers, *ROOT: An object oriented data analysis framework*, *Nucl. Instrum. Meth. A* **389** (1997) 81.
- [87] K. Rose, *Deterministic annealing for clustering, compression, classification, regression, and related optimization problems*, *IEEE Proc.* **86** (1998) 2210.

- [88] R. Fruhwirth, W. Waltenberger and P. Vanlaer, *Adaptive vertex fitting*, *J. Phys. G* **34** (2007) N343.
- [89] CMS collaboration, *The CMS Particle Flow Algorithm*, in *International Conference on Calorimetry for the High Energy Frontier*, pp. 295–304, 2013, [1401.8155](#).
- [90] S. Baffioni, C. Charlot, F. Ferri, D. Futyan, P. Meridiani, I. Puljak et al., *Electron reconstruction in CMS*, *Eur. Phys. J. C* **49** (2007) 1099.
- [91] CMS collaboration, *Performance of Electron Reconstruction and Selection with the CMS Detector in Proton-Proton Collisions at $\sqrt{s} = 8$ TeV*, *JINST* **10** (2015) P06005 [[1502.02701](#)].
- [92] CMS collaboration, *CMS Electron and Photon Performance at 13 TeV*, *J. Phys. Conf. Ser.* **1162** (2019) 012008.
- [93] W. Adam, R. Frühwirth, A. Strandlie and T. Todor, *Reconstruction of Electrons with the Gaussian-Sum Filter in the CMS Tracker at the LHC*, .
- [94] R. Fruhwirth, *Track fitting with nonGaussian noise*, *Comput. Phys. Commun.* **100** (1997) 1.
- [95] A. Hocker et al., *TMVA - Toolkit for Multivariate Data Analysis*, [physics/0703039](#).
- [96] S. Marzani, G. Soyez and M. Spannowsky, *Looking inside jets: an introduction to jet substructure and boosted-object phenomenology*, vol. 958. Springer, 2019, [10.1007/978-3-030-15709-8](#), [[1901.10342](#)].

- [97] G. P. Salam, *Towards Jetography*, *Eur. Phys. J. C* **67** (2010) 637 [[0906.1833](#)].
- [98] M. Cacciari, G. P. Salam and G. Soyez, *The anti- k_t jet clustering algorithm*, *JHEP* **04** (2008) 063 [[0802.1189](#)].
- [99] M. Cacciari, G. P. Salam and G. Soyez, *FastJet User Manual*, *Eur. Phys. J. C* **72** (2012) 1896 [[1111.6097](#)].
- [100] J. M. Butterworth, A. R. Davison, M. Rubin and G. P. Salam, *Jet substructure as a new Higgs search channel at the LHC*, *Phys. Rev. Lett.* **100** (2008) 242001 [[0802.2470](#)].
- [101] A. J. Larkoski, S. Marzani, G. Soyez and J. Thaler, *Soft Drop*, *JHEP* **05** (2014) 146 [[1402.2657](#)].
- [102] CMS collaboration, *Determination of Jet Energy Calibration and Transverse Momentum Resolution in CMS*, *JINST* **6** (2011) P11002 [[1107.4277](#)].
- [103] CMS collaboration, *Jet energy scale and resolution in the CMS experiment in pp collisions at 8 TeV*, *JINST* **12** (2017) P02014 [[1607.03663](#)].
- [104] C. Weiser, *A combined secondary vertex based B-tagging algorithm in CMS*, .
- [105] CMS collaboration, *Performance of missing transverse momentum reconstruction in proton-proton collisions at $\sqrt{s} = 13$ TeV using the CMS detector*, *JINST* **14** (2019) P07004 [[1903.06078](#)].

- [106] E. Re, *Single-top Wt -channel production matched with parton showers using the POWHEG method*, *Eur. Phys. J. C* **71** (2011) 1547 [[1009.2450](#)].
- [107] J. M. Campbell, R. K. Ellis, P. Nason and E. Re, *Top-Pair Production and Decay at NLO Matched with Parton Showers*, *JHEP* **04** (2015) 114 [[1412.1828](#)].
- [108] NNPDF collaboration, *Parton distributions for the LHC Run II*, *JHEP* **04** (2015) 040 [[1410.8849](#)].
- [109] CMS collaboration, *Event generator tunes obtained from underlying event and multiparton scattering measurements*, *Eur. Phys. J. C* **76** (2016) 155 [[1512.00815](#)].
- [110] J. Alwall et al., *Comparative study of various algorithms for the merging of parton showers and matrix elements in hadronic collisions*, *Eur. Phys. J. C* **53** (2008) 473 [[0706.2569](#)].
- [111] M. Czakon and A. Mitov, *Top++: A Program for the Calculation of the Top-Pair Cross-Section at Hadron Colliders*, *Comput. Phys. Commun.* **185** (2014) 2930 [[1112.5675](#)].
- [112] Y. Li and F. Petriello, *Combining QCD and electroweak corrections to dilepton production in FEWZ*, *Phys. Rev. D* **86** (2012) 094034 [[1208.5967](#)].
- [113] A. Ali, Y. Bystritskiy and M. Ivanov, eds., *Proceedings, Helmholtz International Summer School on Physics of Heavy Quarks and Hadrons (HQ*

2013): JINR, Dubna, Russia, July 15-28, 2013, (Hamburg), DESY, 2014.
10.3204/DESY-PROC-2013-03.

- [114] J. M. Campbell, R. Ellis and C. Williams, *Vector boson pair production at the LHC*, *JHEP* **07** (2011) 018 [[1105.0020](#)].
- [115] O. Brein, R. V. Harlander and T. J. Zirke, *vh@nnlo - Higgs Strahlung at hadron colliders*, *Comput. Phys. Commun.* **184** (2013) 998 [[1210.5347](#)].
- [116] R. V. Harlander, S. Liebler and T. Zirke, *Higgs Strahlung at the Large Hadron Collider in the 2-Higgs-Doublet Model*, *JHEP* **02** (2014) 023 [[1307.8122](#)].
- [117] O. Brein, A. Djouadi and R. Harlander, *NNLO QCD corrections to the Higgs-strahlung processes at hadron colliders*, *Phys. Lett. B* **579** (2004) 149 [[hep-ph/0307206](#)].
- [118] L. Altenkamp, S. Dittmaier, R. V. Harlander, H. Rzehak and T. J. Zirke, *Gluon-induced Higgs-strahlung at next-to-leading order QCD*, *JHEP* **02** (2013) 078 [[1211.5015](#)].
- [119] L. Bianchini, J. Conway, E. K. Friis and C. Veelken, *Reconstruction of the Higgs mass in $H \rightarrow \tau\tau$ Events by Dynamical Likelihood techniques*, *J. Phys. Conf. Ser.* **513** (2014) 022035.
- [120] CMS collaboration, *Searches for a heavy scalar boson H decaying to a pair of 125 GeV Higgs bosons hh or for a heavy pseudoscalar boson A decaying to Zh , in the final states with $h \rightarrow \tau\tau$* , *Phys. Lett. B* **755** (2016) 217 [[1510.01181](#)].

- [121] C. Lester and D. Summers, *Measuring masses of semiinvisibly decaying particles pair produced at hadron colliders*, *Phys. Lett. B* **463** (1999) 99 [[hep-ph/9906349](#)].
- [122] A. Barr, C. Lester and P. Stephens, *$m(T^2)$: The Truth behind the glamour*, *J. Phys. G* **29** (2003) 2343 [[hep-ph/0304226](#)].
- [123] CDF collaboration, *A Measurement of the ratio $\sigma \times B(p\bar{p} \rightarrow W \rightarrow e\nu)/\sigma \times B(p\bar{p} \rightarrow Z^0 \rightarrow ee)$ in $p\bar{p}$ collisions at $\sqrt{s} = 1800$ GeV*, *Phys. Rev. D* **52** (1995) 2624.
- [124] CMS collaboration, *Measurements of differential production cross sections for a Z boson in association with jets in pp collisions at $\sqrt{s} = 8$ TeV*, *JHEP* **04** (2017) 022 [[1611.03844](#)].
- [125] *The CMS Higgs Combined Tool*.
- [126] T. Junk, *Confidence level computation for combining searches with small statistics*, *Nucl. Instrum. Meth. A* **434** (1999) 435 [[hep-ex/9902006](#)].
- [127] A. L. Read, *Presentation of search results: The $CL(s)$ technique*, *J. Phys. G* **28** (2002) 2693.
- [128] A. Oliveira, *Gravity particles from Warped Extra Dimensions, predictions for LHC*, [1404.0102](#).
- [129] C. Collaboration, *The Phase-2 Upgrade of the CMS Muon Detectors*, Tech. Rep. CERN-LHCC-2017-012. CMS-TDR-016, CERN, Geneva, Sep, 2017.

- [130] CMS HGCAL BEAM TEST GROUP collaboration, *The CMS High Granularity Calorimeter for HL-LHC*, *JINST* **14** (2019) C05002.
- [131] C. CMS, *A MIP Timing Detector for the CMS Phase-2 Upgrade*, Tech. Rep. CERN-LHCC-2019-003. CMS-TDR-020, CERN, Geneva, Mar, 2019.
- [132] A. Caratelli, D. Ceresa, J. Kaplon, K. Kloukinas, Y. Leblebici, J. Murdzek et al., *Short-Strip ASIC (SSA): A 65nm silicon-strip readout ASIC for the Pixel-Strip (PS) module of the CMS Outer Tracker detector upgrade at HL-LHC*, *PoS TWEPP-17* (2018) 031. 5 p.
- [133] D. Ceresa, A. Marchioro, K. Kloukinas, J. Kaplon, W. Bialas, V. Re et al., *Macro Pixel ASIC (MPA): the readout ASIC for the pixel-strip (PS) module of the CMS outer tracker at HL-LHC*, *JINST* **9** (2014) C11012.
- [134] *Irradiation center Karlsruhe.*
- [135] *Secondary Beams and Areas.*
- [136] H. Jansen et al., *Performance of the EUDET-type beam telescopes*, *EPJ Tech. Instrum.* **3** (2016) 7 [1603.09669].
- [137] C. Hu-Guo et al., *First reticule size MAPS with digital output and integrated zero suppression for the EUDET-JRA1 beam telescope*, *Nucl. Instrum. Meth. A* **623** (2010) 480.
- [138] T. Obermann, M. Backhaus, F. Hügging, H. Krüger, F. Lütticke, C. Marinas et al., *Implementation of a configurable FE-I4 trigger plane for the AIDA telescope*, *JINST* **9** (2014) C03035.

- [139] A. Ryd, D. Lange, N. Kuznetsova, S. Versille, M. Rotondo, D. P. Kirkby et al., *EvtGen: A Monte Carlo Generator for B-Physics*, .

Chapter 9

Conclusions

A search for Higgs boson pair production in the $HH \rightarrow b\bar{b}\tau\tau$ final state, using 35.9fb^{-1} data collected by CMS in 2016, is reported in Chapter 5 of this thesis for both non-resonant and resonant HH production scenarios.

- Non-resonant HH production: The search has been performed through both the SM and BSM Higgs couplings. The transverse mass (m_{T2}) has been used as the final discriminating variable. Data and expected background distributions of m_{T2} are found to agree within the statistical and systematic uncertainties and no excess is observed. Therefore, a 95% CL limit on the non-resonant $\sigma_{HH} \times \mathcal{B}(HH \rightarrow b\bar{b}\tau\tau)$ is set. The observed (expected) 95% CL limit on the SM non-resonant $\sigma_{HH} \times \mathcal{B}(HH \rightarrow b\bar{b}\tau\tau)$ is 75.4 (61.0) fb, which is 30 (25) times the SM prediction. The 95% CL limit on $\sigma_{HH} \times \mathcal{B}(HH \rightarrow b\bar{b}\tau\tau)$ is also estimated as a function of κ_λ/κ_t and is compared with the theoretical predictions for $\kappa_t = 1$ and 2. The excluded regions at 95% CL level, in the $\kappa_t - \kappa_\lambda$ plane, is also

studied.

- Resonant HH production: The invariant mass of the two Higgs boson candidates, calculated with a kinematic fit algorithm (m_{HH}^{KinFit}), has been the natural choice as the final discriminant. The invariant mass distributions of data and background expectation agree within the statistical and systematic uncertainties and no excess is found. Therefore, a 95 % CL limit on the resonant $\sigma_{HH} \times \mathcal{B}(HH \rightarrow b\bar{b}\tau\tau)$, as a function of the mass of the resonant particle, ranging from 250 to 900 GeV , is set. The 95 % CL limits obtained are interpreted in the habemus Minimal Supersymmetric Standard Model (hMSSM) scenario to set exclusion limits in the $\tan\beta - m_A$ plane.

The LHC machine will be upgraded to attain instantaneous luminosities which will be 5 – 7 times higher compared to the current value. To work efficiently in the high radiation environment of the High Luminosity LHC (HL-LHC), the CMS detector will go through an extensive upgrade programme, known as the CMS Phase-2 upgrade. One of the key features of the CMS Phase-2 upgrade is to replace the current tracker with a new one (the so-called CMS Phase-2 tracker), which will have better radiation hardness, lower material budget and higher granularity. The CMS Phase-2 tracker will be equipped with modules, which will be able to reduce the data volume for tracking at the Level1 (L1) trigger system, by selecting high- p_T tracks at the detector front-end. Two different studies related to the CMS Phase-2 upgrade have been reported in Chapters 7 and 8 of the thesis.

- The performance of a number of prototype Strip-Strip (2S) detector modules

of the CMS Phase-2 tracker have been studied under realistic beam conditions. The results obtained in the beam test data analysis show that the 2S modules will be able to select tracks with $p_T > 2 \text{ GeV}$ efficiently, even after withstanding radiation damage until the end the HL-LHC period. The performance of the 2S modules is also found to be uniform over the full detector dimension.

- Currently, CMS is unable to trigger on low- p_T , fully hadronic, final states like $B_s^0 \rightarrow \phi\phi \rightarrow 4 \text{ Kaons}$, due to the lack of a proper trigger. Inclusion of the tracking information in the L1 trigger will allow CMS to trigger on such final states at the HL-LHC. The potential of CMS to trigger on $B_s^0 \rightarrow \phi\phi \rightarrow 4 \text{ Kaons}$ using tracks at L1, has been studied where the results show that a moderately high signal efficiency of $\sim 30\%$ can be achieved at a manageable trigger rate of 15 kHz.

SUMMARY

Measurement of the Higgs boson self-coupling is one of the major goals of the LHC, where the Higgs boson pair (HH) production cross-section is one important handle. A search for Higgs boson pair production in the $HH \rightarrow b\bar{b}\tau\tau$ final state, using 35.9fb^{-1} data collected by the CMS in 2016, has been reported in this thesis for the following scenarios,

- Non-resonant HH production, where the Higgs boson pair is produced through various couplings of the Higgs boson. Both Standard Model and beyond Standard Model (BSM) couplings are considered.
- Resonant HH production, where a BSM particle directly decays to pair of Higgs bosons.

The analysis of $HH \rightarrow b\bar{b}\tau\tau$ has been performed for the semi-leptonic and fully hadronic decay modes of the τ pair, which constitute $\sim 80\%$ of all τ pair decays. $t\bar{t} + jets$, $Z/\gamma^* \rightarrow ll + jets$ and QCD multi-jet events are the major sources of background in this analysis. There are also small background contributions from the di-boson, single top, W boson production in association with jets, single Higgs boson production and Electroweak + 2 jets events. No excess is found in data over the expected background and a 95% CL limit on both resonant and non-resonant $\sigma_{HH} \times \mathcal{B}(HH \rightarrow b\bar{b}\tau\tau)$ is set.

The LHC machine will be upgraded to attain instantaneous luminosities a factor 5 – 7 higher than the current value. In order to work efficiently in the extremely high radiation environment of the High Luminosity LHC (HL-LHC), the CMS detector

will go through an extensive upgrade programme, known as the CMS Phase-2 upgrade. One key feature of the CMS Phase-2 upgrade is to replace the current tracker completely with the so-called CMS Phase-2 tracker, with better radiation hardness, lower material budget and higher granularity. The CMS Phase-2 tracker will be equipped with modules, which will be able to reduce the data volume for tracking at the Level1 (L1) trigger system, by selecting high- p_T tracks at the detector front-end.

The performance of a number of prototype Strip-Strip (2S) detector modules of the CMS Phase-2 tracker have been studied under realistic beam conditions and the results obtained have been presented in the thesis. The capability of CMS at the HL-LHC to trigger on rare, low- p_T , fully hadronic final states, like $B_s^0 \rightarrow \phi\phi \rightarrow 4$ Kaons, using tracks reconstructed at the L1 trigger, has also been reported.

Thesis Keywords

Name of the Student: Rajarshi Bhattacharya

Name of the CI/OCC: Saha Institute of Nuclear Physics

Enrolment No.: PHYS05201304017

Thesis Title: Search for Higgs boson pair production in the $HH \rightarrow bb\tau\tau$ channel in p-p collisions using CMS data at $\sqrt{s} = 13$ TeV at the LHC

Discipline: eg. **Physical Sciences** **Sub-Area of Discipline:** **Experimental High Energy**

Date of viva voce: 19/01/2021

1. The Standard Model of Particle Physics
2. Higgs boson pair production
3. $HH \rightarrow bb\tau\tau$ decay
4. The CMS detector
5. The CMS Phase-2 tracker
6. Strip-Strip (2S) module
7. $B_s^0 \rightarrow \phi \phi \rightarrow 4$ Kaons decay

Thesis Highlight

Name of the Student: Rajarshi Bhattacharya

Name of the CI/OCC: Saha Institute of Nuclear Physics

Enrolment No.: PHYS05201304017

Thesis Title: Search for Higgs boson pair production in the $HH \rightarrow bb\tau\tau$ channel in p-p collisions using CMS data at $\sqrt{s} = 13$ TeV at the LHC

Discipline: eg. **Physical Sciences**

Sub-Area of Discipline: **Experimental High Energy**

Date of viva voce: 19/01/2021

Measurement of the Higgs boson self-coupling is one of the major goals of the LHC, where the Higgs boson pair (HH) production cross-section is one important handle. A search for Higgs boson pair production in the $HH \rightarrow bb\tau\tau$ final state, using 35.9 fb^{-1} data collected by the CMS in 2016, has been reported in this thesis for the following scenarios,

- Non-resonant HH production, where the Higgs boson pair is produced through various couplings of the Higgs boson. Both Standard Model and beyond Standard Model (BSM) couplings are considered.
- Resonant HH production, where a BSM particle directly decays to pair of Higgs bosons.

The analysis of $HH \rightarrow bb\tau\tau$ has been performed for the semi-leptonic and fully hadronic decay modes of the τ pair, which constitute $\sim 80\%$ of all τ pair decays. $t\bar{t} + \text{jets}$, $Z/\gamma^* \rightarrow \ell\bar{\ell} + \text{jets}$ and QCD multi-jet events are the major sources of background in this analysis. There are also small background contributions from the di-boson, single top, W boson production in association with jets, single Higgs boson production and Electroweak + 2 jets events. No excess is found in data over the expected background and a 95% CL limit on both resonant and non-resonant $\sigma_{HH} \times B(HH \rightarrow bb\tau\tau)$ is set. The observed (expected) limit on the Standard Model $HH \rightarrow bb\tau\tau$ production cross-section is 31 (25) \times the Standard Model prediction.

The LHC machine will be upgraded to attain instantaneous luminosities a factor 5 - 7 higher than the current value. In order to work efficiently in the extremely high radiation environment of the High Luminosity LHC (HL-LHC), the CMS detector will go through an extensive upgrade programme, known as the CMS Phase-2 upgrade. One key feature of the CMS Phase-2 upgrade is to replace the current tracker completely with the so-called CMS Phase-2 tracker, with better radiation hardness, lower material budget and higher granularity. The CMS Phase-2 tracker will be equipped with modules, which will be able to reduce the data volume for tracking at the Level1 (L1) trigger system, by selecting high- p_T tracks at the detector front-end.

The performance of a number of prototype Strip-Strip (2S) detector modules of the CMS Phase-2 tracker have been studied under realistic beam conditions and the results obtained have been presented in the thesis. The capability of CMS at the HL-LHC to trigger on rare, low- p_T , fully hadronic final states, like $B_s^0 \rightarrow \phi$ $\phi \rightarrow 4$ Kaons, using tracks reconstructed at the L1 trigger, has also been reported.